

Diss. ETH No. 30180

# **Magnetic Levitation Platform Featuring an Exceptionally Large Levitation Distance**

A thesis submitted to attain the degree of

DOCTOR OF SCIENCES  
(Dr. sc. ETH Zurich)

presented by

RETO BONETTI

MSc ETH

born on 02.03.1995

accepted on the recommendation of

Prof. Dr. Johann W. Kolar, examiner

Prof. Dr. Hans-Peter Nee, co-examiner

2024

ETH Zurich  
Power Electronic Systems Laboratory  
Physikstrasse 3 | ETL H23  
8092 Zurich | Switzerland

<http://www.pes.ee.ethz.ch>

© 2024, Reto Bonetti

# Acknowledgments

**F**IRST of all, I would like to express my gratitude to Prof. Dr. Johann W. Kolar for accepting me as a doctoral student in his group, providing me with the necessary tools to carry out the project, and helping me in difficult situations with prompt inputs.

A special thank you goes to Prof. Dr. Hans-Peter Nee, who accepted to be my co-examiner. Thank you for taking the time to read my thesis and joining my Ph.D. defense.

I would also like to thank Prof. Dr. Jörg Hugel for his financial support through the “Else und Friedrich Hugel-Fonds für Mechatronik / ETH Foundation”. His interest in my research has always been a motivating factor.

Most of my doctoral studies have been co-supervised by Dr. Dominik Bortis, who asked me to join the Power Electronic System Laboratory (PES) as a Ph.D. student. Thank you for your guidance, your theoretical and practical expertise, and for enriching my knowledge. Working with you has been challenging, but this has helped to shape my character.

Ass. Prof. DDr. Spasoje Mirić deserves immense gratitude for helping me during the latest stage of my project under intricate circumstances. Thank you for your technical inputs during the commissioning of the magnetic levitation platform and, most importantly, for taking the time to read and improve the last two publications. It has been a pleasure to share the office with you during my first year at PES and be able to use your inverter in my project. Thank you, Spasoje!

Without the social support of the rest of the PES team, coming to the end of my project would have been more demanding. A special thank you goes to Dr. Pascal Niklaus, who has been my reference point for technical questions starting from my first project at PES under his supervision. Also, he entertained me and my colleagues during the lunch breaks with countless jokes. Thank you to my long-term office mate, Gwendolin Rohner, whom I enjoyed talking about work-related and other stuff every day. She was the mind behind most social events, always motivated me to participate, and shared tons of crackers with me. Thank you to Rosario Giuffrida for creating a relaxed and cheerful atmosphere, introducing me to the FPGA board used at PES, and providing hardware and support for developing the eddy current sensor. Thank you to Ivana Bagaric, with whom I had the pleasure of teaching a laboratory course for bachelor students and had the opportunity to chat, improving my German. Closing this restricted group of colleagues with whom I spent most of my time at PES and outside ETH, thank you to Neha Nain for your trust in letting me water your plants during your absence

and for generously compensating me for this simple task.

Special thanks go to the other colleagues who contributed to making life pleasing at PES and with whom I enjoyed extra-work events. Thank you to Dr. Daifei Zhang, Dr. Jannik Schäfer, Dr. David Menzi (the only one who dared to join me for some cold winter swims in the Limmat), Dr. Junzhong Xu, Emanuel Hubmann, Dr. Thomas Langbauer (who introduced me to Kalman filters), Sven Weihe, Saransh Chhawchharia, Luc Imperiali, Patrick Ziegler, Elias Bürgisser, and Andreas Horat (who helped me debugging VHDL codes, thank you!).

Also, I am grateful to all bachelor and master students who directly contributed to the project: Lars Beglinger (who had the brilliant idea of using a force sensor for the closed-loop control of the magnetic levitation platform), Vinzenz Tütsch, Milena Keller, Till Aerni, Fabian Hirth, David Sommer, and Timon Schmidt.

Furthermore, I would like to thank the group leaders, Dr. Florian Krismer and Dr. Jonas Huber, and the administrative team at PES for their work. Special recognition goes to Peter Seitz, Prisca Maurantonio, Yvonne Schnyder-Lieberherr, Nadine Wacha, Roswitha Coccia, and Monica Kohn.

Of course, I would also like to thank the rest of the graduated colleagues who already left PES. I had the pleasure of getting to know and exchanging some talks with Dr. Mattia Guacci, Dr. Michael Antivachis, Dr. Jon Azurza Anderson, Dr. Pantelis Papamanolis (my personal hairdresser), Dr. Piotr Czyż, Dr. Gustavo Knabben, Dr. Michael Haider, Dr. Julian Böhler, Dr. Morris Heller, Dr. Marc Röthlisberger, and Dr. Yunni Li.

Last but not least, I would like to thank all my family members for their incredible support and motivation during these years. Thank you very much!

*Thank you! Danke! Grazie!*

Zurich, March 2024

Reto Bonetti

# Abstract

**H**YBRID magnetic bearings are widely used in mechatronics, covering various applications. For instance, they substitute conventional ball bearings in electric machines, enabling ultra-high rotational speeds due to eliminating friction, which usually causes wear and tear and excessive heat generation. Additionally, their air gap permits decoupling two subsystems with a barrier. Therefore, they are employed in machines for clean environments to prevent contamination between two subsystems while transferring and converting electrical power from the stator to the rotor into mechanical work.

This thesis proposes a magnetic levitation platform (MLP), in the form of an axial hybrid magnetic bearing, with the target of enlarging the air gap between the permanent magnets (PMs, located in the stator and mover) constituting the passive part of the MLP. Compared to existing drive systems employed in industry, which are characterized by an air gap being orders of magnitude smaller than the most extensive system's dimension (i.e., the characteristic dimension), the air gap achieved in this thesis is about half the characteristic dimension of the MLP. This air gap enlargement permits the extension of the mentioned application of decoupling two subsystems where the conventional limited air gap is problematic and, eventually, enables entirely new applications.

The challenge regarding the enlargement of the air gap is overcome by optimizing the PMs' dimensions achieved with an analytical method that calculates the magnetic forces between PMs. The resulting MLP is based on a steady PM (stator) and an axially stacked levitating PM (mover), which is repelled by the stator, creating an air gap of 104 mm, determined by the balance of the vertical magnetic force with the mover's gravitational force. In addition, the proposed analytical calculation method ensures that three out of six mover's degrees of freedom (DOFs) are passively stable. Stable axial magnetic forces passively hold the mover at the given distance. In contrast, radial magnetic forces destabilize the mover from the radially centered position. Therefore, they must be actively compensated by forces generated with electromagnets (EMs) placed at the stator level that constitute the active part of the MLP. The EMs are designed to control the mover at a given distance from the center while minimizing the power consumption and restricting their size to get a compact system. The assembly of stator and EMs determines the characteristic dimension of the MLP, which results in 207 mm. Furthermore, the mover can rotate around all axes while levitating. The rotation around the radial axes occurs due to destabilizing radial displacements and

due to control actions by the EMs. This rotation is passively stable because of counteracting magnetic torques holding the mover parallel to the stator. The rotation around the axial axis can be initiated by external torques and cannot be influenced by magnetic or electromagnetic torques due to the axial symmetry of the MLP. This rotation is marginally stable, and an active control is disregarded in this thesis.

The challenges that follow the enlargement of the air gap are connected to the active position control of the mover, which must be controlled in the radial direction. In this context, a sensing system able to measure the mover's position at large distances is required to close the position control loop. Moreover, the sensor must operate irrespective of the material used to separate the two subsystems (stator with EMs and mover) for applications of the MLP in clean environments. These two requirements are satisfied by employing a force sensor capturing the reaction forces on the stator and EMs caused by the mover's radial displacement, rotation around the radial axes, and control actions. Due to the superposition of the mover's radial position, angle, and EM current on the sensed signal, a sophisticated control algorithm is required. First, an observer extracts each quantity from the measured reaction force. Then, a controller regulates the mover's radial position and actively dampens the mover's rotation around the radial axes, which is poorly damped by passive magnetic interactions because of the relatively large air gap. The observer relies on a dynamic model of the complete MLP, including the force sensor. The dynamic model is proven with measurements and augmented to include and/or compensate undesired disturbances in the observer to estimate the mover's position and angle better, achieving stable levitation.

The levitation performance of the MLP using the force sensor is finally compared to the performance obtained with a custom eddy current sensor, which is more commonly employed in conjunction with MLPs but cannot be applied when the barrier separating the mover from the stator is electrically conductive. The electromagnetic coils within the eddy current sensor are designed to sense the mover's radial position with maximal sensitivity. Their arrangement is carefully chosen to enhance their electromagnetic coupling, which is influenced by the electrically conductive components of the MLP, such as PMs and EMs. The eddy current sensor requires the same observed-based controller structure since the measured signal contains the mover's position and angle. However, the observer implementation is simplified due to the larger sensor's bandwidth and a sensed signal less prone to disturbances. Therefore, the levitation performance using the eddy current sensor is improved by a factor of eight. In quantitative terms, the achieved standard

deviation of the mover's radial position from the radially centered position is (0.15 mm, 0.26 mm) for the two radial axes.

Furthermore, the eddy current sensor permits the investigation of dynamical position tracking with and without additional weight on the mover, demonstrating the potential applications of the investigated MLP for transporting objects with the mover.





# Sommario

I cuscinetti magnetici ibridi sono ampiamente utilizzati nella meccatronica, coprendo diverse applicazioni. Ad esempio, sostituiscono i convenzionali cuscinetti a sfere nei motori elettrici, consentendo velocità di rotazione molto elevate grazie all'eliminazione dell'attrito, che di solito provoca usura ed eccessiva generazione di calore. Inoltre, il loro traferro (ovvero, lo spazio d'aria fra le proprie componenti) permette di separare due sottosistemi con una barriera. Pertanto, vengono impiegati in motori elettrici per ambienti sterili al fine di prevenire la contaminazione tra due sottosistemi durante il trasferimento e la conversione di potenza elettrica dallo statore al rotore in lavoro meccanico.

Questa tesi propone una piattaforma a levitazione magnetica (MLP), sotto forma di cuscinetto magnetico ibrido assiale, con l'obiettivo di ingrandire il traferro tra i magneti permanenti (PMs, situati nello statore e nel fluttuatore) che costituiscono la parte passiva del MLP. Rispetto ai sistemi tradizionali impiegati nell'industria, caratterizzati da un traferro che è ordini di grandezza inferiore rispetto alla massima dimensione del sistema (cioè la lunghezza caratteristica), il traferro ottenuto in questa tesi è approssimativamente la metà della lunghezza caratteristica del MLP. Questo allargamento del traferro permette di estendere l'applicazione di separare due sottosistemi in cui il limitato convenzionale traferro è problematico, ed eventualmente consente applicazioni completamente nuove.

La sfida relativa all'ingrandimento del traferro viene superata ottimizzando le dimensioni dei magneti, ottenute con un metodo analitico che calcola le forze magnetiche tra magneti. Il risultante MLP si basa su un magnete fisso (statore) e su un magnete levitante sovrapposto assialmente (fluttuatore), che è respinto dallo statore, creando un traferro di 104 mm, determinato dall'equilibrio tra la forza magnetica verticale e la forza gravitazionale del fluttuatore. In aggiunta, il proposto metodo di calcolo analitico assicura che tre dei sei gradi di libertà (DOFs) del fluttuatore siano passivamente stabili. Le stabili forze magnetiche assiali sospendono passivamente il fluttuatore alla distanza desiderata. Al contrario, le forze magnetiche radiali destabilizzano il fluttuatore dalla posizione radialmente centrata. Pertanto, devono essere attivamente compensate da forze generate con elettromagneti (EMs) posizionati a livello dello statore che costituiscono la parte attiva del MLP. Gli elettromagneti sono progettati per controllare il fluttuatore ad una determinata distanza dal centro, minimizzando il consumo di energia e limitando le loro dimensioni per ottenere un sistema compatto. L'insieme dello statore ed elettromagneti determina la lunghezza caratteristica del MLP, che risulta essere di 207 mm.

Inoltre, il fluttuatore può ruotare intorno a tutti gli assi mentre levita. La rotazione intorno agli assi radiali avviene a causa di spostamenti radiali destabilizzanti e delle azioni di controllo degli elettromagneti. Questa rotazione è passivamente stabile grazie ai momenti di forza magnetici contrastanti che mantengono il fluttuatore parallelo allo statore. La rotazione intorno all'asse assiale può essere innescata da momenti di forza esterni e non può essere influenzata da momenti di forza magnetici o elettromagnetici a causa della simmetria assiale del MLP. Questa rotazione è marginalmente stabile e un suo controllo attivo non viene considerato in questa tesi.

Le sfide che seguono l'ingrandimento del traferro sono legate al controllo attivo della posizione del fluttuatore, che deve essere stabilizzato nella direzione radiale. Per raggiungere ciò, è richiesto un sensore in grado di misurare la posizione del fluttuatore a grandi distanze al fine di chiudere il circuito di controllo della posizione. In aggiunta, il sensore deve funzionare indipendentemente dal materiale utilizzato per separare i due sottosistemi (statore con elettromagneti e fluttuatore) per le applicazioni del MLP in ambienti sterili. Questi due requisiti vengono soddisfatti impiegando un sensore di forza che cattura le forze di reazione vincolari sullo statore e sugli elettromagneti causate dallo spostamento radiale del fluttuatore, dalla sua rotazione intorno agli assi radiali e dalle azioni di controllo. A causa della sovrapposizione della posizione radiale del fluttuatore, del suo angolo e della corrente elettromagnetica nel segnale rilevato, è richiesto un sofisticato algoritmo di controllo. Inizialmente, un osservatore di stato estrae ciascuna grandezza dalla forza di reazione vincolare misurata. Successivamente, un controllore regola la posizione radiale del fluttuatore e smorza attivamente la rotazione del fluttuatore intorno agli assi radiali, che è scarsamente smorzata dalle interazioni magnetiche passive a causa del relativamente ampio traferro. L'osservatore di stato si basa su un modello delle dinamiche all'interno del MLP, compreso il sensore di forza. Il modello delle dinamiche viene dimostrato con misurazioni e ampliato per includere e/o compensare disturbi indesiderati nell'osservatore di stato per stimare la posizione e l'angolo del fluttuatore in modo migliore, al fine di ottenere una levitazione stabile.

Le prestazioni di levitazione del MLP utilizzando il sensore di forza vengono finalmente confrontate con le prestazioni ottenute con un sensore induttivo a correnti parassite (principio "eddy current") personalizzato, che è più comunemente impiegato in combinazione con gli MLPs ma non può essere applicato quando la divisione che separa il fluttuatore dallo statore è elettricamente conduttiva. Le bobine elettromagnetiche all'interno del sensore induttivo sono progettate per rilevare la posizione radiale del fluttuatore con

massima sensibilità. La loro disposizione è attentamente scelta per migliorare il loro accoppiamento elettromagnetico, che è influenzato dalle componenti elettricamente conduttive del MLP, ossia i magneti e gli elettromagneti. Il sensore induttivo richiede lo stesso sistema di controllo basato sull'osservatore di stato poiché il segnale misurato contiene la posizione radiale e l'angolo del fluttuatore. Tuttavia, l'implementazione dell'osservatore di stato è semplificata grazie alla maggiore larghezza di banda del sensore e ad un segnale rilevato meno suscettibile a disturbi. Pertanto, le prestazioni di levitazione utilizzando il sensore induttivo sono migliorate di un fattore di otto. In termini quantitativi, lo scarto quadratico medio della posizione radiale del fluttuatore rispetto alla posizione radialmente centrata è di (0.15 mm, 0.26 mm) per i due assi radiali.

Inoltre, il sensore induttivo consente di studiare il tracciamento dinamico della posizione con o senza peso aggiuntivo sul fluttuatore, dimostrando le potenziali applicazioni dell'esaminato MLP per il trasporto di oggetti con il fluttuatore.



# Abbreviations

2D	Two-Dimensional
3D	Three-Dimensional
ADC	Analog-to-Digital Converter
Buf.	Buffer
CD	Characteristic Dimension
CDRLH	Characteristic Dimension-Related Levitation Height
CM	Common-Mode
const.	Constant
CPU	Central Processing Unit
DC	Direct Current
DOF	Degree of Freedom
ECS	Eddy Current Sensor
EM	Electromagnet
EMF	Electromotive Force
FPGA	Field Programmable Gate Array
freq.	Frequency
Im	Imaginary Axis
Inv.	Inverter
LHP	Left-Half-Plane
LP	Levitation Point
LQR	Linear-Quadratic Regulator
MLP	Magnetic Levitation Platform
MMF	Magnetomotive Force
N	North Pole of Permanent Magnets
NdFeB	Neodymium-Iron-Boron
PCB	Printed Circuit Board
PD	Proportional-Derivative
PI	Proportional-Integral
PID	Proportional-Integral-Derivative
PM	Permanent Magnet
Re	Real Axis
RFS	Reaction Force Sensor
RHP	Right-Half-Plane
RMS	Root Mean Square
S	South Pole of Permanent Magnets
SNR	Signal-to-Noise Ratio
SoC	System on a Chip

## Abbreviations

---

TF	Transfer Function
VGA	Variable Gain Amplifier

# List of Symbols

$A$	State matrix of the MLP's dynamic model
$a_1, a_2$	Scaling factors of the PMs' dimensions
$A_{\text{ctrl}}$	State matrix of the mover's position state-space controller
$B$	Input vector of the MLP's dynamic model
$\mathbf{B}$	Magnetic flux density vector
$B_{\text{ctrl}}$	Input vector of the mover's position state-space controller
$B_{m,z}$	Mover's magnetic flux density in the $z$ direction
$B_s$	Stator's magnetic flux density
$C$	Output vector of the MLP's dynamic model
$C_c$	Coupling capacitance between electromagnets and force sensor's ground connection
$C_{\text{ctrl}}$	Output vector of the mover's position state-space controller
$\text{CDRLH}^*$	Scaled characteristic dimension-related levitation height
$C_{\text{EM}}$	Parasitic capacitance of the electromagnet
$C_{\text{exc}}$	Parasitic capacitance of the eddy current sensor's excitation coil
$C_f$	Capacitor of the inverter's $LC$ filter
$C_{\text{fd}}$	Capacitor in the damping branch of the inverter's $LC$ filter
$C_{\text{filt}}$	Capacitor of the force sensor's active first-order filter
$C_{\text{sens}}$	Parasitic capacitance of the eddy current sensor's sensing coils
$d\mathbf{A}_w$	Elemental area vector
$dA_{w,z}$	Elemental area vector component in the $z$ direction
$d\mathbf{B}_m$	Differential of the mover's magnetic flux density vector
$dB_{m,z}$	Change of mover's magnetic flux density in the $z$ direction
$dF_x/dx_m$	Force gradient in the $x$ direction
$dF_y/dy_m$	Force gradient in the $y$ direction
$dF_z/dz_m$	Force gradient in the $z$ direction
$dI/dt$	Current slope over time
$d\mathbf{l}_m$	Direction vector of an infinitesimally small piece of conductor of the mover's Ampèrian model

## List of Symbols

---

$d\mathbf{l}_s$	Direction vector of an infinitesimally small piece of conductor of the stator's Ampèrian model
$dt$	Differential of time
$dT_x/d\theta_{m,x}$	Torque gradient in the $x$ direction
$dT_y/d\theta_{m,y}$	Torque gradient in the $y$ direction
$dT_z/d\alpha_{m,z}$	Torque gradient in the $z$ direction
$dv/dt$	Voltage slope over time
$d_w$	Diameter of the electromagnet's wire including insulation
$d_{w,Cu}$	Diameter of the electromagnet's copper wire
$d_{w,max}$	Maximum diameter of the electromagnet's wire including insulation
$d_{w,min}$	Minimum diameter of the electromagnet's wire including insulation
$dx_m$	Small displacement of the mover in the $x$ direction
$dy_m/dt$	Mover's speed in the $y$ direction
$dz_m$	Small displacement of the mover in the $z$ direction
$d^2y_m/dt^2$	Mover's acceleration in the $y$ direction
$d\theta_{m,y}$	Small rotation of the mover around the $y$ axis
$d\phi/dt$	Magnetic flux slope over time
$EM_{x,1}, EM_{x,2}$	Electromagnets on the $x$ axis
$EM_{y,1}, EM_{y,2}$	Electromagnets on the $y$ axis
$\mathbf{F}$	Force vector
$f_0$	Natural frequency for second-order systems
$f_{0,LC}$	Design frequency of the inverter's $LC$ filter
$f_{bw,ECS}$	Eddy current sensor's approximate bandwidth
$f_d$	Pole/zero frequency of $H_d$
$F_{EM}$	Electromagnetic force
$F_{EM,PD}$	Electromagnetic force calculated with the PD-controller for the mover's position
$f_{exc}$	Eddy current sensor's excitation frequency
$f_{f,ECS}$	Cutoff frequency of the eddy current sensor's output filter
$F_{RFS}$	Total force acting on the force sensor
$F_g$	Mover's gravitational force
$F_g^*$	Scaled mover's gravitational force
$\mathbf{F}_k$	Force vector on a single conductor segment of the Ampèrian model



$f_{n, \text{filt}}$	Cutoff frequency of the force or eddy current sensor's output filter
$f_{n, \text{RFS}}$	Force sensor's natural frequency
$f_{n, \text{rot}}$	Natural frequency of the mover's rotation around the radial axes
$f_{n, \text{disp}}$	Natural frequency of the mover's radial displacement
$F_{\text{PM}}$	Magnetic force
$F_{\text{PM}, x}$	Magnetic force in the $x$ direction
$F_{\text{push}}$	External push force on the mover
$F_{\text{rot}}$	Rotational force
$f_{\text{sens}}$	Self resonant frequency of the eddy current sensor's sensing coils
$f_{\text{sw}}$	Switching frequency of the inverter
$\mathbf{F}_{\text{tot}}$	Total force vector acting on the mover
$F_x$	Force in the $x$ direction
$F_x/I$	Normalized force in the $x$ direction produced by a single-turn coil on the mover
$F_y$	Force in the $y$ direction
$F_z$	Force in the $z$ direction
$F_{z, \text{max}}$	Maximum force in the $z$ direction
$F_{z, \text{max}}/F_g$	Payload capability
$F_{z, \text{max}}^*/F_g^*$	Scaled payload capability
$G_{\text{CL}}$	Closed-loop transfer function of the mover's position control loop
$G_{\text{CL}, \text{out}}$	Closed-loop transfer function of the outer current control loop
$G_{\text{dist}, \text{xx}, \text{ECS}}$	Disturbance transfer function on $G_{\text{tot}, x, \text{ECS}}$
$G_{\text{dist}, \text{xx}, \text{RFS}}$	Disturbance transfer function on $G_{\text{tot}, x, \text{RFS}}$
$G_{\text{dist}, \text{xx}}$	Disturbance transfer function on $G_{\text{tot}, x}$
$G_{\text{dist}, \text{xy}, \text{RFS}}$	Cross-coupling transfer function on $U_{\text{out}, y}$ from $I_x$ for the force sensor
$G_{\text{dist}, \text{xy}}$	Cross-coupling transfer function on $U_{\text{out}, y}$ from $I_x$
$G_{\text{dist}, \text{xy}, \text{RFS}}$	Cross-coupling transfer function on $U_{\text{out}, x}$ from $I_y$ for the force sensor
$G_{\text{dist}, \text{yx}}$	Cross-coupling transfer function on $U_{\text{out}, x}$ from $I_y$
$G_{\text{dist}, \text{yy}, \text{ECS}}$	Disturbance transfer function on $G_{\text{tot}, y, \text{ECS}}$
$G_{\text{dist}, \text{xy}, \text{RFS}}$	Disturbance transfer function on $G_{\text{tot}, y, \text{RFS}}$
$G_{\text{dist}, \text{yy}}$	Disturbance transfer function on $G_{\text{tot}, y}$
$G_{\text{el}}$	Transfer function from $U_{\text{inv}}$ to $I_{\text{inv}}$

## List of Symbols

---

$G_{\text{filt}}$	Transfer function of the filter for the mover's position and current measurement
$G_{\text{L,out}}$	Transfer function of the integral controller for the outer current control loop
$G_{\text{LC,EM}}$	Transfer function from $U_{\text{inv}}$ to $I$
$G_{\text{meas}}$	Measured transfer function to prove the MLP's dynamic model
$G_{\text{meas,x}}$	Measured transfer function to prove the MLP's dynamic model for the $x$ axis
$G_{\text{meas,y}}$	Measured transfer function to prove the MLP's dynamic model for the $y$ axis
$G_{\text{OL}}$	Open-loop transfer function for the mover's position control loop
$G_{\text{PI,ctrl}}$	Transfer function of the PI-controller for the mover's position
$G_{\text{PI,in}}$	Transfer function of the PI-controller for the inner current control loop
$\text{grad}(F)$	Force gradient
$\text{grad}(F)^*$	Scaled force gradient
$\text{grad}(T)$	Torque gradient
$\text{grad}(T)^*$	Scaled torque gradient
$G_{\text{tot}}$	Transfer function of the total MLP's dynamic model
$G_{\text{tot,x,ECS}}$	Transfer function of the total MLP's dynamic model including the eddy current sensor for the $x$ axis
$G_{\text{tot,y,ECS}}$	Transfer function of the total MLP's dynamic model including the eddy current sensor for the $y$ axis
$G_{\text{tot,x,RFS}}$	Transfer function of the total MLP's dynamic model including the force sensor for the $x$ axis
$G_{\text{tot,y,RFS}}$	Transfer function of the total MLP's dynamic model including the force sensor for the $y$ axis
$G_{\text{tot,x}}$	Transfer function of the total MLP's dynamic model for the $x$ axis
$G_{\text{tot,y}}$	Transfer function of the total MLP's dynamic model for the $y$ axis
$h$	Levitation height
$H$	Scale factor for the mover's position state-space controller
$h^*$	Scaled levitation height
$h_1$	Levitation height example 1

---

$h_2$	Levitation height example 2
$H_{ci,m}$	Mover's coercive field
$H_{ci,s}$	Stator's coercive field
$H_d$	Transfer function approximation of a time delay
$\tilde{H}_d$	Phase-equivalent transfer function of $H_d$
$h_{EM}$	Height of the electromagnet's winding area
$h_m$	Mover's height
$h_m^*$	Scaled mover's height
$h_{max}$	Maximum levitation height
$h_{min}$	Minimum levitation height
$h_s$	Stator's height
$h_s^*$	Scaled stator's height
$I$	Current in the electromagnets
$\hat{I}$	Peak current in the electromagnets
$i_{CM}$	Common-mode current generated by the inverter
$I_{err}$	Measurement error of the current sensor
$I_{final}^*$	Reference current for the outer current controller
$I_{final,x}^*$	Reference current for the $x$ axis outer current controller
$i_{HF}, i_{HF,1}, i_{HF,2}$	High-frequency current generated by the inverter
$I_{inv}$	Switched current at the full-bridge inverter output
$I_{inv,x}$	Switched current at the full-bridge inverter output for the $x$ axis
$I_m$	Mover's Ampèrian model current
$I_{max}$	Maximum current in the electromagnets
$I_{meas,x}$	Measured current in the electromagnets for the $x$ axis
$I_{meas,y}$	Measured current in the electromagnets for the $y$ axis
$I_{PD}$	Current calculated with the PD-controller for the mover's position
$I_{PI}$	Current calculated with the PI-controller for the mover's position
$I_s$	Stator's Ampèrian model current
$I_x$	Control and measured current in the electromagnets for the $x$ axis
$I_x^*$	Reference current for the $x$ axis
$\hat{I}_x$	RMS noise amplitude on the measured current in the electromagnets for the $x$ axis
$I_{x,1}$	Current in the electromagnet $EM_{x,1}$
$I_{x,2}$	Current in the electromagnet $EM_{x,2}$

## List of Symbols

---

$I_y$	Control and measured current in the electromagnets for the $y$ axis
$\hat{I}_y$	RMS noise amplitude on the measured current in the electromagnets for the $y$ axis
$j$	Imaginary unit
$J$	Current density in the electromagnet
$J_m$	Mover's moment of inertia for the radial axes
$J_{\max}$	Maximum current density in the electromagnet
$K$	Gain vector of the mover's position state-space controller
$k_1, k_2, k_3, k_4$	Gains of the mover's position state-space controller
$k_{D1}$	Derivative gain of the PD-controller for the mover's position
$k_{d,RFS}$	Force sensor's viscous damping
$k_{d,rot}$	Damping constant for the mover's rotation around the radial axes
$k_{FEM}$	Electromagnets' force constant
$k_{fill}$	Fill factor of the electromagnet's winding area
$k_{FPM}$	Radial stiffness
$k_{Frot}$	Rotational force constant
$k_I$	Integral gain of the mover's position state-space controller
$k_{I2}$	Integral gain of the PI-controller for the mover's position
$k_{IPS}$	Eddy current sensor's gain
$k_{P1}$	Proportional gain of the PD-controller for the mover's position
$k_{P2}$	Proportional gain of the PI-controller for the mover's position
$k_{s,RFS}$	Force sensor's stiffness
$k_{Tdisp}$	Displacement torque constant
$k_{TEM}$	Electromagnets' torque constant
$k_{TPM}$	Rotational stiffness
$k_v$	Electrical conversion constant
$k_{v,disp}$	Eddy current sensor's sensitivity for the mover's radial displacement
$k_{v,rot}$	Eddy current sensor's sensitivity for the mover's rotation around the radial axes
$k_{v,RFS}$	Force sensor's electrical conversion constant
$k_{VGA}$	Electrical gain
$k_\omega$	Ratio between $\omega_c$ and $\omega_0$

---

$l_1, \dots, l_6$	Electromagnet's horizontal layers
$L_{EM}$	Inductance of the electromagnet
$L_{exc}$	Inductance of the eddy current sensor's excitation coil
$L_f$	Inductor of the inverter's $LC$ filter
$L_{sens}$	Inductance of the eddy current sensor's sensing coils
$LP_1$	Levitation point example 1
$LP_2$	Levitation point example 2
$L_{target}$	Inductance of the eddy current sensor's target coil
$l_{tot}$	Total length of the electromagnet's wire
$l_w$	Length of the electromagnet's design winding
$m_m$	Mover's mass
$m_m^*$	Scaled mover's mass
$m_s$	Stator's mass
$m_s^*$	Scaled stator's mass
$m_{mlp}$	Total magnetic levitation platform's weight
$n$	Ratio between $C_{fd}$ and $C_f$ of the inverter's $LC$ filter
$N$	Electromagnet's number of turns
$N_{exc}$	Number of turns of the eddy current sensor's excitation coil
$N_{hor}$	Electromagnet's number of horizontal layers
$N_m$	Number of turns of the mover's Ampèrian model coil
$N_{pts}$	Number of discretization points of the Ampèrian model coil
$N_s$	Number of turns of the stator's Ampèrian model coil
$N_{sens}$	Number of turns of the eddy current sensor's sensing coils
$N_{vert}$	Electromagnet's number of vertical layers
$N_{vert}^{even}$	Electromagnet's number of vertical turns in the horizontal layers with even number
$N_{vert}^{odd}$	Electromagnet's number of vertical turns in the horizontal layers with odd number
$Q$	Symmetric and positive definite weighting matrix of the LQR
$Q_{(1,1)}$	Entry of $Q$ 's first row and first column
$p$	Complex pole
$P$	Solution matrix of the continuous-time Riccati equation
$p_1, p_2, p_3, p_4$	Poles of the mover's position state-space controller
$pm$	Phase margin
$P_{max}$	Maximum power dissipated by the electromagnet

## List of Symbols

---

$r$	Distance between a current carrying conductor and the evaluation point of the magnetic flux density
$R$	Strictly positive weighting constant of the LQR
$\mathbf{r}$	Distance vector between a current carrying conductor and the evaluation point of the magnetic flux density
$R_{EM}$	Resistance of a single electromagnet
$R_{EMd}$	Damping resistance of the electromagnet's resonance
$R_{exc}$	Resistance of the eddy current sensor's excitation coil
$R_{fd}$	Damping resistor of the inverter's $LC$ filter
$R_{filt}$	Resistor of the force sensor's active first-order filter
$r_{i,min}$	Electromagnet's internal radius
$r_m$	Mover's radius
$\mathbf{r}_m$	Radius vector pointing from the mover's center to a conductor segment of its Ampèrian model
$r_m^*$	Scaled mover's radius
$r_{mlp}$	Radius of the magnetic levitation platform corresponding to half of the characteristic dimension
$r_{m,ext}$	Mover's external radius
$r_{m,ext}^*$	Scaled mover's external radius
$r_{m,int}$	Mover's internal radius
$r_{m,int}^*$	Scaled mover's internal radius
$r_s$	Stator's radius
$r_s^*$	Scaled stator's radius
$R_{sens}$	Resistance of the eddy current sensor's sensing coils
$r_{s,ext}$	Stator's external radius
$r_{s,ext}^*$	Scaled stator's external radius
$r_{s,int}$	Stator's internal radius
$r_{s,int}^*$	Scaled stator's internal radius
$R_{target}$	Resistance of the eddy current sensor's target coil
$s$	Laplace's domain complex variable
$SNR_x$	Signal-to-noise ratio for the $x$ axis
$SNR_y$	Signal-to-noise ratio for the $y$ axis
$t$	Time
$T_d$	Time delay of the eddy current sensor's demodulation process
$T_{EM}$	Electromagnetic torque
$T_f$	Time constant of the force or eddy current sensor's output filter
$T_{f,ECS}$	Time constant of the eddy current sensor's output filter

---

$T_{f,RFS}$	Time constant of the force sensor's output filter
$\mathbf{T}_k$	Torque vector on a single conductor segment of the Amperian model
$T_{PM}$	Magnetic torque
$\mathbf{T}_{tot}$	Total torque vector acting on the mover
$T_x$	Torque in the $x$ direction
$T_y$	Torque in the $y$ direction
$T_{y,max}$	Maximum torque in the $y$ direction before the mover changes stability properties
$T_{y,max}^*$	Scaled maximum torque in the $y$ direction before the mover changes stability properties
$T_{y,min}$	Minimum torque in the $y$ direction before the mover changes stability properties
$T_z$	Torque in the $z$ direction
$u$	Input variable of the MLP's dynamic model and the mover's position state-space controller
$U$	Voltage applied to the electromagnets
$u_{amp}$	Force or eddy current sensor's amplified voltage
$u_{amp,ECS}$	Eddy current sensor's amplified voltage
$u_{amp,RFS}$	Force sensor's amplified voltage
$U_{DC}$	DC-link voltage
$U_{DC,min1}$	Minimum $U_{DC}$ required to achieve the inner current controller bandwidth
$U_{DC,min2}$	Minimum $U_{DC}$ required to achieve the current peak in the electromagnets
$u_{DS,1}, u_{DS,2}$	Instantaneous voltage of the low-side inverter switches
$u_{exc}$	Excitation voltage of the force or eddy current sensor
$u_{exc,ECS}$	Eddy current sensor's excitation voltage
$u_{exc,RFS}$	Force sensor's excitation voltage
$u_{filt}, U_{filt}$	Force or eddy current sensor's filtered voltage
$\hat{u}_{filt}$	RMS noise of the sensors' filtered voltage
$\dot{u}_{filt}$	Time derivative of $u_{filt}$
$u_{filt,ECS}$	Eddy current sensor's filtered voltage
$\dot{u}_{filt,ECS}$	Time derivative of $u_{filt,ECS}$
$\dot{u}_{filt,RFS}$	Time derivative of $u_{filt,RFS}$
$u_{filt,RFS}$	Force sensor's filtered voltage
$U_{filt,x}$	Force or eddy current sensor's filtered voltage for the $x$ axis

## List of Symbols

---

$U_{\text{filt},y}$	Force or eddy current sensor's filtered voltage for the $y$ axis
$U_{\text{inv}}$	Switched voltage at the full-bridge inverter output
$U_{\text{inv},x}$	Switched voltage at the full-bridge inverter output for the $x$ axis
$U_{\text{inv},x}^*$	Reference inverter output voltage average for the $x$ axis
$U_{\text{max}}$	Maximum allowed DC-link voltage of the inverter board
$\hat{u}_{\text{noise}}$	RMS noise of the sensors' output voltage
$\tilde{U}_{\text{out},x,\text{ECS}}$	Estimated eddy current sensor's output voltage for the $x$ axis
$\tilde{U}_{\text{out},y,\text{ECS}}$	Estimated eddy current sensor's output voltage for the $y$ axis
$\tilde{U}_{\text{out},x,\text{RFS}}$	Estimated force sensor's output voltage for the $x$ axis
$\tilde{U}_{\text{out},y,\text{RFS}}$	Estimated force sensor's output voltage for the $y$ axis
$u_{\text{out},x}, U_{\text{out},x}$	Force and eddy current sensor's output voltage for the $x$ axis
$\tilde{u}_{\text{out},x}, \tilde{U}_{\text{out},x}$	Estimated force and eddy current sensor's output voltage for the $x$ axis
$\hat{u}_{\text{out},x}$	RMS noise of the measured sensors' voltage for the $x$ axis
$u_{\text{out},y}, U_{\text{out},y}$	Force and eddy current sensor's output voltage for the $y$ axis
$\tilde{u}_{\text{out},y}, \tilde{U}_{\text{out},y}$	Estimated force and eddy current sensor's output voltage for the $y$ axis
$\hat{u}_{\text{out},y}$	RMS noise of the measured sensors' voltage for the $y$ axis
$u_{\text{sens}}$	Force or eddy current sensor's unprocessed voltage
$u_{\text{sens},\text{ECS}}$	Eddy current sensor's unprocessed voltage
$\hat{u}_{\text{sens},\text{ECS}}$	Eddy current sensor's demodulated voltage
$u_{\text{sens},\text{RFS}}$	Force sensor's unprocessed voltage
$u(F_x)$	Voltage-dependent force on the $x$ axis
$u(F_y)$	Voltage-dependent force on the $y$ axis
$u(F_z)$	Voltage-dependent force on the $z$ axis
$V$	Cost function of the LQR
$w_{\text{EM}}$	Width of the electromagnet's winding area
$x$	State vector of the MLP's dynamic model
$\dot{x}$	State vector's time derivative of the MLP's dynamic model
$x_{\text{ctrl}}$	State vector of the mover's position state-space controller



---

$\dot{x}_{ctrl}$	State vector's time derivative of the mover's position state-space controller
$x_{err,curr}$	Mover's $x$ position error due to an offset in the current sensor
$x_{err,pos}$	Mover's $x$ position error due to an offset in the position sensor
$x_m, X_m$	Mover's $x$ position
$\dot{x}_m$	Mover's speed in the $x$ direction
$\ddot{x}_m$	Mover's acceleration in the $x$ direction
$x_m^*$	Mover's $x$ position reference
$\tilde{x}_m$	Estimated mover's $x$ position
$\tilde{\dot{x}}_m$	Estimated mover's speed in the $x$ direction
$x_{m,max}$	Maximum mover's $x$ position
$x_{m,max}^*$	Scaled maximum mover's $x$ position
$x_{m,meas}$	Measured mover's position
$\dot{x}_{m,meas}$	Time derivative of the measured mover's position
$x_{m,min}$	Lower detectable limit for the mover's displacement on the $x$ axis
$x_{m,res}$	Mover's displacement resolution for the $x$ axis
$x_s, X_s$	Movement of the force sensor's sensing side
$\dot{x}_s$	Speed of the force sensor's sensing side
$\ddot{x}_s$	Acceleration of the force sensor's sensing side
$x_{s,max}$	Maximum displacement of the force sensor's sensing side
$x_{s,res}$	Force sensor's resolution for the $x$ axis
$y$	Output variable of the MLP's dynamic model
$y_{ctrl}$	Output variable of the mover's position state-space controller
$y_m$	Mover's $y$ position
$y_m^*$	Mover's $y$ position reference
$y_{m,min}$	Lower detectable limit for the mover's displacement on the $y$ axis
$Z$	Complex electrical impedance
$Z_{g,inv}$	Modeled impedance of the electromagnet's cable connected to the inverter
$Z_{g,meas}$	Modeled impedance of the force sensor's ground connection to the inverter
$z_m$	Mover's $z$ position
$z_m^*$	Scaled mover's $z$ position
$(dF_x/dx_m)^*$	Scaled force gradient in the $x$ direction

## List of Symbols

---

$(dF_z/dz_m)^*$	Scaled force gradient in the $z$ direction
$(dT_y/d\theta_{m,y})^*$	Scaled torque gradient in the $y$ direction
$(F_{xy})$	The mover is stable against radial displacements if $\theta_{m,x} = \theta_{m,y} = 0$ (two DOFs are passively stable, and three DOFs must be controlled actively)
$(F_{xy}, T_{xy})$	the mover is stable against radial displacements if $\theta_{m,x} = \theta_{m,y} = 0$ and it is stable against rotations around the $x, y$ axes (four DOFs are passively stable, but the rotation must be actively controlled to zero and one DOF must be controlled actively)
$(F_z)$	The mover is stable against axial displacements (one DOF is passively stable, and four DOFs must be controlled actively)
$(F_z, T_{xy})$	in addition to $(F_z)$ , the mover is stable against rotations around the $x, y$ axes (three DOFs are passively stable, and two DOFs must be controlled actively)
$(T_{xy})$	The mover is stable against rotations around the $y, x$ axes (two DOFs are passively stable, and three DOFs must be controlled actively)
$ \mathbf{F}_{\text{tot}} ^*$	Scaled total force vector acting on the mover
$ \mathbf{T}_{\text{tot}} ^*$	Scaled total torque vector acting on the mover
$\alpha_{m,z}$	Mover's angle for rotations around the axial axis
$\delta$	Skin depth
$\delta_{\text{Cu}}$	Copper's skin depth
$\delta_{\text{NdFeB}}$	NdFeB magnet's skin depth
$\Delta\mathbf{B}_j$	Flux density vector from a single conductor segment of the Ampèrian model
$\Delta F_{\text{EM}}$	Change of electromagnetic force
$\Delta F_{\text{PM}}$	Change of magnetic force
$\Delta F_{\text{rot}}$	Change of rotational force
$\Delta I$	Change of current in the electromagnets
$\Delta l_m$	Arc length of a mover's conductor segment of the Ampèrian model
$\Delta \mathbf{l}_m$	Direction vector of a mover's conductor segment of the Ampèrian model
$\Delta l_s$	Arc length of a stator's conductor segment of the Ampèrian model

---

$\Delta \mathbf{l}_s$	Direction vector of a stator's conductor segment of the Ampèrian model
$\Delta T_{EM}$	Change of electromagnetic torque
$\Delta T_{PM}$	Change of magnetic torque
$\Delta u_{amp}$	Change of force or eddy current sensor's amplified voltage
$\Delta x_m$	Change of mover's $x$ position
$\Delta \theta_m$	Change of mover's angle for rotations around the radial axes
$\zeta$	Damping ratio for second-order systems
$\theta_m, \Theta_m$	Mover's angle for rotations around the radial axes
$\dot{\theta}_m$	Mover's angular speed for rotations around the radial axes
$\ddot{\theta}_m$	Mover's angular acceleration for rotations around the radial axes
$\tilde{\theta}_{m,x}$	Estimated mover's angle for rotations around the $x$ axis
$\tilde{\dot{\theta}}_{m,x}$	Estimated mover's angular speed for rotations around the $x$ axis
$\theta_{m,max}$	Mover's angle at the maximum mover's radial position
$\theta_{m,x}$	Mover's angle for rotations around the $x$ axis
$\theta_{m,y}$	Mover's angle for rotations around the $y$ axis
$\theta_{m,y,max}$	Maximum angle before the mover changes stability properties
$\theta_{m,y,max}^*$	Scaled maximum angle before the mover changes stability properties
$\theta_{m,y,min}$	Minimum angle before the mover changes stability properties
$\lambda_1, \lambda_2$	Proportionality factors for scaling laws
$\mu$	Permeability
$\mu_0$	Vacuum permeability
$\mu_r$	Relative permeability
$\mu_{r,Cu}$	Copper's relative permeability
$\mu_{r,NdFeB}$	NdFeB magnet's relative permeability
$\rho$	Electrical resistivity
$\rho_{Cu}$	Copper's electrical resistivity
$\rho_{NdFeB}$	NdFeB magnet's electrical resistivity
$\varrho$	Mass density
$\sigma$	Standard deviation
$\phi$	Magnetic flux

## List of Symbols

---

$\omega_0$	Natural angular frequency of second-order systems and $G_{CL}$
$\omega_c$	Crossover frequency of $G_{OL}$
$\omega_{in}$	Bandwidth of the inner current controller
$\omega_{out}$	Bandwidth of the outer current controller

# Contents

<b>Acknowledgments</b>	<b>iii</b>
<b>Abstract</b>	<b>v</b>
<b>Sommario</b>	<b>ix</b>
<b>Abbreviations</b>	<b>xiii</b>
<b>List of Symbols</b>	<b>xv</b>
<b>1 Introduction</b>	<b>1</b>
1.1 Challenges . . . . .	3
1.2 Aims and Contributions . . . . .	4
1.3 List of Publications . . . . .	5
1.3.1 Journal Papers . . . . .	6
<b>2 Exploring the Physical Limits of Magnetic Levitation Platforms</b>	<b>7</b>
2.1 Introduction . . . . .	8
2.2 Analytical Model Description . . . . .	10
2.2.1 Ampèrian Model of Permanent Magnets . . . . .	10
2.2.2 Simplified 2D Analysis . . . . .	11
2.2.3 3D Analysis, Magnetic Flux Density Calculation . . . . .	12
2.2.4 3D Analysis, Force and Torque Calculation . . . . .	13
2.2.5 Further Considerations . . . . .	14
2.3 Passive Stability . . . . .	16
2.3.1 Displacement Method . . . . .	16
2.3.2 Passive Stability Types . . . . .	17
2.4 Dependence of Levitation Properties on MLP Dimensions . . . . .	19
2.4.1 Stability Regions and Levitation Height . . . . .	19
2.4.2 From Disc-Shaped to Ring-Shaped PMs . . . . .	21
2.5 Optimization Process . . . . .	24
2.5.1 Optimization Targets . . . . .	24
2.5.2 Multi-Objective Optimization . . . . .	26
2.6 Optimization Results . . . . .	27
2.7 Experimental Verification . . . . .	29
2.8 Scaling Laws . . . . .	33
2.8.1 Proportionality Factors . . . . .	33

2.8.2	Scaling Laws . . . . .	34
2.8.3	Example . . . . .	35
2.9	Conclusions . . . . .	37
<b>3</b>	<b>Reaction Force-Based Position Sensing for Magnetic Levitation Platform with Exceptionally Large Hovering Distance</b>	<b>38</b>
3.1	Introduction . . . . .	39
3.2	Magnetic Levitation Platform Overview . . . . .	43
3.3	Dynamics Modeling . . . . .	47
3.3.1	Radial Motion Dynamics . . . . .	47
3.3.2	Rotational Dynamics . . . . .	49
3.3.3	Force Sensor Mechanical Dynamics . . . . .	52
3.3.4	Force Sensor Electrical Dynamics . . . . .	53
3.3.5	Summary of the Dynamics . . . . .	54
3.4	Dynamic Model Verification and Tuning . . . . .	55
3.4.1	Mover's Position Controller . . . . .	56
3.4.2	Dynamic Model Proof and Adaption . . . . .	60
3.5	Observer and Controller Design . . . . .	64
3.5.1	Observer . . . . .	64
3.5.2	Mover's Position Controller and Rotation Damping . . . . .	65
3.5.3	Inverter Stage . . . . .	69
3.5.4	Position Sensor Offset Compensation . . . . .	72
3.6	Hardware Demonstrator Realization . . . . .	74
3.6.1	Force Sensor . . . . .	74
3.6.2	Controller Tuning . . . . .	76
3.6.3	Results . . . . .	78
3.7	Conclusions . . . . .	80
<b>4</b>	<b>Comparative Analysis of Force and Eddy Current Position Sensing Approaches for Magnetic Levitation Platform with an Exceptional Hovering Distance</b>	<b>82</b>
4.1	Introduction . . . . .	83
4.2	Eddy Current Position Sensor for the MLPs . . . . .	86
4.2.1	ECS Geometry and Operating Principle . . . . .	86
4.2.2	ECS Design Considerations . . . . .	89
4.2.3	Impact of Conductive Obstacles in the Air Gap . . . . .	91
4.3	Reaction Force-Based Position Sensor . . . . .	92
4.4	Dynamics Modeling and Verification . . . . .	94
4.4.1	Dynamic Model . . . . .	94
4.4.2	Dynamic Model Verification and Calibration . . . . .	97

4.5	Comparative Results . . . . .	99
4.5.1	Steady-State Levitation Comparison . . . . .	99
4.5.2	Analysis of Performance Variance . . . . .	101
4.6	Additional Experimental Results for the Eddy Current Sensor	106
4.6.1	Disturbance During Steady-State Levitation . . . . .	106
4.6.2	Position Reference Tracking . . . . .	108
4.6.3	Position Reference Tracking with Payload . . . . .	110
4.7	Conclusions . . . . .	113
<b>5</b>	<b>Conclusion and Outlook</b>	<b>114</b>
5.1	Summary . . . . .	114
5.2	Outlook . . . . .	115
	<b>Appendices</b>	<b>117</b>
<b>A</b>	<b>Design of the Electromagnets</b>	<b>119</b>
A.1	Positioning Analysis . . . . .	119
A.2	Multi-Turn Electromagnet . . . . .	121
A.3	Hardware Realization of the Electromagnets . . . . .	125
	<b>Bibliography</b>	<b>129</b>
	<b>Curriculum Vitae</b>	<b>140</b>

# 1

## Introduction

**A**LREADY in the late 1980s and 1990s, studies on hybrid magnetic bearing technologies (“bearingless motors” utilizing passive and active stabilization of the degrees of freedom of the moving part/rotor) were carried out at D-ITET/ETH Zurich and constituted a key research topic. These works are early precursors of this thesis, which aims to extend the levitation distance between permanent magnets (PMs) constituting the passive part of magnetic levitation platforms (MLPs), i.e., axial hybrid magnetic bearings. This ambitious objective has rarely been researched despite its potential for exciting applications in mechatronic systems.

Within the framework of previous projects conducted at the Power Electronic System Laboratory (PES) of D-ITET, research in the fields of hybrid magnetic bearings was pushed further with a focus on specific applications. Fundamental properties were clarified, multi-objective optimizations were performed, and demonstrator systems were realized. Research results include magnetic bearings enabling ultra-high rotational speeds (up to 500 krpm [1]) of permanent magnet synchronous machines, as used in turbocompressors, machining spindles, gas turbine generators, flywheels, and scanners; magnetically supported drives used in hermetically sealed chambers for wafer processing in the semiconductor industry [2]; and bearingless slice motors in exterior rotor construction employed for mixing solutions in bioreactors in pharmaceutical, chemical, and food industries [3] (see **Fig. 1.1 (a)**). However, research in this area was limited to systems with air gaps one to two orders of magnitude smaller than the system’s characteristic dimension, defined as the largest dimension of the MLP’s mechanical components.

MLPs featuring exceptionally large air gap distances, i.e., distances in the same order of magnitude as the system’s characteristic dimension, would extend current applications, such as the contactless support, transport, or



rotation of objects within hermetically sealed process chambers. The extraordinary large air gap allows levitating the object far from the chamber's walls or enables the use of thick walls, or the considerable magnetic force allows equipping the levitated magnet with heavy additional payloads. However, to overcome the limitation concerning the air gap width by at least one order of magnitude, completely new design and modeling approaches are required, which motivate this thesis. Besides the electromagnetic design of the contactless MLP, the development of a suitable position sensor system represents a unique challenge since the operation must be ensured without direct sight of the levitated magnet.

In general, commercially available “magnetic levitation modules” as shown in **Fig. 1.1 (b)** are formed by

- ▶ two axially arranged PMs designed to achieve specific passive bearing forces,
- ▶ position sensors that detect displacements of the levitated PM, and
- ▶ a set of electromagnets (EMs) that generate additional magnetic flux density components, which generate forces on the levitated PM and accordingly allow controlling its position.

These commercial products typically achieve air gap length to characteristic dimension ratios below 1:4, which should be increased to at least 1:2 in this thesis. Different sensing concepts are employed today depending on the distance between the two PMs. Hall effect sensors [6] are often used for relatively small air gaps since they offer sufficient sensitivity for the active position control of the levitated PM (mover). However, considering the substantial decay of the magnetic field strength with increasing distance, a significant amplification of the sensed signal would be required for larger air gaps. On the contrary, large amplification is not applicable due to the high magnetic field near the steady PM (stator) for preventing saturation. Therefore, other sensing techniques are used, such as optical [7] and eddy current sensors [8]. Optical sensors are more precise than the other sensing methods but cannot be employed in cases where obstacles such as shields, walls, or enclosures used to isolate the mover from the rest of the system are present in the air gap. In comparison, eddy current sensors can be applied in a more extensive variety of systems, given that the separation surface between stator and mover is non-conductive. This thesis must conceive a different positioning concept that enables stable levitation at large distances, irrespective of the material inserted in the air gap. Furthermore, the payload

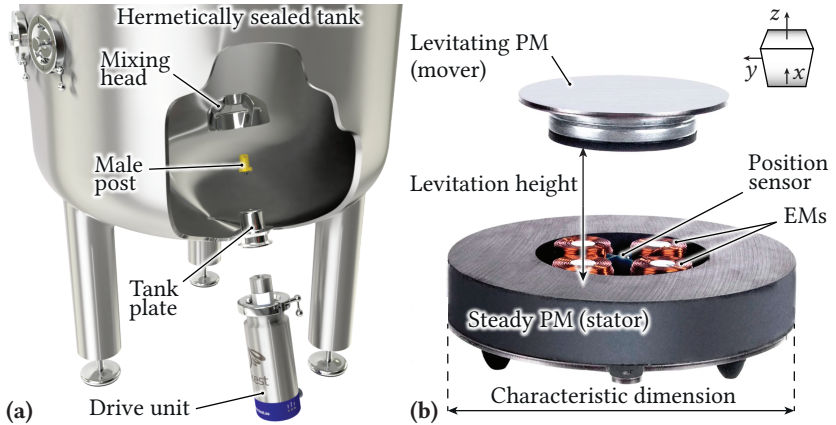


**Fig. 1.1:** (a) Magnetically coupled mixer from [4] used in pharmaceutical, chemical, and food industries. (b) Commercially available magnetic levitation module from [5] showing the core components and the relevant dimensions of the investigated axial MLP.

that commercial MLPs can handle is limited to about four times the mass of the mover. Therefore, substantially larger levitation forces must be generated to levitate and eventually manipulate heavy objects at large levitation heights inside a hermetically sealed process chamber.

## 1.1 Challenges

In the first step, the interaction and optimal design of the MLP's PMs will be investigated in detail. According to Earnshaw's theorem, it is impossible to passively stabilize all degrees of freedom (DOFs) of the mover. Depending on the PMs' dimensions, different stability regions for a set of DOFs and stability types, i.e., axial, radial, or rotation stability, are observed. Hence, besides aiming for the maximum physically achievable levitation height, the stability type resulting in the maximum number of passively stable DOFs is pursued. This stability type is characterized by restoring axial forces and radial torques that passively prevent the mover from displacing along the axial axis  $z$  and rotating around the radial axes  $x$ ,  $y$ . Consequently, only the mover's radial displacement is passively unstable, implying that the realization effort of the position sensing and the related active control are minimized. For the

active position control of the mover, an appropriate actuation system must be designed to efficiently generate the required stabilizing force, even over large distances. Therefore, the amount, shape, position, and design of actuator coils must be optimized. Moreover, the relation with the power electronic converter impressing the required actuation current must be considered in this context.

An attractive position-sensing solution is to capture the position of the mover by measuring the reaction forces between the levitated and stationary PMs. A three-axes force sensor supporting the stator measures the radial forces due to the unstable mover's radial displacement and the axial force in case of dynamic payload changes on the mover. A mover's rotation around the  $x$ ,  $y$  axes is always coupled with the radial displacement due to destabilizing magnetic and stabilizing electromagnetic forces, contributing to the total measured force. Therefore, a sophisticated control algorithm is required, where an observer based on the dynamical model of the complete MLP extracts the radial position from the sensed forces so that it can be actively regulated. However, due to the considerable relative levitation height, more than the passive dynamic damping of the mover's rotation is required to achieve a complete system's stability. Hence, the position controller is augmented to actively enhance rotation damping with the already available observed mover's angle.

Finally, the performance of the MLP is evaluated and compared using the force sensor and a custom eddy current sensor. The main design challenge for the eddy current sensor is achieving sufficient magnetic field coupling within its electromagnetic coils. The coupling diminishes with greater distance between the coils, whose dimensions are limited by the components constituting the MLP to have a fair comparison with the force sensor system. Moreover, the neighboring electrically conductive components (stator, mover, and EMs) influence the magnetic field distribution in space, necessitating an accurate placement of the eddy current sensor's coils.

## 1.2 Aims and Contributions

As already highlighted, the primary goal of this thesis is to elaborate a new sensing concept for the mover's position to achieve a functional levitation in situations where the mover is encapsulated in an electrically conductive sealed chamber and levitated at extremely large distances from the stator. The MLP system should be designed, realized, and experimentally verified in hardware as the ultimate goal. The contributions of this thesis to enrich the

understanding of axial MLPs featuring large levitation heights are listed in the following.

- ▶ **Chapter 2** presents an analytical method to calculate the static magnetic forces and torques between PMs in three-dimensional space. This fast calculation method enables a rapid multi-objective optimization of the PMs' dimensions. In the same context, scaling laws of PMs to enhance the air gap or improve the payload capability are presented, permitting the redesign of the PMs from the results of a single optimization process.
- ▶ In **Chapter 3**, the novel usage of a force sensor for the mover's position sensing and control dictates a deep investigation of the complete MLP. The dynamics of the mover, EMs, and force sensor are modeled to permit the implementation of an observer for extracting the mover's radial position and angle from the sensed forces. A measurement method to verify the proposed model is presented. Finally, a position controller design that regulates the mover's radial position and actively dampens the mover's rotations around the radial axis is discussed and experimentally verified.
- ▶ **Chapter 4** highlights the differences between the force sensor and an eddy current sensor, both used for the position control of the mover in the same MLP. The sensors are compared regarding their sensing principles, implementation challenges within the MLP, and performance, calculating the standard deviation of the mover's position from a static reference. Furthermore, the eddy current sensor shows the controller's dynamic position tracking capability and the MLP's operation with a payload on the mover. Finally, the theoretical considerations are comprehensively verified experimentally.

**Chapter 5** concludes the thesis by summarizing the findings and looking at further research on the analyzed MLP.

Additionally, **Appendix A** analyzes the positioning and design of the EMs, knowing the optimized PM geometry and the voltage/current ratings of the power electronic converter.

## 1.3 List of Publications

Key insights presented in this thesis have already been published or will be published in international scientific journals, conference proceedings, or

presented at workshops. The publications created as part of this thesis, or also in the scope of other related projects, are listed below.

### 1.3.1 Journal Papers

- ▶ R. Bonetti, D. Bortis, L. Beglinger and J. W. Kolar, “Exploring the Physical Limits of Axial Magnetic Bearings Featuring Extremely Large Vertical Levitation Distances,” *IEEE Transactions on Industry Applications*, vol. 57, no. 6, pp. 6931-6943, November-December 2021. DOI: [10.1109/TIA.2021.3096170](https://doi.org/10.1109/TIA.2021.3096170).
- ▶ R. Bonetti, L. Beglinger, S. Mirić, D. Bortis, and J. W. Kolar, “Reaction Force-Based Position Sensing for Magnetic Levitation Platform with Exceptionally Large Hovering Distance,” *Actuators*, vol. 13(3), no. 114, pp. 1-31, March 2024. DOI: [10.3390/act13030114](https://doi.org/10.3390/act13030114).
- ▶ R. Bonetti, S. Mirić, and J. W. Kolar, “Comparative Analysis of Force and Eddy Current Position Sensing Approaches for Magnetic Levitation Platform with an Exceptional Hovering Distance,” *Actuators*, vol. 13(4), no. 122, pp. 1-22, March 2024. DOI: [10.3390/act13040122](https://doi.org/10.3390/act13040122).

Moreover, the author had the pleasure to contribute to the following journal paper:

- ▶ P. Niklaus, R. Bonetti, C. Stäger, J. W. Kolar, D. Bortis, “High-Bandwidth Isolated Voltage Measurements with Very High Common Mode Rejection Ratio for WBG Power Converters,” *IEEE Open Journal of Power Electronics*, vol. 3, pp. 651-664, September 2022. DOI: [10.1109/OJPEL.2022.3208693](https://doi.org/10.1109/OJPEL.2022.3208693).

# 2

## Exploring the Physical Limits of Magnetic Levitation Platforms

This chapter summarizes the most relevant findings of the exploration of magnetic levitation platforms regarding the levitation height and passive stability properties that are also published in:

- ▶ R. Bonetti, D. Bortis, L. Beglinger and J. W. Kolar, “Exploring the Physical Limits of Axial Magnetic Bearings Featuring Extremely Large Vertical Levitation Distances” *IEEE Transactions on Industry Applications*, vol. 57, no. 6, pp. 6931-6943, November-December 2021.

### Chapter Abstract

This chapter provides an analytical method, based on the Ampèrian model of permanent magnets (PMs), for a fast calculation of the magnetic flux density in three-dimensional space applying Biot-Savart's law and the calculation of the forces using Lorentz's law. The applied approach enables the characterization of forces, torques, and stiffnesses of the levitating PM for any arbitrary position in space. Furthermore, it permits the extension of the investigation to any shape and configuration of ironless magnetic levitation platforms (MLPs). To demonstrate the simple use of the analytical model, the dimensions of an ironless MLP employing PMs are optimized with a multi-objective Pareto analysis, which reveals the physical limits concerning the maximum achievable levitation height under given constraints on the required axial/radial and rotational stiffnesses, and the axial robustness defined by the maximum allowable payload on the levitating magnet. Moreover, the optimized MLP and a corresponding test bench are realized to validate the proposed model with experimental results. For completeness, it should be mentioned that in a later stage, the optimized MLP can be scaled with simple scaling laws if the demanded specifications change, e.g., concerning desired maximum levitation height or payload capability.

## 2.1 Introduction

Magnetic levitation platforms (MLPs) consisting of axially arranged permanent magnets (PMs) and/or electromagnets (EMs) are used, e.g., in suspension devices [9], in blood pumps [10], or in positioning applications where objects are levitated in the vertical direction [11], and in certain cases with extremely large levitation heights [7, 12] (see **Fig. 2.1**). Future applications could, e.g., be found in the non-touch charging of drones and robotics or in manipulating objects inside a hermetically sealed process chamber. Such PM/EM arrangements have been analyzed in the literature [13–23], where analytical equations for the resulting axial forces are derived. However, these closed-form equations are only valid for symmetric arrangements. Investigating the passive system's stability, stiffness, and robustness is not possible when analyzing purely symmetric arrangements since the forces and torques at a certain radial displacement must be known for these calculations. Therefore, time-consuming 3D FEM simulations have to be performed, where different possible MLP geometries are iterated to obtain the optimal MLP design.

As an alternative, in this chapter, a simple analytical method based on the Biot-Savart law is proposed in **Section 2.2**, which allows calculating the resulting forces and torques for any ironless non-symmetric 3D PM/EM geometry by substituting all PMs with equivalent current-carrying coils, so that

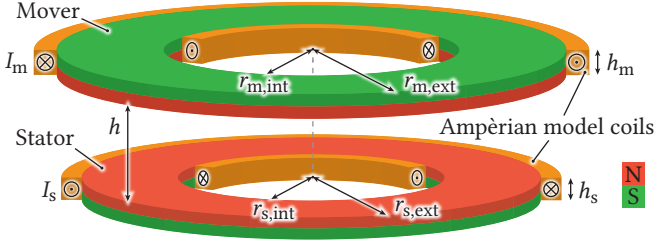


**Fig. 2.1:** General MLP arrangement with ring-shaped PMs, where the equivalent current-carrying coils are shown.

the magnetic flux density distribution is replicated with sufficient accuracy. In contrast to [24], where the Ampèrian model is successfully applied to a simple linear Halbach array, the shape of the PMs does not constrain the suggested method since the path of the Ampèrian model coils is discretized into short linear segments. Nonetheless, it is applied to an ironless magnetic levitation platform constituted by PMs with axial magnetization, as illustrated in **Fig. 2.1**. For instance, a similar arrangement with PMs and electromagnets, which could be analyzed with the proposed method, is found in motors featuring ironless coil units [25] where the back iron parts are explicitly omitted to eliminate attraction or cogging forces between PMs and iron cores and to achieve superior positioning precision and fast dynamics with high acceleration and deceleration capabilities. Further applications are, e.g., found in weight-optimized ironless flywheels where Halbach arrays are employed [26]. Moreover, the considered analytical model could be combined with the method of images [27] to determine the magnetic forces and torques in magnetic bearings and motors incorporating PMs and simple structures of magnetic materials. For example, the method of images was applied in [28] in combination with the surface charge model of PMs [27] to calculate the radial and axial magnetic forces in a magnetic bearing of a highly reliable fan, or it is used to design a suspension system for a micro-lithography application where precise movements are required [29].

In this thesis, the purpose of using PMs in the MLP is to generate large passive vertical forces, which result in an efficient levitation of the levitating PM, hereinafter called mover. However, as stated by Earnshaw's theorem [30] (**Section 2.3**), a passive stabilization of each degree of freedom (DOF) of the mover is not possible. Therefore, a proper integration of EMs is essential to actively control the remaining unstable DOFs of the mover and stabilize



its position. The design of the EMs is not further discussed in this chapter; however, in **Section 2.4**, it is shown that the selected dimensions of the MLP and the relative magnetization direction between the two PMs define which and/or how many DOFs remain unstable. Hence, different passive stability types depending on the number of passively stable DOFs and stiffnesses are defined in **Section 2.4**.

To demonstrate the simple use of the analytical model, in **Section 2.5**, the MLP is optimized such that the maximum possible levitation height is achieved for given constraints as the rotational stiffness and the maximum payload the mover can carry. As shown in **Section 2.6**, for a minimum rotational stiffness of  $1 \text{ mNm}/^\circ$  and a demanded payload capability of 50 times the mover's weight, the optimized MLP features a maximum diameter of 130 mm, i.e., the characteristic dimension of the passive MLP, a maximum magnet height of 21 mm, and a payload capability of 17 kg. Moreover, it is found that a characteristic dimension-related levitation height (CDRLH) close to 1.0 is achieved, outperforming existing commercial systems, which show CDRLHs around 0.6 [7], where the levitation height is only 60 % of the characteristic dimension.

Further, in **Section 2.7**, the performance of the MLP is tested on a 6 DOF platform, where the stationary PM (stator) is brought into different positions and distances relative to the mover to verify the analytically calculated forces and torques experimentally.

For completeness, instead of iterating through all possible combinations in the Pareto optimization, in **Section 2.8**, scaling laws are derived from the analytical equations which directly allow calculating the resulting forces, torques, stiffnesses, and levitation height for a scaled version of the characterized MLP.

## 2.2 Analytical Model Description

### 2.2.1 Ampèrian Model of Permanent Magnets

As described in [31] and applied in [22, 24], to replicate the magnetic field generated by the axially-magnetized ring-shaped PMs, current-carrying coils with the same inner and outer radius and the same height as the PMs can be used (see **Fig. 2.1**). The polarity of the PMs gives the current direction, whereas the amplitudes  $I_s$  and  $I_m$  are determined with Ampère's law as [32]

$$I_i = \frac{H_{ci,i} \cdot h_i}{N_i} \quad \text{with } i = \{s, m\}, \quad (2.1)$$

where  $H_{ci,i}$  is the coercive field (955 kA/m for the investigated Neodymium-Iron-Boron magnets),  $h_i$  is the height of the PM, and  $N_i$  is the number of turns of the model coil.

In the following, a lumped single-turn coil ( $N_i = 1$ ) located at the center of the height  $h_i$  is assumed for the approximation of the PM's magnetic flux density (see **Fig. 2.2** and **Fig. 2.4 (a)**). This choice leads to the lowest computational effort with sufficient accuracy for the far-field calculation. To improve the accuracy of the near field calculation, a distributed multi-turn coil along the total height  $h_i$  is possible (**Fig. 2.4 (b)**), which consequently implies an increased computational effort.

### 2.2.2 Simplified 2D Analysis

The internal radii  $r_{m,int}$  and  $r_{s,int}$  of the two ring-shaped PMs are assumed to be zero to introduce the proposed analytical method. Hence, the most simple MLP configuration with two disc-shaped PMs is obtained as depicted in **Fig. 2.2** as a cross-section view.

For this axially symmetric arrangement, a simplified 2D analysis can be conducted, where each of the two PMs is substituted by two straight and infinitely long conductors carrying the same current  $I_{i1} = I_{i2}$  in opposite directions. Based on Ampère's law, the magnetic flux density generated by each of the two stator conductors is determined for each position in space and decays with  $1/r$ , where  $r$  is the distance from the considered stator conductor to the magnetic flux density evaluation point. Based on the right-hand rule, the magnetic flux density always points in the tangential direction with respect

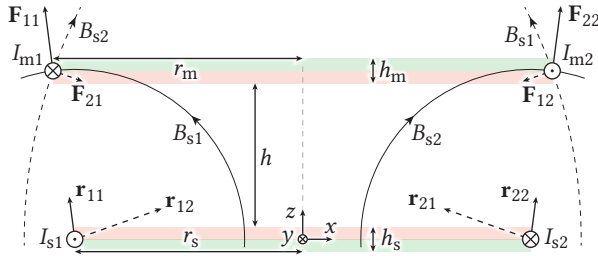


**Fig. 2.2:** Cross-section view of two disc-shaped PMs (see **Fig. 2.1** with  $r_{m,int} = r_{s,int} = 0$ ), explaining the Lorentz forces acting on the mover coils. Both conductors modeling the stator PM generate a force on both conductors modeling the mover PM, whose direction is determined by the right-hand rule.

to  $\mathbf{r}$  (see Fig. 2.2). Hence, the Lorentz force acting on each mover conductor is directly determined by the superposition of the two force components resulting from the two stator conductors. There, the force vector always lies in the connection line between the considered stator and mover conductors and, depending on the current directions, results in an attractive or repulsive force (see Fig. 2.2). Consequently, the total force acting on the mover is the sum of each force contribution, i.e.,  $\mathbf{F}_{\text{tot}} = \mathbf{F}_{11} + \mathbf{F}_{12} + \mathbf{F}_{21} + \mathbf{F}_{22}$ . For this symmetric case, the total force only acts in the axial direction because the  $xy$ -force components cancel each other out. However, in a more general case, where the mover is displaced from the center in the  $x$  direction,  $\mathbf{F}_{\text{tot}}$  results in a net force component acting in the  $x$  direction. In addition, the  $z$ -force components acting on each of the two mover conductors are not equal, meaning that a torque in the  $y$  direction is created. Consequently, the mover experiences a horizontal displacement in the  $x$  direction while rotating around the  $y$  axis.

The 2D analysis of this general case is only valid for infinitely long and straight conductors and can be applied to approximately calculate the forces for axially symmetric arrangements. Hence, to investigate arbitrary configurations with displaced or rotated movers, an analytic 3D analysis has to be performed.

### 2.2.3 3D Analysis, Magnetic Flux Density Calculation

In a homogeneous medium, the Biot-Savart law allows calculating the magnetic flux density vector  $\mathbf{B}$  at any point in 3D space generated by a conductor carrying the current  $I_s$  as

$$\mathbf{B} = \frac{\mu}{4\pi} \int_C \frac{I_s d\mathbf{l}_s}{r^2} \times \frac{\mathbf{r}}{r}, \quad (2.2)$$

where  $\mu = \mu_r \mu_0 = \mu_0$  is assumed in the following. There,  $d\mathbf{l}_s$  is the vector representing an infinitesimally small piece of conductor pointing in the direction of the current  $I_s$ , and  $\mathbf{r}$  is the distance vector between the considered piece of conductor and the evaluation point of the magnetic flux density. In the case of a circular conductor, the solution of (2.2) contains elliptic integrals that need to be evaluated with numerical integration [33–35]. According to [36], the approach used in this chapter is to approximate the integral of (2.2) with a finite sum of field components, such that the magnetic flux density generated by any current-carrying conductor can be calculated. Accordingly, the single-turn mover and stator coils are discretized in a finite number  $N_{\text{pts}}$

of conductor segments with length  $\Delta l_i$ , which are represented by their corresponding center points as shown in **Fig. 2.3**.

Hence, to calculate the magnetic flux density at the center points of each mover segment, the magnetic flux density contribution of each stator segment has to be evaluated as

$$\Delta \mathbf{B}_j = \frac{\mu_0}{4\pi} \cdot \frac{I_s \Delta \mathbf{l}_s}{r^2} \times \frac{\mathbf{r}}{r}, \quad (2.3)$$

where the length of the vector  $\Delta \mathbf{l}_s$  is given by the linear distance between two adjacent center points on the stator winding, and its direction is determined by the direction of the current  $I_s$  at the corresponding center point, i.e., always tangential to the circular winding. The distance vector  $\mathbf{r}$  equals the distance between the considered center points.

Accordingly, the total magnetic flux density acting on one mover segment's center point is given by

$$\mathbf{B} = \sum_{j=1}^{N_{\text{pts}}} \Delta \mathbf{B}_j = \frac{\mu_0}{4\pi} \sum_{j=1}^{N_{\text{pts}}} \frac{I_s \Delta \mathbf{l}_s}{r^2} \times \frac{\mathbf{r}}{r}. \quad (2.4)$$

### 2.2.4 3D Analysis, Force and Torque Calculation

Knowing the magnetic flux density at each mover segment's center point, the Lorentz force  $\mathbf{F}_k$  acting on each mover segment (**Fig. 2.3**) is calculated to

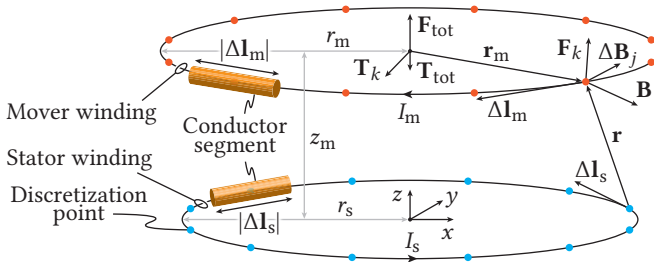


**Fig. 2.3:** Discretization of the Ampèrian model coils of **Fig. 2.1** for  $r_{m,\text{int}} = r_{s,\text{int}} = 0$  and  $N_s = N_m = 1$ , where the magnetic flux density, forces, and torques are reported.

determine the total force applied the mover as

$$\mathbf{F}_{\text{tot}} = \int I_m d\mathbf{l}_m \times \mathbf{B} \approx \sum_{k=1}^{N_{\text{pts}}} \mathbf{F}_k = \sum_{k=1}^{N_{\text{pts}}} I_m \Delta \mathbf{l}_m \times \mathbf{B}. \quad (2.5)$$

Accordingly, the total torque referenced to the center of the mover is calculated by summing the radius-force products of each mover point, i.e.,

$$\mathbf{T}_{\text{tot}} = \sum_{k=1}^{N_{\text{pts}}} \mathbf{T}_k = \sum_{k=1}^{N_{\text{pts}}} \mathbf{r}_m \times \mathbf{F}_k, \quad (2.6)$$

where  $\mathbf{r}_m$  is the radius vector pointing from the center of the mover to a discretization point on the mover winding.

The number of discretization points  $N_{\text{pts}}$  determines the precision of the finite sum approximation and the required computation time. For  $N_{\text{pts}} \gg 1$ , the force/torque error decays exponentially with  $N_{\text{pts}}$ . Instead, the computation time grows quadratically with  $N_{\text{pts}}$  because for the magnetic flux density calculation of each mover segment, each stator segment has to be considered. Consequently, a discretization of  $N_{\text{pts}} = 100$  was chosen, which reveals a sufficient accuracy at a moderate computational effort.

### 2.2.5 Further Considerations

In a case where the stator and mover are realized as ring-shaped PMs, four model coils with radius  $r_{s,\text{int}}$ ,  $r_{s,\text{ext}}$ ,  $r_{m,\text{int}}$ , and  $r_{m,\text{ext}}$  are required, where the currents in the inner and outer coil of each ring-shaped PM are pointing in opposite direction (see **Fig. 2.1**). In the simplest case, where single-turn coils are considered (**Fig. 2.4 (a)**), the calculation of the forces and torques has to be conducted for all combinations of coil pairs, where a stator and a mover coil constitute a pair.

As already mentioned, the accuracy of the simulated magnetic flux density distribution depends on the coil's number of turns  $N_i$  and the distance  $h$  between the PMs (see **Fig. 2.4**). Especially in the near field region, a distributed multi-turn coil (**Fig. 2.4 (b)**) results in a more accurate field calculation compared to the lumped single-turn coil (**Fig. 2.4 (a)**). Hence, the multi-turn approach must be used for relatively small distances  $h$  compared to  $h_i$  ( $h \ll h_s, h_m$ ). Thus, the forces and torques between each stator and mover turn have to be calculated, which means that the computational effort for the

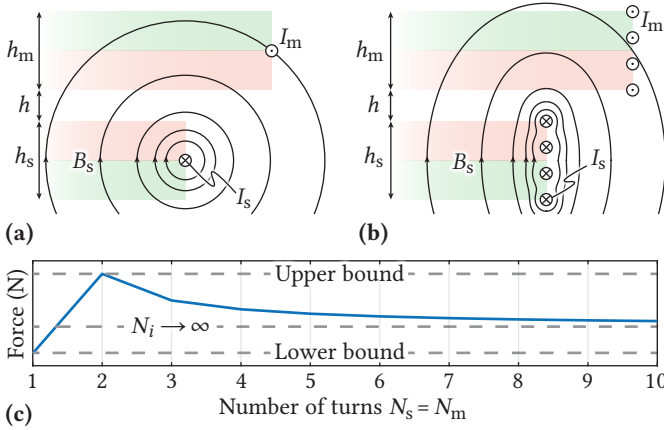


**Fig. 2.4:** Magnetic flux density distribution of the stator PM in a 2D plane for the case  $h \ll h_s, h_m$  with **(a)** single-turn model coils  $N_s = N_m = 1$  and **(b)** multi-turn model coils  $N_s = N_m = 4$ . **(c)** Example of force calculation for different numbers of model turns  $N_s$  and  $N_m$  considering the same MLP, where it is visible that the single and double-turn models define the bounds for all other force calculations with  $N_s = N_m \geq 3$ .

multi-turn winding approach increases by  $N_s \cdot N_m$ , compared to the single-turn approach. For the considered MLP, where extremely large levitation heights are pursued, i.e.,  $h \gg h_s, h_m$ , the single and the multi-turn models result in a similar far-field distribution; thus, similar forces and torques are obtained as shown later in **Fig. 2.6**, **Fig. 2.14** and **Section 2.6**. This justifies the described procedure, where the single-turn coil approach is used for a coarse Pareto optimization to speed up the computation time, whereas in a second step, the force and torque calculation is refined to obtain precise results (see **Fig. 2.14 (b)-(d)**).

Furthermore, there is an interesting fact that the single-turn ( $N_s = N_m = 1$ ) and the double-turn model ( $N_s = N_m = 2$ ) define the bounds for the calculated forces and torques, whereas the multi-turn models with  $N_s = N_m \geq 3$  yield values between these bounds. The calculation error decays with an increasing number of model turns as it is shown in **Fig. 2.4 (c)** for a particular case with randomly selected values for  $h$ ,  $h_s$ , and  $h_m$  and as verified later for the force calculations of the optimal MLP (see **Fig. 2.14**).

## 2.3 Passive Stability

The derived analytical method enables an extensive analysis of the mover's behavior in 3D space. Therefore, in the first step of the design process, the passive stability of the mover, i.e., the DOFs that are already passively stable only due to the presence of the PMs, is analyzed for its nominal operating or levitation position. As stated by Earnshaw's theorem [30], not all six DOFs of the mover (see Fig. 2.5 (a)) can be stabilized passively. However, as shown in the following, depending on the selected dimensions of the MLP, different stability types with different numbers of passively stable DOFs or different properties concerning stiffnesses are obtained. In the end, a stability type that enables a high levitation height and minimizes the sensing and control effort of the EMs to control the remaining unstable DOFs actively should be selected.

### 2.3.1 Displacement Method

The method to determine the passively stable DOFs of the mover is to displace the mover from a nominal levitation position and to compute all forces and the torque for this position. These values determine the corresponding force and torque gradients for each DOF. A negative gradient value, i.e., a force or torque acting in the opposite direction to the displacement or rotation, is associated with a stable equilibrium. In contrast, a positive gradient value indicates an unstable equilibrium. The magnitude of the gradient is defined as stiffness, which characterizes the dynamic behavior of the mover around the equilibrium. A gradient that equals zero means that the equilibrium is marginally stable, i.e., neither stable nor unstable.

The axial force gradient  $dF_z/dz_m$  is determined by calculating the change of force  $dF_z$  for a certain displacement  $dz_m$  of the mover in the  $z$  direction

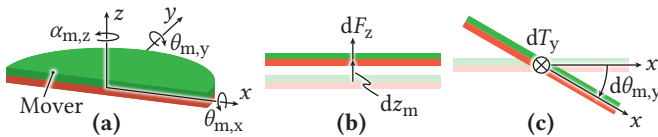


**Fig. 2.5:** (a) Illustration of the mover's six DOFs with its local coordinate system spanned by  $(x, y, z)$ , where a translation and a rotation along each axis is possible. (b) Axial displacement of the mover needed to calculate the gradient  $dF_z/dz_m$ . (c) Rotation around the  $y$  axis of the mover needed to calculate the gradient  $dT_y/d\theta_{m,y}$ .

(**Fig. 2.5 (b)**). Similarly, to calculate the torque gradient of a rotational DOF, the mover is rotated as illustrated in **Fig. 2.5 (c)** to obtain the torque gradient, as shown for  $dT_y/d\theta_{m,y}$ . For calculating the radial force gradient, the mover's rotation around the radial axes must be considered because magnetic torques rotating the mover around the  $x$ ,  $y$  axes occur for radial positions different from zero. When rotational stability is ensured (negative torque gradient),  $dF_x/dx_m$  is calculated by displacing the mover in the  $x$  direction by  $dx_m$  and rotating it around the  $y$  axis by the angle  $\theta_{m,y}$  that cancels the torque in the  $y$  direction. When the mover reveals rotational instability (positive torque gradient),  $dF_x/dx_m$  is calculated by displacing the mover by  $dx_m$  and assuming that the mover is kept horizontal ( $\theta_{m,y} = 0$ ) with active control. The two procedures to calculate  $dF_x/dx_m$  assume that the mover's axial position remains unchanged for the displacement  $dx_m$  and the eventual rotation  $\theta_{m,y}$ , but ensure that the force gradients are calculated under the real mover's rotational behavior.

### 2.3.2 Passive Stability Types

The force and torque gradients and stiffnesses are now analyzed for the MLP. If the mover is located at its nominal radially centered position  $x_m = y_m = 0$  at a certain height  $h$  (the MLP is axially symmetric), the following holds

$$F_x = F_y = 0 \quad (2.7) \quad dF_x/dx_m = dF_y/dy_m \quad (2.10)$$

$$T_x = T_y = 0 \quad (2.8) \quad dT_x/d\theta_{m,x} = dT_y/d\theta_{m,y} \quad (2.11)$$

$$T_z = 0 \quad (2.9) \quad dT_z/d\alpha_{m,z} = 0. \quad (2.12)$$

In contrast to the general case, (2.10), (2.11), and (2.12) imply that the stability properties for the axially symmetric MLP can be derived with a reduced computation time, since only three gradients have to be determined, i.e.,  $dF_x/dx_m$ ,  $dF_z/dz_m$ , and  $dT_y/d\theta_{m,y}$ . Another direct implication of (2.12) is the marginal stability of the torque in the axial direction. Thus, the rotation around the axial axis (indicated by the angle  $\alpha_{m,z}$ ) is marginally stable and must not be stabilized actively at the cost of a continuous rotation around the  $z$  axis once initiated.

Furthermore, as explained in [30] and applied in [9, 13, 14, 28], the divergence of the force vector between permanent magnets in a homogeneous medium is given as

$$\nabla \cdot \mathbf{F} = \frac{dF_x}{dx_m} + \frac{dF_y}{dy_m} + \frac{dF_z}{dz_m} = 0, \quad (2.13)$$



which in combination with (2.10) results in

$$\frac{dF_z}{dz_m} = -2 \cdot \frac{dF_x}{dx_m}. \quad (2.14)$$

It is essential to mention that (2.13) and (2.14) hold for axially symmetric MLPs where the mover is kept parallel to the stator, i.e., where  $\theta_{m,x} = \theta_{m,y} = 0$ , which is only possible when active control regulates the mover's angle. The proposed analytical model does not rely on axial symmetry assumptions; however, the relations (2.7)-(2.14) have been observed as a result of the calculations.

Consequently, when the angles  $\theta_{m,x}$  and  $\theta_{m,y}$  are controlled to zero actively, (2.14) excludes simultaneous stability of all three force components, i.e., passive force stability is only possible either in the axial or radial direction. A passive stability type with only rotational stability is possible when the mover is free to rotate because the corresponding active control is disregarded, i.e., (2.14) is invalid. Accordingly, considering the restrictions given for axially symmetric MLPs with both magnets radially centered, five types of passive stability exist:

- I. ( $F_z$ ): the mover is stable against axial displacements (one DOF is passively stable, and four DOFs must be controlled actively);
- II. ( $F_{xy}$ ): the mover is stable against radial displacements if  $\theta_{m,x} = \theta_{m,y} = 0$  (two DOFs are passively stable, and three DOFs must be controlled actively);
- III. ( $T_{xy}$ ): the mover is stable against rotations around the  $y, x$  axes (two DOFs are passively stable, and three DOFs must be controlled actively);
- IV. ( $F_z, T_{xy}$ ): in addition to ( $F_z$ ), the mover is stable against rotations around the  $x, y$  axes (three DOFs are passively stable, and two DOFs must be controlled actively);
- V. ( $F_{xy}, T_{xy}$ ): the mover is stable against radial displacements if  $\theta_{m,x} = \theta_{m,y} = 0$  and it is stable against rotations around the  $x, y$  axes (four DOFs are passively stable, but the rotation must be actively controlled to zero and one DOF must be controlled actively).

( $F_{xy}, T_{xy}$ ) exhibits four passively stable DOFs; however, the condition  $\theta_{m,x} = \theta_{m,y} = 0$  must be met to ensure that the mover is stable against radial displacements, meaning that active control of the two passively stable rotational

DOFs must be implemented. Therefore, the stability type  $(F_{xy}, T_{xy})$  reduces to  $(F_{xy})$  since active control of three DOFs (the axial displacement and the rotations around the radial axes) is required.

As a result,  $(F_z, T_{xy})$  offers the lowest number of DOFs that must be controlled actively, translating to a simpler design of the active controller.

## 2.4 Dependence of Levitation Properties on MLP Dimensions

Now, the question is how the MLP must be designed to obtain a specific stability type with a high stiffness. This section addresses this question with a design example of two disc-shaped PMs with opposing magnetization directions. The mover's external radius  $r_{m,ext}$  is used as a variable, whereas the other dimensions are chosen as  $r_{s,ext} = 50$  mm,  $r_{s,int} = r_{m,int} = 0$  mm,  $h_s = 10$  mm, and  $h_m = 5$  mm. In the following, it is shown that different stability types are obtained with different  $r_{m,ext}$ . Furthermore, it is highlighted that the passive rotational stiffness of the mover improves using ring-shaped instead of disc-shaped PMs.

### 2.4.1 Stability Regions and Levitation Height

The first step of the design example is to determine the stability type obtained for different  $r_{m,ext}$  and levitation heights  $h$  combinations, while the mover's radial position is always kept to zero. **Fig. 2.6 (a)** shows the resulting stability types derived with the displacement method for each  $r_{m,ext}$ - $h$  combination. It is visible that the preferred stability type  $(F_z, T_{xy})$ , in the orange region, is obtained for  $r_{m,ext} \geq 36$  mm. It should be mentioned that the colored regions have been generated with the fast model ( $N_s = N_m = 1$ ), and the boundaries between the regions have been proven to be satisfyingly precise with the multi-turn model  $N_s = N_m = 4$  as indicated with white lines. To complete the picture, the levitation height  $h$  at which the mover passively settles is found for the case where the axial force  $F_z$  is equal to the gravitational force  $F_g$  of the examined PM, i.e.,  $F_z = F_g$ , as indicated in **Fig. 2.6 (a)** with a dashed curve. With the smallest considered mover's radius  $r_{m,ext} = 1$  mm, the largest levitation height of  $h_{max} = 137$  mm is achieved. At this design point, only  $F_z$  is passively stable, meaning that rotations and radial displacements of the mover must be actively controlled. Moreover, only low axial forces  $F_z$  and low MLP stiffnesses are achieved. Therefore, it is beneficial to choose a

design point in the orange region ( $F_z, T_{xy}$ ), where at the expense of a certain levitation height reduction (at least 11.7%), passive rotational stability in the  $x, y$  directions is gained, such that only the mover's radial displacements in the  $x, y$  directions must be actively controlled.

With a further increase of  $r_{m,ext}$ , the levitation height  $h$  continuously decreases and for  $96 \text{ mm} \leq r_{m,ext} \leq 118 \text{ mm}$ , two operating points with  $F_z = F_g$  are found. To explain this behavior, **Fig. 2.6 (b)** illustrates the calculated axial magnetic force  $F_z$  with respect to  $h$  for  $r_{m,ext} = 110 \text{ mm}$ . The mover is only passively stable in the axial direction at the levitation height  $h_1$  since the axial force increases at lower  $h < h_1$  ( $F_z > F_g$ ) and, therefore, would lift the mover again. The axial stability at  $h_1$  is also indicated by the negative force gradient  $dF_z/dz_m$  around this operating point, whereas around  $h_2$ , the force gradient is positive (unstable). With the above considerations, the mover's radius is chosen to be  $r_{m,ext} = 63 \text{ mm}$  for the design example, meaning that the levitation height is maximized for the stability type ( $F_z, T_{xy}$ ) (see **Fig. 2.6 (a)**).

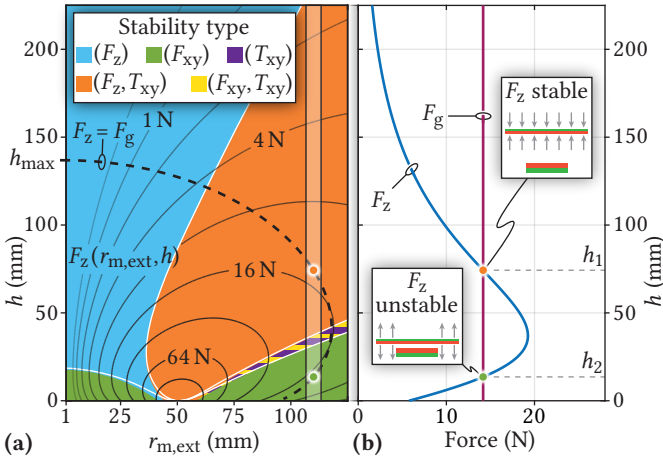


**Fig. 2.6:** (a) Stability regions for different levitation heights  $h$  depending on the mover's radius  $r_{m,ext}$  for two radially centered disc-shaped PMs with  $r_{s,ext} = 50 \text{ mm}$ ,  $h_m = 5 \text{ mm}$ , and  $h_s = 10 \text{ mm}$ . Two stability types are observed in the striped yellow and violet region, depending on whether the mover's angles ( $\theta_{m,x}$  and  $\theta_{m,y}$ ) are actively controlled. (b) Axial magnetic force versus axial position of the mover with  $r_{m,ext} = 110 \text{ mm}$ , where the levitation positions for  $F_z = F_g$  are highlighted. The gradient of  $F_z$  reveals that the passive levitation is axially stable at  $h_1$ , whereas it is unstable at  $h_2$ .

For completeness, it should be mentioned that the other regions where three DOFs must be regulated actively, i.e., where the stability types  $(F_{xy}, T_{xy})$ ,  $(F_{xy})$ , and  $(T_{xy})$  are found, are relatively narrow and are characterized by lower levitation heights compared to the stability type  $(F_z, T_{xy})$ . Therefore, only MLPs exhibiting the stability type  $(F_z, T_{xy})$  are pursued and investigated further in this thesis.

### 2.4.2 From Disc-Shaped to Ring-Shaped PMs

A further possibility to increase the levitation height  $h$  is reducing the mover's weight and, therefore, the gravitational force  $F_g$  by increasing the mover's internal radius  $r_{m,int}$ , i.e., by passing from a disc-shaped to a ring-shaped mover PM. At the same time, a decrease of the axial force  $F_z$  is expected since the needed additional model coil placed at the mover's internal radius (**Fig. 2.1**) generates an attractive force in combination with the stator coil due to its opposite current direction, compared to the external mover coil. As derived in **Section 2.8** and shown in **Fig. 2.7 (b)**, even though  $F_g$  reduces with the square of  $r_{m,int}$  and the axial force  $F_z$  decays proportionally with  $r_{m,int}$ , the levitation height  $h$  decreases with increasing  $r_{m,int}$  (see **Fig. 2.7 (c)**). This levitation height reduction occurs because  $F_z$  is always lower than  $F_g$ , as highlighted in **Fig. 2.7 (b)**. However, the major advantage of a ring-shaped mover compared to a disc-shaped mover ( $r_{m,int} = 0$  mm) is the substantial increase of the rotational stiffness (magnitude of the torque gradient) with increasing  $r_{m,int}$  (up to  $r_{m,int} = 46$  mm as illustrated in **Fig. 2.7 (d)**). Assuming a minimum required rotational stiffness of  $1 \text{ mNm}/^\circ$ , an optimum mover's internal radius of  $r_{m,int} = 26$  mm is found. This 35 times larger stiffness compared to the disc-shaped mover PM comes at the expense of a levitation height reduction of only 3 mm, i.e., a decrease of 2.5 % (cf. **Fig. 2.7 (a)** and **(c)**).

The same sensitivity analysis is conducted for the stator's internal radius  $r_{s,int}$ , while a disc-shaped mover with  $r_{m,ext} = 63$  mm is assumed. For the ring-shaped stator, an additional model coil with opposite current direction has to be considered, which reduces the axial force  $F_z$ . Since the mover's dimensions are kept constant,  $F_g$  of the mover remains constant. Consequently, the levitation height decreases with increasing  $r_{s,int}$  as shown in **Fig. 2.8 (a)**. As already observed for the variation of  $r_{m,int}$ , the rotational stiffness increases for a ring-shaped stator (see **Fig. 2.8 (b)**). However, to reach the same stiffness as with a ring-shaped mover, the levitation height drops substantially by 34 mm, i.e., 28 % compared to a disc-shaped stator.

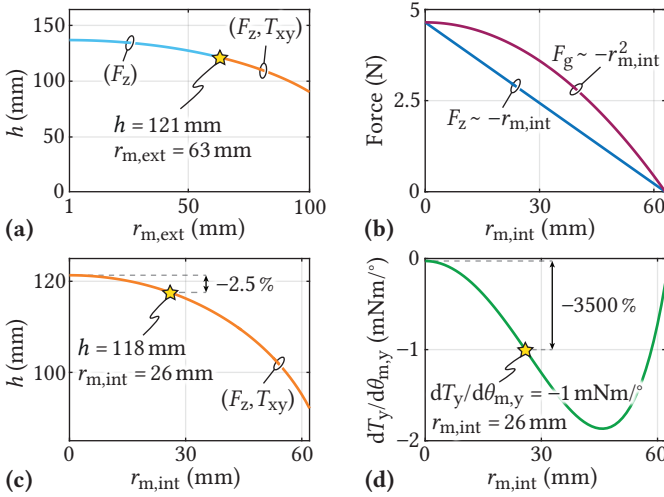


**Fig. 2.7:** MLP design example starting from two disc-shaped PMs with fixed dimensions  $r_{s,ext} = 50$  mm,  $r_{s,int} = 0$  mm,  $h_s = 10$  mm, and  $h_m = 5$  mm. **(a)** Levitation height versus mover's external radius with  $r_{m,int} = 0$  mm (same as the dashed line in **Fig. 2.6 (a)**). With the optimal radius  $r_{m,ext} = 63$  mm, the largest levitation height for the stability type  $(F_z, T_{xy})$  is obtained. Trends of **(b)** the axial and gravitational forces, **(c)** the levitation height  $h$ , and **(d)** the rotational stiffness with respect to the mover's internal radius  $r_{m,int}$ .  $r_{m,int}$  is selected to be 26 mm such that a rotational stiffness of 1 mNm/° is ensured and the levitation height reduction is small.

Besides changing the inner and outer radii of the PMs, their heights  $h_s$  and  $h_m$  are varied. Starting with the variation of the stator's height  $h_s$ , while keeping the other PM dimensions constant ( $r_{s,ext} = 50$  mm,  $r_{s,int} = r_{m,int} = 0$  mm,  $r_{m,ext} = 63$  mm, and  $h_m = 5$  mm), it is expected (and mathematically derived in **Section 2.8**) that the axial force increases linearly with  $h_s$ . Based on (2.1), the equivalent coil current and, thus, the Lorentz force increase linearly. This means that the levitation height  $h$  increases as the gravitational force of the mover remains unchanged. However, as already observed in **Fig. 2.6**, the stability type changes depending on the levitation height  $h$ . Consequently, the stator's height must be limited below  $h_s = 10$  mm for the design example to maintain the desired stability type  $(F_z, T_{xy})$  (see **Fig. 2.9 (a)**).

Now, fixing the stator's height to  $h_s = 10$  mm, the mover's height  $h_m$  is varied to address the corresponding stiffness sensitivity. As detailed in **Section 2.8**, all forces and gradients scale linearly with  $h_m$ . The rotational

## 2.4. Dependence of Levitation Properties on MLP Dimensions

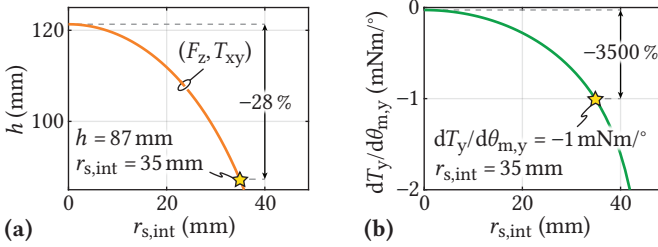


**Fig. 2.8:** MLP design example starting from two disc-shaped PMs with fixed dimensions  $r_{s,ext} = 50$  mm,  $h_s = 10$  mm,  $h_m = 5$  mm,  $r_{m,int} = 0$  mm, and  $r_{m,ext} = 63$  mm. **(a)** Resulting levitation height  $h$  and **(b)** rotational stiffness depending on the stator's internal radius  $r_{s,int}$ . To achieve a rotational stiffness of 1 mNm/° by varying  $r_{s,int}$ , a much stronger levitation height reduction has to be accepted, compared to the case where  $r_{m,int}$  is varied.

stiffness increases as depicted in **Fig. 2.9 (b)** for increasing  $h_m$ . Since  $F_z$  increases and  $F_g$  reduces with the same linear factor dependent on  $h_m$ , the mover's vertical position (indicated by  $z_m$  in **Fig. 2.3**) remains the same, indicating that the effective levitation height  $h = z_m - h_s/2 - h_m/2$  decreases with increasing mover's height. Thus,  $h_m$  can finally be used to tune the stiffnesses, while a slight levitation height reduction has to be accepted.

Concluding this section, the design example showed that the effective levitation height  $h$  cannot be increased by reducing the weight of the mover,

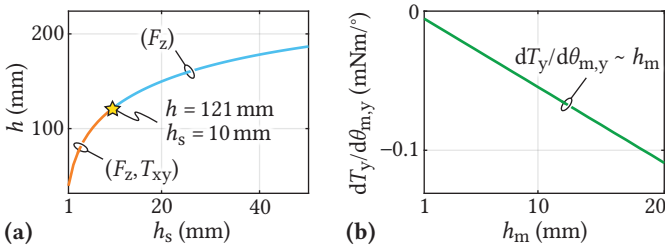


**Fig. 2.9:** MLP design example starting from two disc-shaped PMs with fixed dimensions  $r_{s,ext} = 50$  mm,  $r_{s,int} = r_{m,int} = 0$  mm, and  $r_{m,ext} = 63$  mm. **(a)** Levitation height  $h$  with respect to the stator's height  $h_s$ , where the mover's height is fixed to  $h_m = 5$  mm. An improvement of the levitation height for increasing  $h_s$  is observed but is limited by the stability type region. **(b)** Linear trend of the rotational stiffness versus mover's height  $h_m$ , where the stator's height is  $h_s = 10$  mm.

i.e., by increasing its internal radius  $r_{m,int}$ . However, with a ring-shaped mover, a strongly enhanced rotational stiffness is gained at the expense of a slight levitation height reduction. Similarly, the rotational stiffness increases with a ring-shaped stator, but the levitation height reduction is much more substantial. In contrast, the stator's height  $h_s$  increases the levitation height only up to some extent, determined by the stability type of the levitation point. Finally, the mover's height  $h_m$  linearly tunes the stiffnesses, affecting the levitation height by  $-h_m/2$ .

## 2.5 Optimization Process

In the example above, only one dimension has been varied at a time to analyze the sensitivity of the levitation height on different design parameters and to determine the passive stability properties. In the following, an optimization is performed where all mentioned dimensions are varied iteratively, and the resulting characteristics of the levitation points are determined to find the optimal MLP arrangement for the given application requirements.

### 2.5.1 Optimization Targets

In the design process, the resulting levitation height  $h$  is determined for a given geometry, where the mover is assumed to be radially centered and  $F_z = F_g$  (see  $LP_1$  and  $LP_2$  in **Fig. 2.10 (a)**). Afterwards, the gradients of three mover's DOFs, i.e.,  $dF_x/dx_m$ ,  $dF_z/dz_m$ , and  $dT_y/d\theta_{m,y}$ , at these levitation heights are calculated, such that the stiffnesses and the stability properties are obtained. Due to the axial symmetry of the MLP, the remaining gradients are evaluated with (2.10)-(2.12). For the optimization process, only designs with the stability type  $(F_z, T_{xy})$  are considered ( $LP_1$  in **Fig. 2.10 (a)**), whereas designs with other stability types are discarded ( $LP_2$  in **Fig. 2.10 (a)**). A further essential aspect is the achievable robustness, which measures the magnitude of the external disturbance or the maximum displacement/rotation that the mover can withstand, maintaining the same stability properties as in the original levitation point, and is divided into three categories.

The *axial robustness* is defined as the maximum axial force  $F_{z,max}$  that can be applied to the mover, i.e., the maximum payload capability (**Fig. 2.10 (a)**). For example, the mover levitating at  $LP_1$  can be loaded with an additional payload. Consequently, the levitation height reduces until the minimum levitation height  $h_{min}$  is achieved for the maximum payload. The stability properties change for levitation heights below  $h_{min}$ , meaning that the active

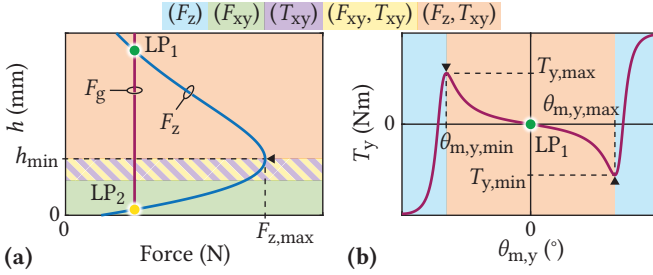


**Fig. 2.10:** (a) Illustration of the axial robustness where the mover exhibits the stability type  $(F_z, T_{xy})$  at  $LP_1$ . The mover can be loaded with an additional payload up to  $F_{z,\max}$  before the stability properties of the original levitation point are violated. (b) Illustration of the rotational robustness for the levitation point  $LP_1$  of (a). When the maximum torque  $T_{y,\max}$  is exceeded, the torque gradient becomes positive, i.e., the mover loses its ability to reject external torque disturbances.

control has to be changed.

The *rotational robustness* is defined as the maximum torque in the  $x, y$  directions that the mover can withstand such that the same stability type as in the horizontal position is maintained (Fig. 2.10 (b)). Rotations with angles larger than  $\theta_{m,y,\max}$  cause the mover to lose its ability to stabilize rotational disturbances. The shown torque curve versus the rotation angle is an odd function since the mover is radially centered; therefore, it holds  $\theta_{m,y,\min} = -\theta_{m,y,\max}$  and  $T_{y,\min} = -T_{y,\max}$ .

The *radial robustness* is related to the maximum displacement  $x_{m,\max}$  of the mover from the radially centered position in the  $x$  direction until the mover loses its initial stability properties, obtained at the levitation point with  $x_m = 0$  (Fig. 2.11). The initial levitation position is indicated with  $LP_1$ , where the mover exhibits the stability type  $(F_z, T_{xy})$ , it levitates horizontally ( $\theta_{m,x} = \theta_{m,y} = 0$ ), and it is radially centered ( $x_m = y_m = 0$ ). For each investigated position ( $x_m > 0$ ), the new axial force and torque equilibrium must be found, in which the mover still exhibits the stability type  $(F_z, T_{xy})$ . The equilibrium is found in two steps: the angle  $\theta_{m,y}$  has to be determined such that the  $y$  torque becomes zero ( $T_y(x_m, \theta_{m,y}) = 0$ ), while the new levitation height is found with  $F_z(x_m, \theta_{m,y}) = F_g$ . Hence, compared to the axial and rotational robustness, the computational effort is larger due to the iterative computation to find the equilibrium for each position  $x_m$ . It should be mentioned that for  $(F_z, T_{xy})$  stable MLPs, it is essential to have a wide range of radial robustness since this allows the mover to deviate from its nominal radially centered



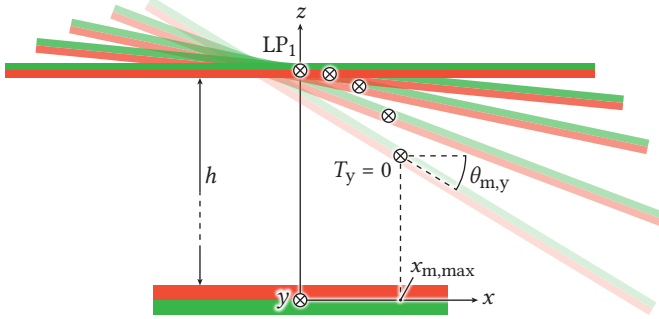


**Fig. 2.11:** Cross-section view of the passive MLP with the mover initially positioned at the levitation point  $LP_1$  of **Fig. 2.10 (a)** and subjected to a radial displacement in the  $x$  direction to determine the radial robustness. For each position  $x_m$ , the angle  $\theta_{m,y}$  has to be determined such that  $T_y = 0$  and  $F_z = F_g$ . For  $x_m > x_{m,max}$ , the mover loses a stable component of the initial stability type ( $F_z, T_{xy}$ ).

position, and gives the sensor and the position controller enough headroom to sense a position change and bring the mover back to its original levitation position.

### 2.5.2 Multi-Objective Optimization

As mentioned, the proposed geometry optimization is conducted by varying the dimensions of the PMs and calculating their levitation points, stability properties, and robustnesses. The relative magnetization direction between the stator and the mover gives additional freedom. For two disc-shaped PMs, a repulsive force is only obtained for PMs having opposite polarities. However, when at least one PM is realized as a ring-shaped PM, both relative magnetization directions can result in a repelling axial force depending on the PMs' dimensions. Therefore, in the optimization process seven design parameters could be iterated:  $r_{s,int}$ ,  $r_{s,ext}$ ,  $h_s$ ,  $r_{m,int}$ ,  $r_{m,ext}$ ,  $h_m$ , and the relative magnetization direction. In the following, the stator's external radius is fixed to  $r_{s,ext} = 50$  mm to reduce the computational effort. As shown in **Section 2.8**, based on the derived scaling laws, the resulting optimum MLP can be scaled to any other stator's external radius in a post-processing step. For the same reason, the mover's height is fixed to  $h_m = 5$  mm since the forces and torques can be scaled linearly with the mover's height  $h_m$  in a post-processing step (see **Section 2.8**). Hence, the optimization is constrained to the remaining

five design parameters:  $r_{s,int}$ ,  $h_s$ ,  $r_{m,int}$ ,  $r_{m,ext}$ , and the relative magnetization direction.

## 2.6 Optimization Results

In **Fig. 2.12 (a)**, the optimization results of all geometries, which result in a stability type ( $F_z$ ,  $T_{xy}$ ) are represented as a 3D Pareto plot, where the characteristic dimension-related levitation height (CDRLH) is evaluated with respect to the relative payload capability  $F_{z,max}/F_g$  and the stable (negative) torque gradient  $dT_y/d\theta_{m,y}$  (same as  $dT_x/d\theta_{m,x}$  due to the axial symmetry). In addition, the color bar highlights the gradient of the unstable (positive)  $x$  force component  $dF_x/dx_m$  (same as  $dF_y/dy_m$ ), which is related to the required magnetomotive

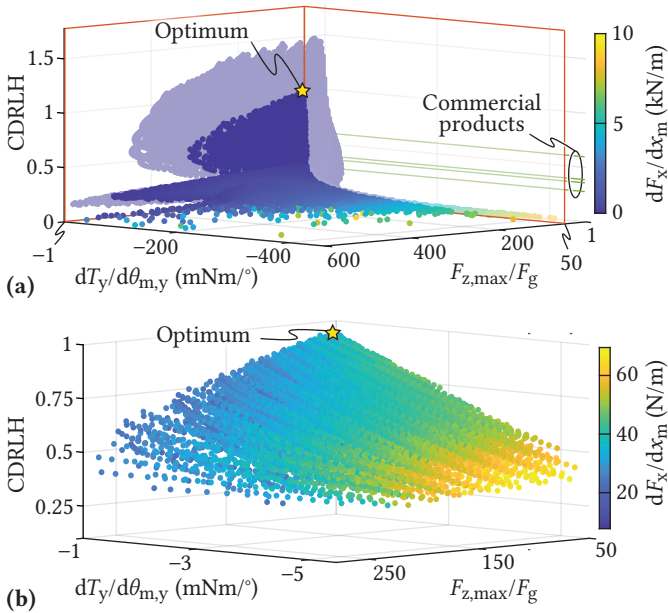


**Fig. 2.12:** Pareto plot of (a) all geometries, which result in the stability type ( $F_z$ ,  $T_{xy}$ ) and (b) remaining designs with minimum relative payload capability of  $F_{z,max}/F_g = 50$  and minimum rotational stiffness  $|dT_y/d\theta_{m,y}| = 1$  mNm/°. The color bar corresponds to the gradient of the unstable radial force component  $dF_x/dx_m$ , which has to be compensated by the magnetomotive force (MMF) of the EMs.

force (MMF) generated by the EMs, i.e., the amount of current fed to the EMs to control the mover's radial position actively. It should be mentioned that the radial robustness is not considered in the Pareto plot; however, it is calculated for a set of optimal design candidates in a post-processing stage.

**Fig. 2.12** shows that larger CDRLHs result in lower relative payload capability and radial/rotational stiffnesses since the magnetic flux density strength and, consequently, the forces decrease. A maximum CDRLH around 1.5 would be possible; however, in these cases, the axial/rotational stiffness and robustness approach zero, which is unacceptable for an actual MLP design. Therefore, the optimization results are restricted to a range with a minimum relative payload capability  $F_{z,\max}/F_g = 50$  and a minimum rotational stiffness  $|dT_y/d\theta_{m,y}| = 1 \text{ mNm}/^\circ$ . The Pareto plot of the remaining design points is shown in **Fig. 2.12 (b)**. There, designs with considerable gradients  $dF_x/dx_m$  are discarded since a low MMF is desired for the subsequent EM design (the

**Tab. 2.1:** Optimal MLP dimensions and calculated performance characteristics of the optimal geometry highlighted in **Fig. 2.12** for single or multi-turn model coils.

Mover	Value	Stator	Value
$r_{m,\text{ext}}$	65 mm	$r_{s,\text{ext}}$	50 mm
$r_{m,\text{int}}$	36 mm	$r_{s,\text{int}}$	28 mm
$h_m$	5 mm	$h_s$	21 mm
Weight $m_m$	0.35 kg	Weight $m_s$	0.86 kg
Mag. direction	Down	Mag. direction	Up

Parameter	$N_s = N_m = 1$	$N_s = N_m = 10$
$h$	123.2 mm	123.8 mm
CDRLH	0.948	0.952
$dF_x/dx_m$	33.6 N/m	33.7 N/m
$dF_z/dz_m$	-65.8 N/m	-66.0 N/m
$dT_y/d\theta_{m,y}$	-1 mNm/ $^\circ$	-1 mNm/ $^\circ$
$T_{y,\text{max}}$	13.4 mNm	13.7 mNm
$\theta_{m,y,\text{max}}$	18 $^\circ$	18 $^\circ$
$x_{m,\text{max}}$	16 mm	16 mm
$F_{z,\text{max}}/F_g$	55.8	50.7
Payload capability	19.1 kg	17.4 kg

color scale shows N/m instead of kN/m shown in **Fig. 2.12 (a)**). With the mentioned constraints, a high CDRLH around 0.95 is still achievable, which is outperforming existing commercial products with CDRLHs around 0.6 [7]. Moreover, a ten times higher payload capability is obtained.

**Tab. 2.1** presents the mover's and stator's dimensions of the optimal design highlighted in **Fig. 2.12** and the corresponding performance characteristics, where similar results are obtained for the single and multi-turn coil approach. The optimum mover's external radius  $r_{m,ext}$  is larger than the stator's external radius  $r_{s,ext}$ ; thus, it defines the characteristic dimension of the passive MLP to  $2 \cdot r_{m,ext} = 130$  mm. The levitation height is  $h = 123.8$  mm, the mover can be rotated up to  $18^\circ$  around the radial axes, and a maximum radial displacement of 16 mm is allowed until the mover becomes unstable. Furthermore, the mover can carry a maximum payload of 17.4 kg, significantly reducing the passive levitation height.

## 2.7 Experimental Verification

A test setup to measure the forces and torques acting on the mover is built to validate the analytical model, as illustrated in **Fig. 2.13**. In the test setup, the stator can be precisely moved against the fixed mover in the  $x$  and  $z$  directions using a positioning stage, and a 6 DOF sensor records all forces and torques applied to the mover. In contrast, the mover freely levitates above the fixed stator in the final MLP setup.

In the test setup, both PMs with the dimensions listed in **Tab. 2.2** are realized with many small rectangular PMs stacked together in a 3D-printed housing, achieving an approximation of the optimal PMs dimensions dis-

**Tab. 2.2:** Dimensions of the PMs used for the experimental verification of the analytical model.

Mover	Value	Stator	Value
$r_{m,ext}$	64.6 mm	$r_{s,ext}$	50 mm
$r_{m,int}$	35.9 mm	$r_{s,int}$	26.5 mm
$h_m$	5 mm	$h_s$	20 mm
Weight $m_m$	0.43 kg	Weight $m_s$	0.91 kg
Mag. direction	Down	Mag. direction	Up

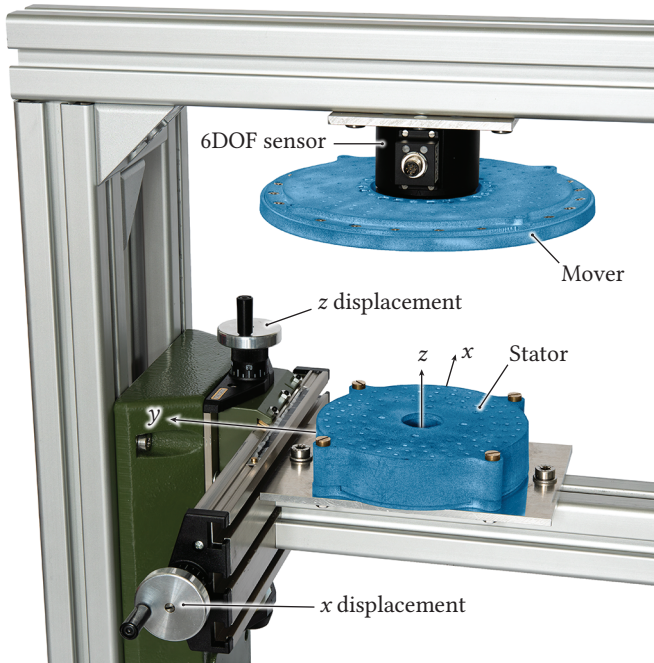


**Fig. 2.13:** Test setup showing the essential components, where the stator can be precisely moved against the fixed mover in the  $x$  and  $z$  directions with a positioning stage. The mover is mounted to a 6 DOF sensor (Rokubi of BOTA Systems), which records all forces and torques applied to the mover with a resolution of 0.15 N and 5 mNm, respectively. Stator and mover are realized with a 3D-printed housing where many small PMs (quality N45) are inserted.

played in **Tab. 2.1**. Due to the free space between the individual rectangular PMs, the magnetic volume of the stator and mover PM is reduced (see **Fig. 2.14 (a)**), meaning that lower forces and torques are obtained. The PM volume reduction corresponds to a proportional decrease of magnetic dipoles in a given stator's and mover's volume; thus, based on Ampère's law given in (2.1), it results in an equivalent reduction of the stator's and mover's coercive field strength  $H_{ci,s}$  and  $H_{ci,m}$ , assuming a constant stator's and mover's volume. The reduction factors are determined from the volume ratio of the discrete PMs and the originally calculated ring-shaped PM volume, and they result in 78 % and 74 % for the built stator and mover, respectively. The magnetic

force scales with  $H_{ci,s} \cdot H_{ci,m}$  and, therefore, reduces to 58 % with respect to the optimal ring-shaped PMs. Since the gravitational force of the mover does not scale with the same factor as the magnetic force – it scales proportionally with the mover’s volume – the scaling laws derived in **Section 2.8** cannot be applied, meaning that the new MLP characteristics have to be recalculated by using the reduced  $H_{ci,s}$  and  $H_{ci,m}$  in the analytical model. Therefore, the performance characteristics listed in **Tab. 2.1** differ from those presented in the following due to the PMs volume reduction.

The corresponding calculated and measured axial forces with respect to the distance  $h$  are shown in **Fig. 2.14 (c)** for a radially centered mover ( $x_m = y_m = 0$ ). The axial force monotonically increases with reduced height  $h$ , indicating that all levitation heights are at least ( $F_z$ ) stable depending on the additional payload. The axial force derived with the multi-turn model always lies between the forces calculated with the single and double-turn model. For the given setup, the calculation error between the single and multi-turn model is below 6 %, as shown in **Fig. 2.14 (d)**, also at low distances  $h$ . Furthermore, all models provide a good correspondence with the performed measurements.

Even though the mover is not actively levitated in the test setup yet, the levitation point is found by comparing the axial force with the mover’s gravitational force and results in  $h = 88$  mm. The total mover’s weight is  $m_m = 0.43$  kg considering the set of small PMs, the 3D-printed housing, and the screws for the assembly. The axial force gradient at the levitation point is obtained as  $dF_z/dz_m = -94$  N/m. The axial force measurement also determines the maximum payload capability of 6.3 kg at the minimum achievable levitation height of  $h = 12$  mm, which is limited by the 3D-printed housing’s thicknesses of the stator and mover ( $h$  is intended as the distance between the PMs’ surfaces to be consistent with the definition used in this thesis).

At the levitation point  $h = 88$  mm, the realized MLP with radially centered mover is also characterized concerning its rotational stiffness and robustness, where the torque  $T_y$  is calculated and measured for different rotation angles  $\theta_{m,y}$  as depicted in **Fig. 2.14 (b)**. The results obtained with the single and multi-turn models agree with the experimental measurements. However, at large angles, a small difference is noted due to the limited accuracy of the setup regarding angular adjustments. Therefore, additional FEM simulations have been performed to verify the results of the analytical model. Furthermore, the maximum rotation angle before the system without payload becomes unstable, i.e., the gradient becomes positive, is determined as  $\theta_{m,y,max} = 27^\circ$  where a maximum stabilizing torque of  $|T_{y,min}| = 72.8$  mNm is achieved. The rotational stiffness is found with the torque gradient at  $\theta_{m,y} \rightarrow 0$ , which

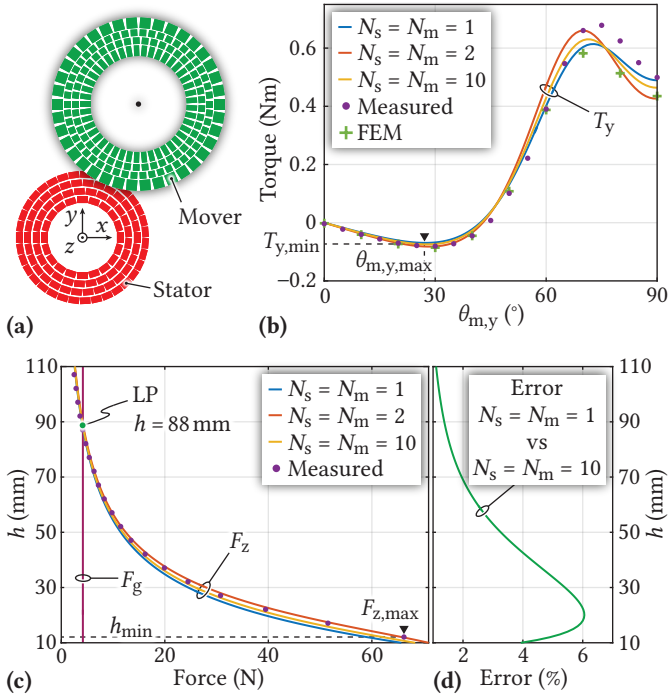


**Fig. 2.14:** (a) Top view of the PMs' schematic realization of Fig. 2.13, where discrete magnets instead of ring-shaped PMs are utilized. (b) Comparison of the calculated and measured torque for a rotated but radially centered mover at the levitation height  $h = 88$  mm, where the rotational stiffness and robustness are verified. (c) Comparison of the calculated and measured axial force on the mover (radially centered) that is displaced in the axial direction to determine the levitation point (LP) and the maximum payload capability. (d) Calculation error between the single and multi-turn models.

leads to  $|dT_y/d\theta_{m,y}| = 2.5 \text{ mNm}/^\circ$ . Therefore, the performed measurements show that the designed MLP achieves the stability type  $(F_z, T_{xy})$  for the shown levitation point. Moreover, the same stability type has been observed by performing simulations for levitation heights (i.e., larger payloads) down to  $h = 12$  mm, and radial displacements up to  $x_{m,max} = 44$  mm, starting from the levitation point  $h = 88$  mm.

## 2.8 Scaling Laws

With the performed Pareto optimization in **Section 2.6**, the optimal dimensions of the PMs were found, which for the defined design space resulted in a calculated maximum levitation height of 123.8 mm and payload capability of 17.4 kg. Assuming that the demanded specifications would change, e.g., concerning the desired maximum levitation height or the payload, one would not repeat the complete optimization routine. Instead, the scaling laws derived in this section could be used to determine the new PM dimensions, such that the new requirements concerning levitation height, forces, torques, or stiffnesses are met.

### 2.8.1 Proportionality Factors

For the derivation of the scaling laws, proportionality factors ( $\lambda_1$  and  $\lambda_2$ ) between different design variables (stator's radius  $r_s$ , mover's radius  $r_m$ , and levitation coordinate  $z_m$ , i.e., the vertical distance between the stator's and mover's center of mass) are introduced such that the resulting flux density, forces, and torques are expressed with a reduced number of variables

$$r_m = \lambda_1 r_s \quad (2.15)$$

$$z_m = \lambda_2 r_s \quad (2.16)$$

$$|\mathbf{r}| \propto r_s. \quad (2.17)$$

Furthermore, the equivalent Ampèrian current of a PM, given in (2.1), is directly proportional to the height of the corresponding PM

$$I_i \propto h_i \quad \text{with } i = \{s, m\}. \quad (2.18)$$

Accordingly, the magnetic flux density  $|\mathbf{B}|$ , derived in (2.4), is related to the defined quantities as

$$|\mathbf{B}| \propto \frac{I_s \cdot r_s \cdot r_s}{r_s^3} \propto \frac{h_s}{r_s}, \quad (2.19)$$

which means that the magnetic flux density is directly proportional to the stator's height and inversely proportional to the stator's radius.

Furthermore, from (2.5) and (2.19), it follows that the force  $|\mathbf{F}_{\text{tot}}|$  is directly proportional to the height of both PMs and to the proportionality constant  $\lambda_1$

$$|\mathbf{F}_{\text{tot}}| \propto \frac{I_m \cdot r_m \cdot h_s}{r_s} \propto h_m h_s \lambda_1, \quad (2.20)$$



meaning that the ratio between the PM radii impacts the force magnitude.

The torque  $|\mathbf{T}_{\text{tot}}|$  is characterized by combining (2.6) and (2.20) as

$$|\mathbf{T}_{\text{tot}}| \propto r_m h_m h_s \lambda_1 = h_m h_s r_s \lambda_1^2. \quad (2.21)$$

Finally, the mover's gravitational force  $F_g$ , which is of fundamental importance to determine the levitation height  $h$ , is determined as

$$F_g \propto h_m r_m^2 = h_m r_s^2 \lambda_1^2, \quad (2.22)$$

which is proportional to the volume of the mover.

### 2.8.2 Scaling Laws

The dimensions of the already characterized MLP can be scaled based on the derived proportionalities between forces, torques, and MLP size. It is assumed that the original mover's radius  $r_m$  and stator's radius  $r_s$  are scaled by the same factor  $a_1$  to the new mover's radius  $r_m^*$  and stator's radius  $r_s^*$  as

$$r_m^* = a_1 r_m \quad (2.23)$$

$$r_s^* = a_1 r_s. \quad (2.24)$$

In the general case, where the PMs are ring-shaped magnets, mover's and stator's radii must be scaled by the same factor  $a_1$ . The scaling of the PM heights  $h_m$  and  $h_s$  are found under the condition that the axial force, given by  $|\mathbf{F}_{\text{tot}}|$ , scales with the same factor as the gravitational force  $F_g$ . Hence, the original stator's height  $h_s$  scales with  $a_1^2$ , whereas for the original mover's height  $h_m$ , an arbitrary scaling factor  $a_2$  is selected

$$h_s^* = a_1^2 h_s \quad (2.25)$$

$$h_m^* = a_2 h_m. \quad (2.26)$$

Consequently, applying the scaling factors  $a_1$  and  $a_2$  to the force and torque equations given in (2.20), (2.21), and (2.22), it follows for the new forces  $|\mathbf{F}_{\text{tot}}|^*$ ,  $F_g^*$  and torque  $|\mathbf{T}_{\text{tot}}|^*$

$$|\mathbf{F}_{\text{tot}}|^* = a_1^2 a_2 |\mathbf{F}_{\text{tot}}| \quad (2.27)$$

$$|\mathbf{T}_{\text{tot}}|^* = a_1^3 a_2 |\mathbf{T}_{\text{tot}}| \quad (2.28)$$

$$F_g^* = a_1^2 a_2 F_g. \quad (2.29)$$

Both force equations scale with the same factor  $a_1^2 a_2$ , whereas the torque scales with  $a_1^3 a_2$ . Furthermore, based on (2.16), the original levitation coordinate  $z_m$  scales as

$$z_m^* = a_1 z_m. \quad (2.30)$$

Thus, the new levitation height  $h^*$  is found as

$$h^* = z_m^* - \frac{h_s^*}{2} - \frac{h_m^*}{2} = a_1 z_m - \frac{a_1^2 h_s}{2} - \frac{a_2 h_m}{2}. \quad (2.31)$$

Finally, the force and torque gradients are obtained by deriving (2.27) and (2.28) for a small displacement or rotation as

$$\text{grad}(F)^* = a_1 a_2 \cdot \text{grad}(F) \quad (2.32)$$

$$\text{grad}(T)^* = a_1^3 a_2 \cdot \text{grad}(T). \quad (2.33)$$

For completeness, the mover's and stator's weight scale as

$$m_m^* = a_1^2 a_2 m_m \quad (2.34)$$

$$m_s^* = a_1^4 m_s. \quad (2.35)$$

$$(2.36)$$

As a simple and useful conclusion of the scaling laws, it is stated that if only the mover's height  $h_m$  is scaled with the factor  $a_2$ , all forces, torques, and corresponding gradients scale linearly with  $a_2$ , whereas the levitation coordinate  $z_m$  remains the same since it only depends on the factor  $a_1$ . Further, if  $a_1$  is increased, the forces and torques scale with  $a_1^2$  and  $a_1^3$ , respectively.

### 2.8.3 Example

To demonstrate the effectiveness of the scaling laws, the optimized MLP designed in **Section 2.6** should be scaled to a new MLP, which achieves a maximum levitation height of  $h = 150$  mm and features a payload capability of 50 kg. Based on (2.31) and (2.29), the two scaling factors are directly found as  $a_1 = 1.25$  and  $a_2 = 1.84$ . **Tab. 2.3** shows the dimensions and performance characteristics of the scaled MLP.

**Tab. 2.3:** Dimensions and performance characteristics of the scaled optimal geometry of **Tab. 2.1** obtained applying the scaling laws for the case  $N_s = N_m = 10$ . The correctness of the values has been verified with simulations.

Mover	Value	Stator	Value
$r_{m,ext}^*$	81.3 mm	$r_{s,ext}^*$	62.5 mm
$r_{m,int}^*$	45 mm	$r_{s,int}^*$	35 mm
$h_m^*$	9.2 mm	$h_s^*$	32.8 mm
Weight $m_m^*$	1 kg	Weight $m_s^*$	2.1 kg
Mag. direction	Down	Mag. direction	Up
Parameter	Value	Factor	Value
$h^*$	150 mm	$a_1$	1.25
CDRLH*	0.923		
$(dF_x/dx_m)^*$	77.6 N/m	$a_1 a_2$	2.3
$(dF_z/dz_m)^*$	-151.9 N/m	$a_1 a_2$	2.3
$(dT_y/d\theta_{m,y})^*$	-3.6 mNm/°	$a_1^3 a_2$	3.6
$T_{y,max}^*$	48.2 mNm	$a_1^3 a_2$	3.6
$\theta_{m,y,max}^*$	18°		
$x_{m,max}^*$	20 mm	$a_1$	1.25
$F_{z,max}^*/F_g^*$	55.8		
Payload capability*	50 kg		

## 2.9 Conclusions

This chapter presents a simple analytical method to calculate the 3D magnetic forces and torques between permanent magnets (PMs). The PMs are first substituted by model coils based on the Ampèrian model, and with a discretization of the Biot-Savart law, the 3D field is calculated. This model allows the calculation of all forces and torques of any arbitrary geometry based on the Lorentz law. Furthermore, stiffnesses in all six degrees of freedom (DOFs) are determined with the displacement method.

Taking an axially symmetric magnetic levitation platform (MLP) as an example, it is shown that depending on the selected MLP dimensions, different stability types are obtained, and ring-shaped PMs outperform disc-shaped PMs concerning achievable stiffnesses by several orders of magnitude; however, lead to a slightly reduced axial levitation height. With the performed Pareto optimization, it is shown that a characteristic dimension-related levitation height (CDRLH) of around 1.5 can be achieved. However, if a minimum payload capability of 50 times the mover's weight and rotational stiffness of  $dT_y/d\theta_{m,y} = 1 \text{ mNm}/^\circ$  are considered, the maximum CDRLH reduces to around 1, which is still almost a factor of two higher as obtained with commercially available products, even with a more stringent constraint on the payload capability.

Furthermore, the forces calculated with the proposed analytical approach are verified on a 6 DOF test setup, which reveals a good matching between calculations and experimental results independent of the chosen number of model windings.

As a final consideration, one can extend the proposed analytical 3D model to calculate the forces between electromagnets (EMs) and PMs and to any ironless MLP (e.g., with radially arranged PMs or systems featuring Halbach arrays) since in the magnetic flux density and force calculation process, no assumptions on the shape or any symmetries are made. As long as one can substitute the PMs and EMs in the system with current-carrying coils arranged such that their magnetic flux density distribution is replicated, the presented discretization and summation process for calculating the magnetic forces can be conducted. With further investigation, the forces in simple MLPs employing iron core structures could be calculated with the method of images. However, in this case, one has to consider the effort for building the model, its time performance, and precision compared to the commonly used FEM simulations.

# 3

## Reaction Force-Based Position Sensing for Magnetic Levitation Platform with Exceptionally Large Hovering Distance

This chapter summarizes the most relevant findings of the investigation of magnetic levitation platforms regarding their dynamic behavior and the employment of a reaction force sensor for their closed-loop control that are also published in:

- ▶ R. Bonetti, L. Beglinger, S. Mirić, D. Bortis, and J. W. Kolar, “Reaction Force-Based Position Sensing for Magnetic Levitation Platform with Exceptionally Large Hovering Distance,” *Actuators*, vol. 13(3), no. 114, pp. 1-31, March 2024.

### Chapter Abstract

This chapter introduces a novel sensing concept based on reaction forces for determining the position of the levitating magnet (mover) for magnetic levitation platforms (MLPs). Besides being effective in conventional magnetic bearings, the applied approach enables the operation in systems where the mover is completely isolated from the actuating electromagnets (EMs) of the stator (e.g., located inside a sealed process chamber) while levitating at an extreme levitation height. To achieve active position control of the levitating mover by properly controlling the stator EM currents, it is necessary to employ a dynamic model of the complete MLP, including the reaction force sensor, and implement an observer that extracts the position from the force-dependent signals, given that the position is not directly tied to the measured forces. Furthermore, two possible controller implementations are discussed in detail: a basic PID-controller and a more sophisticated state-space controller that can be chosen depending on the characteristics of the MLP and the accuracy of the employed sensing method. To show the effectiveness of the proposed position sensing and control concept, a hardware demonstrator employing a 207 mm outer diameter (characteristic dimension, CD) stator with permanent magnets, a set of electromagnets, and a commercial multi-axis force sensor is built, where a 0.36 kg mover is stably levitated at an extreme air gap of 104 mm.

## 3.1 Introduction

In the literature, various types of Magnetic Levitation Platforms (MLPs) are investigated, which can be divided into two groups: (1) systems where the distance  $h$  between stator and mover (i.e., the levitation height) is much smaller than the characteristic dimension of the system (i.e., the largest dimension CD of the system in **Fig. 3.1**), and (2) systems where the levitation height is comparable to the characteristic dimension.

The first type of MLPs features a very small air gap and is generally used in industry for fast and precise motion with different degrees of freedom (DOFs) [37–41], such as pick-and-place machines, wafer scanners, electron microscope inspection systems [42], vibration isolation systems [43], in-line surface inspections [44], surface morphology measurements [45], and photolithography in semiconductor manufacturing [46]. Depending on the application, the mover is mainly levitated over the stator/electromagnets to be easily accessible and eventually loaded or placed under the stator to facilitate the intended task. A precise position measurement system for these MLPs with a smaller air gap is required to enable a precisely controlled motion and vibration compensation of all DOFs. Therefore, laser, inductive, or capacitive sensors are mostly employed, detecting displacements of the mover with an

accuracy down to the nanometer scale [47].

The second type of MLPs features a large air gap [6–8, 48–51] and is applied, for example, in wind tunnels where large distances between the object under test (or mover) and the surrounding levitating system are required. The largest structure of this kind offers a cylindrical space with a diameter of 1 m [52], where the levitated object under test is equipped with permanent magnets on the inside, and electromagnets (EMs) are placed around it, enabling a contactless magnetic suspension and balance with the help of optical sensors for the position control [53]. Accordingly, any other mechanical structure that would be needed to hold the object under test in place can be

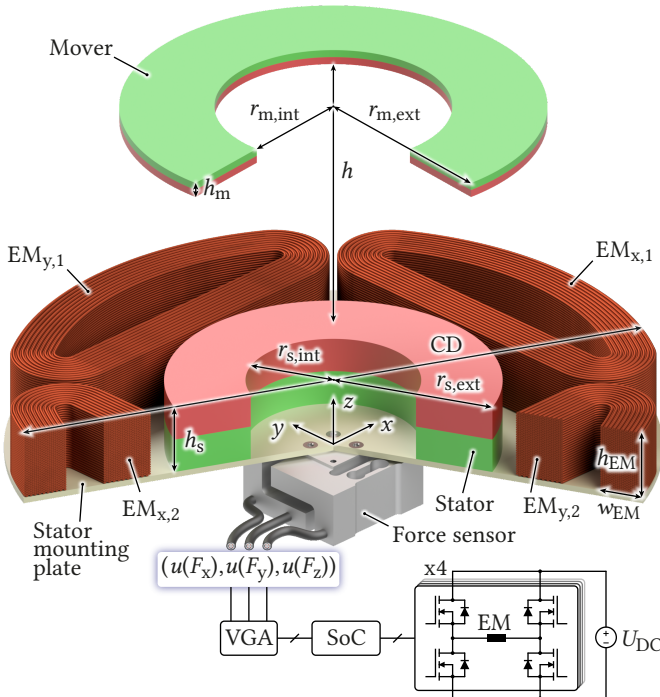


**Fig. 3.1:** 3D rendering of the magnetic levitation platform (MLP) considered in this thesis with a reaction force sensor used to determine the mover's  $x$ ,  $y$  position, actively controlled with the help of electromagnets (EMs), which are driven with a power converter that is controlled with a system-on-a-chip (SoC) where an observer-based position controller (cf. **Section 3.5**) is implemented.

omitted, avoiding changes in the airflow around it. Furthermore, in systems where a lower number of DOFs are actively controlled, on the one hand, the mover is suspended under the stator and/or EMs [54]. The advantage of this configuration is a reduced control effort since only a single unstable DOF (vertical dimension) has to be actively stabilized, which comes at the expense of reduced accessibility for loading the mover. On the other hand, in another type of system, the mover levitates above the stator, offering easy accessibility (see **Fig. 3.1**), but this configuration necessitates active control of at least two DOFs ( $x, y$  position). Various patented methods for position sensing can be found for the latter systems depicted in **Fig. 3.1**. For example, in MLPs with relatively small levitation heights (yet comparable to the characteristic dimension  $CD$ , i.e., stator outer diameter), the mover's position is mostly measured with Hall effect sensors [6]. Another sensing technique consists of stationary sensing coils placed on the stator level that are inductively coupled to a target coil placed on the mover [8]. Also, for large levitation heights, optical sensors are often employed [7].

The studied MLP consists of a passive part with permanent magnets (PMs) and a set of electromagnets (EMs) mounted on the stator. The PMs of the mover and the stator (see **Fig. 3.1**) provide the largest levitation force component by compensating for gravitational forces, whereas the EMs are actively driven to stabilize the levitating mover to a desired position and, typically, steer it in a horizontal and/or vertical direction. The analyzed MLP features an extreme levitation height  $h = 104$  mm relative to the characteristic dimension  $CD = 207$  mm (i.e., the  $CD$ -related levitation height exceeds 0.5). For the position control of the levitating magnet and/or mover, a novel position sensing concept is employed that uses a load cell (i.e., force sensor in **Fig. 3.1**) mounted to the stator to capture the reaction forces on the stator caused by a displacement of the mover. In contrast to optical or inductive sensors, the proposed position sensing method can advantageously also be employed when there are obstacles in the air gap (as long as the mover can freely levitate) or the mover is completely isolated from the rest of the system, e.g., if it is levitated in a separated sealed stainless steel process chamber. A Hall effect sensor is not applicable for such an MLP because of the substantial decay of the magnetic field strength with increasing distance. A significant amplification of the sensed signal would be required for large air gaps to detect a change in magnetic field due to a displacement of the mover. However, high gain is not applicable as it would lead to saturation of the measuring circuit output due to the high magnetic field near the stator PM.

Force sensors are typically used for validating [55] and generating [56]



models for MLPs. However, to date, they are not used for the feedback control of the position in MLPs. Nevertheless, force sensors have already been used for position estimation in other research areas. For example, in robotics, a force/torque sensor placed between the robotic arm and hand is applied to estimate the position of a contact point with an object and monitor the contact state of the hand with the grasped object [57]. Additionally, a single force/torque sensor placed on the base frame of a manipulator is used to estimate the contact force and position at the end effector that interacts with humans and/or other robots [58]. Furthermore, in a micro gripper, the sensed forces on both end effectors are used to determine their position [59]. Lastly, in advanced motion control of vehicles, a Kalman filter is applied to real-time lateral tire force measurements for estimating sideslip and roll angles of a car [60].

For the MLP analyzed in this thesis, the mover is free to rotate around the  $x$ ,  $y$  axes (see **Fig. 3.1**), and the PMs, which provide the levitation force component compensating gravitational forces, are designed so that the axial movement (in  $z$  direction) and the rotation around the  $x$ ,  $y$  axes are passively stable **Chapter 2**. Accordingly, when the mover is placed radially centered with the stator, it naturally settles to a horizontal orientation (parallel with the stator) at a vertical distance  $h$  from the stator without active control. However, a motion in the  $x$ ,  $y$  plane caused by disturbances would be unstable due to radial magnetic forces, which accordingly must be actively compensated using time-varying forces generated by EMs mounted on the stator. For a similar arrangement of magnets, researchers claimed that a single unstable radial DOF of the mover is achievable [51]. However, this implies using two straight and (infinitely) long stator rails placed along one radial axis (e.g., in the direction of the  $y$  axis) to obtain a marginally stable mover motion in the same direction as the orientation of the magnetic rails. As stated in [51], the claimed stability can be achieved with a finite length of the rails, which is approximately four times larger than the achieved levitation height. However, active control of the marginally stable DOF is also required; otherwise, a minimal displacement in the uncontrolled direction caused by external disturbances induces a constant movement towards the ends of the rails that cannot be stopped since there are no counteracting magnetic forces.

MLPs with a similar arrangement of PMs and EMs, as analyzed in this thesis, have only been sporadically and lightly analyzed in the literature. Reference [48] reports the dimensions of a tuned commercially available system, static simulations that show the passively stable and unstable DOFs of the levitating magnet, two generic equations of motion for the forces and torques

in the system, a proportional-derivative control law based on readings coming from two Hall effect probes, and the corresponding results during steady-state levitation and under an external disturbance. A more sophisticated control strategy for the same system as [48] is described in [49]. However, the torque equations describing the rotational motion of the mover around the  $x$ ,  $y$  axes are intentionally omitted. Nevertheless, the controller considers the mover's rotation as a disturbance in the sensor readings. Both cited systems work without complex observer/controller structures, as described in the following, because the rotational stiffness is large enough to compensate for the electromagnet's torque on the mover. This characteristic is generally observed for systems where the levitation height is small compared to the dimensions of the electromagnets **Section 2.6**. However, in systems with extreme levitation heights with relatively low passive stiffnesses, careful attention must be taken in modeling the mover's motion and, therefore, is comprehensively examined in a first step in the following.

The chapter is structured as follows. **Section 3.2** initiates the analysis of the MLP, which is characterized by a large levitation height of  $h = 104$  mm relative to the characteristic dimension  $CD = 207$  mm, and employs EMs for stabilizing the radial position of the mover ( $x$ ,  $y$  direction). The derivation of the MLP's dynamic model is shown in **Section 3.3** using simulations and static measurements. Its validation is conducted in the subsequent chapter (**Section 3.4**) with dynamic measurements, where the mover position is controlled with the help of an optical sensor. A force sensor mounted to the stator plate and ultimately used to stabilize the mover records the reaction forces acting on the stator. The position and rotation of the mover are extracted from the sensed forces by an observer (**Section 3.5**) based on the system's model derived in the previous sections and tuned considering deviations of model and measurements. This finally enables the implementation of a controller for the radial stabilization of the mover with additional active damping of the rotation around the radial  $x$ ,  $y$  axes with the same set of EMs. In **Section 3.6**, the experimental MLP hardware implementation is discussed with short insights into the amplifier for the force sensor and the tuning of the controllers, followed by experimental results about the stable levitation of the mover. **Section 3.7** concludes the chapter.

## 3.2 Magnetic Levitation Platform Overview

The MLP analyzed throughout the thesis consists of two axially symmetric PMs designed following the optimization proposed in **Section 2.5**, which

leads to the dimensions listed in **Tab. 3.1**, where the target is to maximize the levitation height  $h$  under constraints on the number of passively stable

**Tab. 3.1:** Dimensions and characteristics of the MLP considered in this thesis. The characteristic CD dimension is defined as the largest dimension of the components in the MLP, in this case, the width of the stator with the EMs, i.e., the diameter of the stator mounting plate (see **Fig. 3.1**).

Mover PM external radius	$r_{m,ext}$	64.6 mm
Mover PM internal radius	$r_{m,int}$	35.9 mm
Mover height	$h_m$	5 mm
Stator PM external radius	$r_{s,ext}$	50 mm
Stator PM internal radius	$r_{s,int}$	26.5 mm
Stator height	$h_s$	20 mm
Mover weight	$m_m$	0.36 kg
Stator weight	$m_s$	0.91 kg
Mover moment of inertia	$J_m$	0.58 gm <sup>2</sup>
Total MLP weight	$m_{mlp}$	3.6 kg
Levitation height	$h$	104 mm
Characteristic dimension	CD	207 mm
Radial stiffness	$k_{FPM}$	32.8 N/m
Displacement torque const.	$k_{Tdisp}$	0.25 Nm/m
Rotational stiffness	$k_{TPM}$	1.6 mNm/°
Rotational damping	$k_{d,rot}$	2 μNms/°
Rotational force const.	$k_{Frot}$	4.4 mN/°
EMs force const.	$k_{FEM}$	65 mN/A
EMs torque const.	$k_{TEM}$	0.93 mNm/A
Force sensor damping	$k_{d,RFS}$	0.04 Ns/m
Force sensor stiffness	$k_{s,RFS}$	694 kN/m
Force sensor el. conv. const.	$k_v$	13.3 μV/μm
Force sensor amplifier gain	$k_{VGA}$	10 V/mV

DOFs, the stiffness related to each DOF, and the robustness of the passive magnetic levitation platform. In the configuration depicted in **Fig. 3.1** as rendering of the final system and in **Fig. 3.2 (a)** as 2D section view, the mover has six DOFs since it can move along and rotate around all axes  $x, y, z$ . The PMs are designed such that the axial position and the rotations around the radial axes  $x, y$  are passively stable, i.e., three DOFs are stable under passive magnetic forces. Only the radial movement in  $x, y$  direction (two DOFs) must be actively controlled to fully stabilize the system. The remaining DOF, which is the rotation around the vertical axis  $z$ , is marginally stable (neither stable nor unstable), which indicates that active control of this DOF is not mandatory, hence, not considered in this chapter. Design optimization of stiffness for various DOFs was conducted in **Chapter 2**. The used method is to set a lower bound on the rotational stiffness of the mover so that it is less prone to rotations due to external disturbances or during the active control of the radial movement, whereas for the radial stiffness, a low value is beneficial for

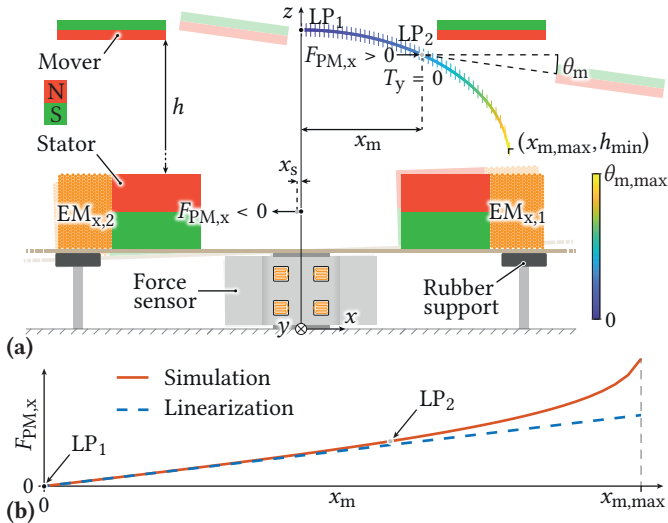


**Fig. 3.2:** (a) Section view of a radial displacement of the mover under destabilizing magnetic forces without active control. (b) The forces that the mover experiences can be measured as reaction forces on the stator and converted with a linear equation to extract the mover's position for the active position control. For the sake of illustration, the EMs' return current path (see **Fig. 3.1**) is not shown, and the levitation height is shown reduced compared to the other dimensions, which are drawn to scale.

the active control since less radial force is needed to keep the mover radially centered. However, trade-offs were faced when choosing those two quantities since increasing the rotational stiffness leads to a reduction of the levitation height, and a reduction of the radial stiffness leads to a proportional reduction of the passive axial stiffness that is required to be large for improving the rejection of external disturbances acting in a vertical direction. Another important aspect to consider during the PMs design is the robustness that can be interpreted as the maximum displacement or angle that the mover can experience from the natural orientation and position (horizontal and radially centered) without changing its passive stability properties. To illustrate the concept of robustness applied to a radial displacement, we consider the designed mover that has three passively stable DOFs at  $LP_1 (x, h) = (0, 104)\text{mm}$  in **Fig. 3.2 (a)** (the axial  $z$ -movement and the rotations around both radial axes  $x, y$ ). The mover can shift to  $(x_{m,\max}, h_{\min}) = (55, 65.5)\text{mm}$  while maintaining the same passively stable DOFs. Correspondingly, the axial robustness is measured by displacing the mover towards the stator starting from  $LP_1$  until a passive stability change is observed. This change occurs at  $h = 2.5\text{ mm}$ , where an axial instability is observed (the mover gets attracted by the stator). Knowing this levitation height and calculating the corresponding axial force determines the maximum payload the mover can carry, resulting in 8.16 kg. Regarding the rotational robustness at  $LP_1$  (without payload), the mover can be rotated around the radial axes  $x, y$  up to  $25^\circ$ . For larger angles, the passive rotational stability is lost. These large robustness bounds allow to stabilize the mover with the same control architecture under external disturbances and different payloads added to the mover; however, for the sake of demonstration, this chapter focuses on the active control of the mover using a force sensor in a preferably small range around the natural levitation point  $LP_1$ , where the mover is unloaded and radially aligned with the stator.

When moved from the center, the mover is tilted as depicted in **Fig. 3.2 (a)** without active control. From the natural position  $LP_1 (x = 0, y = 0, h = 104\text{ mm})$ , where the radial forces are theoretically zero, the levitating magnet starts moving along the colored trajectory, e.g., due to a slight asymmetry in the construction of the PMs, which is arbitrarily chosen to be in positive  $x$  direction. The radial magnetic force on the mover is positive, meaning that the mover keeps rolling away from the initial position and simultaneously rotates by the angle  $\theta_m$  around the perpendicular axis  $y$  due to a passive magnetic torque acting in this direction. Taking a snapshot of the mover's displacement and rotation (e.g., at position  $LP_2$ ), it can be observed that there is only the force  $F_{PM,x} > 0$ , whereas the torque acting on the mover is  $T_y = 0$ ,

making it stable against rotations around the radial axes. Accordingly, the mover keeps a steady-state angle  $\theta_m$  if controlled at a certain radial position  $x_m \neq 0$ . Therefore, the use of a force sensor for determining the mover's position is an attractive option because of the linear relationship between radial force and radial position as depicted in **Fig. 3.2 (b)** for a relatively broad radial range, considering that the mover is typically controlled at  $x_m = 0$  and  $y_m = 0$ . The magnetic force that the mover experiences when it is not radially centered is also observed as reaction force on the stator with equal magnitude but opposite direction, meaning that the mover's position can be indirectly measured with a force sensor, e.g., placed underneath the stator (see **Fig. 3.1**). The force sensor discussed in this chapter is a three-axis load cell employing strain gauges that measure the change of resistance due to the elongation and/or shortening of the gauges, which are glued to the deflecting aluminum elements of the sensor. With this sensing principle, the stator (placed above the sensor) must be able to move when radial forces are acting on the mover as illustrated in **Fig. 3.2**. To allow only a radial movement of the stator with preferably minimal rotation, rubber supports are mounted below the stator mounting plate and fixed to a steady structure, and their impact on the dynamics of the stator is modeled and calibrated with measurements (see **Section 3.4**).

Furthermore, the EMs used for the mover's active stabilization are placed on the stator level to preserve the large levitation height  $h$  and are attached to the stator PM mounting plate so that the electromagnetic forces between EMs and the stator PMs do not act on the force sensor. Otherwise, if the EMs were placed near the stator PMs but mechanically decoupled, large electromagnetic forces between EMs and the stator PMs could saturate the force sensor.

## 3.3 Dynamics Modeling

This section shows a theoretical model of the MLP for the active position control on the radial axis  $x$  for  $y = 0$ ; the same considerations hold for the other radial  $y$  axis (and  $x = 0$ ) since the MLP is axially symmetric. The only differences, as explained in **Subsection 3.4.2**, are due to the asymmetrical construction of the force sensor.

### 3.3.1 Radial Motion Dynamics

As already observed in **Fig. 3.2 (b)**, the magnetic force  $F_{PM}$  acting on the mover for a positive radial displacement is positive and it is shown over  $x_m$

in **Fig. 3.3 (b)** as dotted red curve using the calculation method proposed in **Section 2.2**. In a neighborhood of the wanted levitating point for the mover,  $x_m = 0$  and  $y_m = 0$ , the simulated curve is linearized by a tangent line (centered in the origin and having the same slope as in  $x_m = 0$ ) that defines the radial stiffness, i.e., the proportionality constant between displacement and magnetic force  $k_{\text{FPM}} = |\Delta F_{\text{PM}}/\Delta x_m|$ , whose value is given in **Tab. 3.1** (note that  $k_{\text{FPM}}$  indicates missing natural stability). The force  $F_{\text{EM}}$  generated by the electromagnets is measured with a force sensor by positioning the mover radially centered with the stator and varying the control current with the result shown in **Fig. 3.3 (c)**. Both EMs that can generate a force in  $x$  direction are used with opposite currents  $I_{x,1}$  and  $I_{x,2}$  (see **Fig. 3.3 (a)**), where one drags, and the other pushes the mover, with the convention that a positive force causing a positive movement  $x_m > 0$  is generated by a positive current. For the given position of the mover, the linearization to find  $k_{\text{FEM}} = |\Delta F_{\text{EM}}/\Delta I|$  is not needed since the EMs' magnetic flux density on the mover is directly proportional to the current (Biot-Savart law), and the corresponding Lorentz force is in turn directly proportional to the magnetic flux density **Section 2.2**. Another contribution to the total radial force experienced by the mover is the force  $F_{\text{rot}}$  related to the mover's rotation  $\theta_m$ , e.g., due to the unstable radial motion (see **Fig. 3.2**). The curve obtained with the model **Section 2.2** shown in **Fig. 3.3 (f)** is linearized around  $x_m = 0$  and  $\theta_m = 0$  to obtain the constant  $k_{\text{Frot}} = |\Delta F_{\text{rot}}/\Delta \theta_m|$ . Accordingly, the linear equation of motion that describes the radial displacement of the mover under magnetic and electromagnetic forces in a neighborhood of  $x_m = 0$  and  $\theta_m = 0$  can be written as

$$\begin{aligned} m_m \ddot{x}_m(t) &= F_{\text{PM}}(t) + F_{\text{EM}}(t) + F_{\text{rot}}(t) \\ &= k_{\text{FPM}} x_m(t) + k_{\text{FEM}} I(t) + k_{\text{Frot}} \theta_m(t), \end{aligned} \quad (3.1)$$

where  $m_m$  is the mover's mass and  $t$  indicates the time. To derive the transfer function of the mover's radial dynamics, we set  $\theta_m = 0$  and apply Laplace's transform to (3.1) with the complex variable  $s$ , we find

$$\frac{X_m(s)}{I(s)} = \frac{k_{\text{FEM}}/m_m}{\left(s + \sqrt{\frac{k_{\text{FPM}}}{m_m}}\right) \cdot \left(s - \sqrt{\frac{k_{\text{FPM}}}{m_m}}\right)} \quad (3.2)$$

that shows the instability of the model for the radial movement due to the presence of a real right-half-plane (RHP) pole  $p = \sqrt{k_{\text{FPM}}/m_m}$ . In fact, if a positive current step is applied to the system with the mover initially centered, the trajectory  $x_m(t)$  gets positive due to the positive electromagnetic force

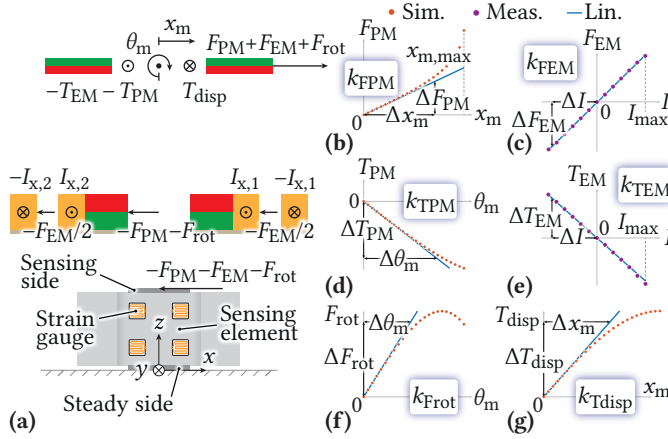


**Fig. 3.3:** (a) Section view of the MLP where the mover is in the center  $x_m = y_m = 0$ , and the force/torque vectors acting on the different parts of the MLP when a current  $I$  is injected into the EMs are shown. (b)-(g) show the linearizations of different simulations and/or measurements performed on the MLP according to **Tab. 3.1** to build a model in the neighborhood of  $x_m = 0$ ,  $y_m = 0$ , and  $\theta_m = 0$ .

and will keep increasing exponentially as time passes due to the positive magnetic force. For completeness, the block diagram of (3.1) (also valid for small  $\theta_m$ ) and the Bode diagram of (3.2) (only valid for  $\theta_m = 0$ ) can be found in **Fig. 3.4 (b)**, where also the natural frequency of the radial displacement of the mover is shown and defined as

$$f_{n,disp} = \frac{1}{2\pi} \cdot \sqrt{\frac{k_{FPM}}{m_m}} = 1.52 \text{ Hz.} \quad (3.3)$$

The basic model described by (3.2) could be used to design a controller if the mover's position is measured directly with a position sensor (see **Subsection 3.4.1**).

### 3.3.2 Rotational Dynamics

The force sensor's reading also depends on the mover's rotation  $\theta_m$ . Therefore, a more sophisticated model of the mover's motion is required because the mover could get too far from the reference center point and start to tilt around the  $y$  axis as depicted in **Fig. 3.2 (a)**. In particular, the tilting can lead to a



wrong reading of the radial position, meaning that a wrong compensation force is generated with the EMs, which could finally lead to an instability of the mover. Due to the low rotational stiffness, the mover also could start tilting due to the torque generated by the EMs while trying to keep the radial position to zero. The current dependent torque with proportionality constant  $k_{\text{TEM}} = |\Delta T_{\text{EM}}/\Delta I|$ , shown in **Fig. 3.3 (e)**, is calculated using the model **Section 2.2** extended to the EMs and is also proven with a different technique described in the following, where the difference between the two methods lies within 8%. The latter approach involves fixing the mover (in the radially centered position) on the  $y$  axis so that it can only freely tilt around that axis without displacements and injecting constant currents in the EMs. For each current, the mover settles to a certain angle  $\theta_m$  because it is stable against tilting and/or rotations around the radial axes, and  $\theta_m$  depends on the rotational stiffness, which is defined as the slope  $k_{\text{TPM}} = |\Delta T_{\text{PM}}/\Delta \theta_m|$  of the dotted curve in **Fig. 3.3 (d)** around the origin. In the reached equilibrium position, the tilting angle can be measured, and the EM torque can be found knowing that it is compensated by the PM torque (i.e.,  $|T_{\text{EM}}| = |T_{\text{PM}}|$ ), which is calculated as described in **Section 2.2**. Another contribution to the total torque experienced by the mover is the torque  $T_{\text{disp}}$  related to the mover's radial displacement  $x_m$ . Correspondingly, the curve depicted in **Fig. 3.3 (g)** is linearized around  $x_m = 0$  and  $\theta_m = 0$  to obtain the constant  $k_{\text{Tdisp}} = |\Delta T_{\text{disp}}/\Delta x_m|$ . Accordingly, the linear equation of the mover's rotation around the radial axes, under PM and EM torques, in a neighborhood of  $x_m = 0$  and  $\theta_m = 0$  can be written as

$$\begin{aligned} J_m \ddot{\theta}_m(t) &= -T_{\text{PM}}(t) - T_{\text{EM}}(t) + T_{\text{disp}}(t) \\ &= -k_{\text{d,rot}} \dot{\theta}_m(t) - k_{\text{TPM}} \theta_m(t) - k_{\text{TEM}} I(t) + k_{\text{Tdisp}} x_m(t), \end{aligned} \quad (3.4)$$

where  $J_m$  is the mover's moment of inertia, and  $k_{\text{d,rot}}$  is a strictly positive damping constant for the rotation, which is given by the magnetic interaction between stator and mover that gives rise to eddy current and hysteresis losses in the PMs [61]. In the  $s$ -domain, (3.4) with  $x_m = 0$  results in

$$\frac{\Theta_m(s)}{I(s)} = \frac{k_{\text{TEM}}}{J_m s^2 + k_{\text{d,rot}} s + k_{\text{TPM}}} \quad (3.5)$$

and shows that the model for the rotation is stable because of the positive coefficients in the denominator (Routh-Hurwitz criterion). However, depending on the constant  $k_{\text{d,rot}}$ , the rotation can be underdamped as shown in the Bode diagram of **Fig. 3.4 (a)**, meaning that oscillations can occur at the natural

frequency

$$f_{n,\text{rot}} = \frac{1}{2\pi} \cdot \sqrt{\frac{k_{\text{TPM}}}{J_m}} = 2 \text{ Hz.} \quad (3.6)$$

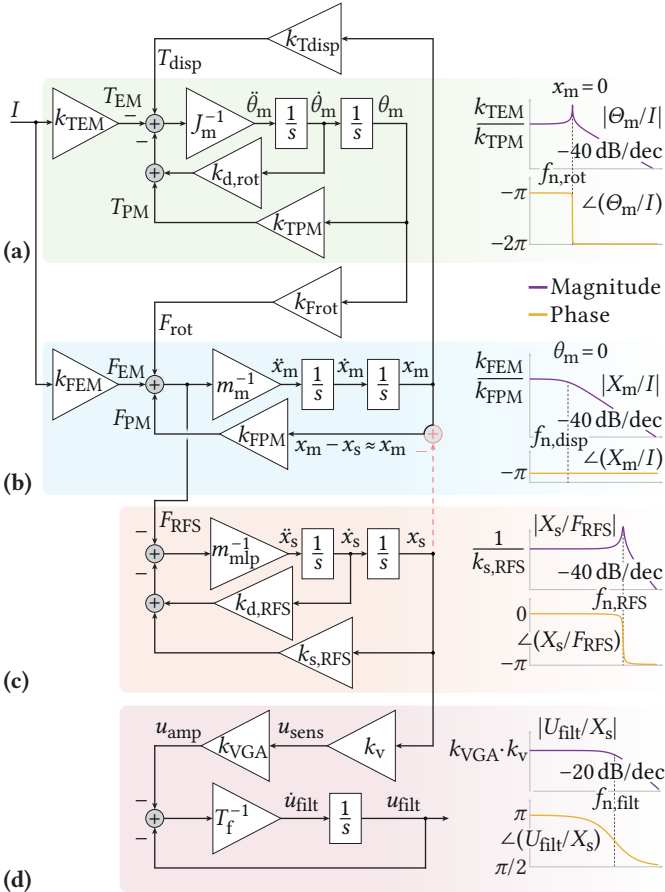


**Fig. 3.4:** Complete block diagram of the MLP where the dynamics of subsystems are also represented with Bode diagrams: **(a)** mover tilting and/or rotation, **(b)** mover displacement, **(c)** force sensor's sensing element mechanical characteristic, and **(d)** force sensor mechanical-to-electrical signal conversion, amplification, and filtering. Parameter values specified in **Tab. 3.1**.

With this extension of the mover's dynamic model, a controller that stabilizes the mover in radial direction and dampens eventual rotary oscillations can be designed given the position  $x_m$  and the rotation  $\theta_m$  as will be shown in **Subsection 3.5.2**.

### 3.3.3 Force Sensor Mechanical Dynamics

When the force sensor is used for position sensing, a further extension of the MLP's dynamic model is required to include the force sensor's dynamics, which is presented in the following. As already illustrated in **Fig. 3.2 (a)**, when the mover is radially displaced with respect to the center position, there is a reaction force acting on the stator that can be assumed to be linearly dependent on the displacement for small deviations, i.e.,  $-F_{PM} = -k_{FPM}x_m$ . In addition, two more forces are acting on the sensor, i.e., the reaction force from the electromagnets  $-F_{EM}$  and a force due to the tilting of the mover  $-F_{rot}$ , as depicted in **Fig. 3.3 (a)**. The electrical signal provided by the force sensor is proportional to the elongation and/or shortening of the strain gauges and, therefore, proportional to the movement of the sensing side of the force sensor (see **Fig. 3.3 (a)**) defined here as  $x_s$ , which is caused by the total dynamic force

$$F_{RFS} = -F_{PM} - F_{EM} - F_{rot}. \quad (3.7)$$

The transfer from applied force  $F_{RFS}$  to the linear movement of the force sensor can be modeled as a mass-spring-damper system (as commonly done in literature [62–64]) with the following equation of motion

$$m_{mlp}\ddot{x}_s(t) = F_{RFS}(t) - k_{d,RFS}\dot{x}_s(t) - k_{s,RFS}x_s(t) \quad (3.8)$$

where  $m_{mlp} = 3.6$  kg is the total mass applied to the force sensor that includes the mass of the PM stator, four EMs, the mounting plate, and the mover,  $k_{d,RFS}$  models the viscous damping for the force sensor and is a strictly positive constant, and  $k_{s,RFS}$  is the stiffness of the force sensor that determines how much the sensing elements bend under constant loads. In the  $s$ -domain, (3.8) results in

$$\frac{X_s(s)}{F_{RFS}(s)} = \frac{1}{m_{mlp}s^2 + k_{d,RFS}s + k_{s,RFS}} \quad (3.9)$$

and shows that the model of the force sensor is stable because of the positive coefficients in the denominator. Also, in this case, the sensor is prone to oscillations at its natural frequency

$$f_{n,RFS} = \frac{1}{2\pi} \cdot \sqrt{\frac{k_{s,RFS}}{m_{mlp}}} = 69.9 \text{ Hz} \quad (3.10)$$

that depend on its damping constant  $k_{d,RFS}$  as illustrated by the peaking in the Bode diagram of **Fig. 3.4 (c)**. In addition, the total force acting on the force sensor causes a tilting of its sensing part and of the whole mounting plate, which is attenuated with the rubber supports shown in **Fig. 3.2 (a)**. This hardware assembly slightly increases the stiffness of the force sensor since the low stiffness of rubber is added to the large stiffness of aluminum, and most importantly, avoids a more complex model for the rotation of the PM stator and EMs around the radial axes. Both stiffnesses are included in the coefficient value in (3.8).

### 3.3.4 Force Sensor Electrical Dynamics

The electrical signal provided by the force sensor depends on the sensitivity of the strain gauges for a given mechanical stiffness, the gain of the electrical circuit, and the optional electrical filter used to attenuate high-frequency noise or electrical disturbances in the system. Therefore, a first-order low pass filter transfer function combined with an inverting amplifier gain  $k_{VGA}$  is used for the model, together with the mechanical-to-electrical signal conversion that is modeled with a constant gain  $k_v$ , which leads to the following transfer function

$$\frac{U_{\text{filt}}(s)}{X_s(s)} = -\frac{k_v \cdot k_{VGA}}{T_f s + 1}, \quad (3.11)$$

where the cutoff frequency is equal to

$$f_{n,\text{filt}} = \frac{1}{2\pi} \cdot \frac{1}{T_f} = 38 \text{ Hz}. \quad (3.12)$$

For completeness, the time-domain representation of (3.11) is given as

$$T_f \dot{u}_{\text{filt}}(t) = -k_v \cdot k_{VGA} x_s(t) - u_{\text{filt}}(t), \quad (3.13)$$

and depicted in **Fig. 3.4 (d)**. The gain  $k_v$  can be determined by displacing the mover in the vicinity of the levitating point  $x_m = y_m = 0$  by  $\Delta x_m$  with  $I = 0$  and  $\theta_m = 0$  while measuring the electrical response  $\Delta u_{\text{amp}}$  of the force sensor. With the prior knowledge of the sensor's stiffness  $k_{s,RFS}$ , the mover's radial displacement stiffness  $k_{FPM}$ , and the electrical amplification factor  $k_{VGA}$ , the gain is obtained as

$$k_v = \left| \frac{\Delta u_{\text{amp}}}{\Delta x_m} \right| \cdot \frac{1}{k_{VGA}} \cdot \frac{k_{s,RFS}}{k_{FPM}}. \quad (3.14)$$

Strictly speaking, the gauges have specific dynamics since their stretch cannot happen instantly. However, these dynamics are simplified here with

the constant  $k_v$  since, according to the design, the stretching occurs almost simultaneously with the bending of the sensing element [65], which is limited by the frequency  $f_{n,RFS}$ . The electrical amplification is simplified with the constant  $k_{VGA}$  since the chosen cutoff frequency of the filter  $f_{n,fil}$  is much lower than the electrical bandwidth of the used amplifier, which lies in the megahertz range [66]. Furthermore, it is important to note that the overall sensor's bandwidth, i.e., the  $-3$  dB frequency of the transfer function  $U_{fil}(s)/F_{RFS}(s)$ , must be sufficiently larger than the other characteristic frequencies in the system ( $f_{n,disp}$  and  $f_{n,rot}$ ) in order to correctly measure the position and tilting-dependent forces of the mover without excessive phase shift. Otherwise, wrong estimations of  $x_m$  and  $\theta_m$  can occur, leading to incorrect EM forces defined by the controller that would ultimately destabilize the system.

### 3.3.5 Summary of the Dynamics

The dynamic equations (3.1), (3.4), (3.7), (3.8), and (3.13) are shown in the form of a block diagram in **Fig. 3.4**, where the single input is the current  $I$  through the EMs and the single output is the amplified and filtered voltage of the force sensor  $u_{fil}$ . In the diagram, a simplification can be done assuming that the movement of the stator is negligible compared to the mover's radial movement (red dashed connection in **Fig. 3.4**). Strictly speaking,  $F_{PM} = k_{FPM}(x_m - x_s)$  holds, assuming that the sensing side of the force sensor moves. However, given any mover's position  $x_m = F_{PM}/k_{FPM}$  and knowing that the same magnetic force acts on the stator, its displacement can be calculated as  $x_s = -F_{PM}/k_{s,RFS} = -k_{FPM}/k_{s,RFS} \cdot x_m = -4.7 \cdot 10^{-5} \cdot x_m$  with the constants given in **Tab. 3.1**. Therefore, the stator's displacement contribution to the magnetic force is small and can be neglected, i.e., the simplification  $F_{PM} = k_{FPM}x_m$  is justified. Correspondingly, the complete and simplified model of the MPL is expressed with the following state-space equations

$$\dot{x}(t) = Ax(t) + Bu(t) \quad (3.15)$$

$$y(t) = Cx(t) \quad (3.16)$$

with the input, output, and state variables

$$u(t) = I(t) \quad (3.17)$$

$$y(t) = u_{fil}(t) \quad (3.18)$$

$$x(t) = [\theta_m(t) \quad \theta_m(t) \quad \dot{x}_m(t) \quad x_m(t) \quad \dot{x}_s(t) \quad x_s(t) \quad u_{fil}(t)]^T \quad (3.19)$$

and the corresponding matrices

$$A = \begin{bmatrix} -\frac{k_{d,rot}}{J_m} & -\frac{k_{TPM}}{J_m} & 0 & \frac{k_{Tdisp}}{J_m} & 0 & 0 & 0 \\ 1 & 0 & 0 & 0 & 0 & 0 & 0 \\ 0 & \frac{k_{Frot}}{m_m} & 0 & \frac{k_{FPM}}{m_m} & 0 & 0 & 0 \\ 0 & 0 & 1 & 0 & 0 & 0 & 0 \\ 0 & -\frac{k_{Frot}}{m_{mlp}} & 0 & -\frac{k_{FPM}}{m_{mlp}} & -\frac{k_{d,RFS}}{m_{mlp}} & -\frac{k_{s,RFS}}{m_{mlp}} & 0 \\ 0 & 0 & 0 & 0 & 1 & 0 & 0 \\ 0 & 0 & 0 & 0 & 0 & -\frac{k_v k_{VGA}}{T_f} & -\frac{1}{T_f} \end{bmatrix} \quad (3.20)$$

$$B = \begin{bmatrix} -\frac{k_{TEM}}{J_m} & 0 & \frac{k_{FEM}}{m_m} & 0 & -\frac{k_{FEM}}{m_{mlp}} & 0 & 0 \end{bmatrix}^T \quad (3.21)$$

$$C = [0 \ 0 \ 0 \ 0 \ 0 \ 0 \ 1]. \quad (3.22)$$

The Bode diagram of the transfer function

$$G_{tot}(s) = \frac{U_{filt}(s)}{I(s)}, \quad (3.23)$$

for currents through the EMs with different frequencies while the mover levitates around the center position is shown in **Fig. 3.5**. In addition, the poles (seven in total) of the transfer functions (3.2), (3.5), (3.9), and (3.11) are shown with their real and imaginary part. The diagram clearly shows two magnitude peaks at  $f_{n,rot}$  and  $f_{n,RFS}$ , resulting from poles that possess a larger imaginary component relative to their real component. Additionally, the noticeable dip near  $f_{n,rot}$  is attributed to a pair of zeros located very close to the poles indicated by green dots.

### 3.4 Dynamic Model Verification and Tuning

To validate in a first step the complete dynamic model of the system, a measurement of the total transfer function  $G_{tot} = U_{filt}/I$  has to be performed, where the stator PM and the EMs are mounted on the force sensor, and the mover levitates at the reference operating point while being able to move and tilt freely. For this purpose, an optical position sensor with sufficient bandwidth (at least ten times higher than  $\omega_0 = 2\pi \cdot 2 \text{ Hz}$ , e.g., 2.5 kHz [67]) directly measures the mover's position and feeds the signal to a position controller that stabilizes the mover. In addition, sinusoidal currents are injected into the EMs, which excite the mover's radial  $x$  position around the levitating point. At the same time, the electrical output of the force sensor is

being recorded. This method verifies the total transfer function depicted in Fig. 3.5 (cf. with Fig. 3.8).

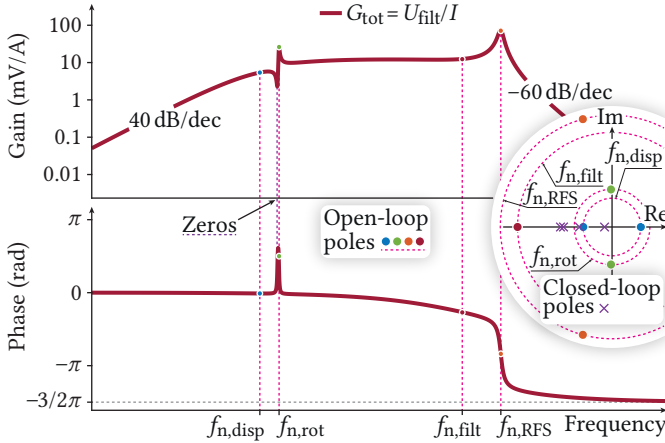


**Fig. 3.5:** Bode diagrams of the model for the MLP (see Fig. 3.4) with an inset showing the location of the seven poles of the system in the complex plane. A single pole is in the RHP and corresponds to the radial displacement of the mover (see (3.2)), whereas the poles describing the mover rotation and the force sensor dynamics are stable but show a relatively large imaginary part that implies oscillations in the system. The magnitude and frequency axes have a logarithmic scale.

### 3.4.1 Mover's Position Controller

A position controller that actively stabilizes the radial position of the mover is required for levitation at the desired operating point. Furthermore, the method for the position sensing has to be preferably independent of the mover's tilting around the radial axes such that only the part of the model of Subsection 3.3.1 describing the radial motion, e.g., along the  $x$  axis, can be used to design the controller. Consequently, if a tilting of the mover still occurs, it does not influence the sensor readings detrimentally and is naturally damped by passive magnetic interactions. The proposed approach depicted in Fig. 3.6 is to use a PD-controller that stabilizes the mover's radial displacement along the  $x$  axis by shifting the unstable pole to the left-half-plane (LHP) combined with a PI-controller that enables steady-state reference tracking. To verify the dynamic model of the complete system, including the force sensor, the position signal  $x_m$  is directly measured with an external

optical sensor (Baumer OM70-Po14o.HHo13o.VI, [67]) and filtered with a first-order low pass filter  $G_{\text{filt}}$ . With the straightforward method proposed in the following to design both controllers, a phase margin of about  $52^\circ$  at the desired crossover frequency is guaranteed. Nevertheless, other approaches can be implemented to get the desired system response, e.g., implementing and tuning a single PID-controller. The stabilization can be achieved by measuring the position  $x_m$ , deriving it to obtain the mover's velocity, and injecting a stabilizing current  $I_{\text{PD}}$  into the EMs proportional to these two quantities so that (3.1) with the simplification  $\theta_m = 0$  is extended to

$$\begin{aligned} m_m \ddot{x}_m(t) &= F_{\text{PM}}(t) - F_{\text{EM,PD}}(t) + F_{\text{EM,PI}}(t) \\ &= k_{\text{FPM}} x_m(t) - k_{\text{FEM}}(k_{\text{D1}} \dot{x}_m(t) + k_{\text{P1}} x_m(t)) + k_{\text{FEM}} I_{\text{PI}}(t), \end{aligned} \quad (3.24)$$

where  $k_{\text{P1}}$  and  $k_{\text{D1}}$  are the proportional and derivative gains of the PD-controller, respectively. It must be ensured that the measured mover's position and speed are equal to the actual ones, i.e.,  $x_{m,\text{meas}} = x_m$  and  $\dot{x}_{m,\text{meas}} = \dot{x}_m$ , for frequencies below the force sensor's bandwidth (or the cutoff frequency of the measurement filter  $G_{\text{filt}}$ ), which should be ten times higher than the natural frequency of the mover's dynamics  $f_{n,\text{disp}}$  as a commonly used guideline in control systems. Therefore, in the following analysis, it is assumed that the sensor's dynamics have no impact on the design of the controller. In the frequency domain, the transfer function from the EMs' current to the mover's

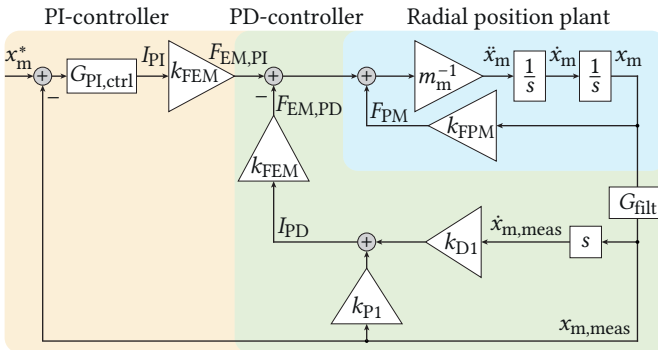


**Fig. 3.6:** Block diagram of the mover's position control built with a PD-controller that stabilizes the unstable radial dynamics and a reference tracking PI-controller.



position can be expressed as

$$\frac{X_m(s)}{I_{PI}(s)} = \frac{k_{FEM}/m_m}{s^2 + \frac{k_{FEM}k_{D1}}{m_m}s + \frac{k_{FEM}k_{P1} - k_{FPM}}{m_m}} \quad (3.25)$$

and has two stable poles if and only if the coefficients in the denominator are strictly positive (Routh-Hurwitz criterion), meaning that the minimal requirements  $k_{D1} > 0$  and  $k_{P1} > k_{FPM}/k_{FEM}$  must be satisfied. This also shows that a derivative controller must be implemented; otherwise, when  $k_{D1} = 0$ , either an unstable real pole still exists for  $k_{P1} < k_{FPM}/k_{FEM}$ , or two purely imaginary poles are obtained if the mentioned requirement for the proportional gain is fulfilled, leading to an oscillatory behavior. Furthermore, comparing the denominator of (3.25) with the standard form of a second-order systems

$$s^2 + 2\zeta\omega_0s + \omega_0^2, \quad (3.26)$$

where  $\omega_0 = 2\pi f_0 > 0$  is the natural frequency, and  $\zeta > 0$  is the damping ratio, expressions for the PD-controller gains can be obtained

$$k_{P1} = \frac{\omega_0^2 m_m + k_{FPM}}{k_{FEM}} \quad (3.27)$$

$$k_{D1} = \frac{2\zeta\omega_0 m_m}{k_{FEM}}. \quad (3.28)$$

It can be seen that the aforementioned basic requirements are satisfied regardless of the chosen natural frequency and damping ratio, meaning that a stabilization of the mover is theoretically always possible for each pair  $(\omega_0, \zeta) > (0, 0)$ . For the sake of simplicity, the PI-controller

$$G_{PI,ctrl}(s) = k_{P2} + \frac{k_{I2}}{s} = \frac{k_{I2}(1 + \frac{k_{P2}}{k_{I2}}s)}{s} \quad (3.29)$$

is designed so that its corner frequency is the same as the chosen natural frequency for the stabilized plant given by (3.25), i.e.  $k_{I2}/k_{P2} = \omega_0$ , and its constant gain is the inverse constant gain of (3.25), leading to the following equations for the controller gains

$$k_{P2} = \frac{k_{FEM}k_{P1} - k_{FPM}}{k_{FEM}} = \frac{\omega_0^2 m_m}{k_{FEM}} \quad (3.30)$$

$$k_{I2} = \omega_0 k_{P2} = \frac{\omega_0^3 m_m}{k_{FEM}}. \quad (3.31)$$

Eventually, multiplication of (3.25) and (3.29) considering the corresponding gains (3.27), (3.28), (3.30), and (3.31), the expression

$$G_{OL}(s) = \frac{s + \omega_0}{s} \cdot \frac{\omega_0^2}{s^2 + 2\zeta\omega_0s + \omega_0^2} \quad (3.32)$$

is obtained. To show that the above stated phase margin at the desired crossover frequency can be achieved, the damping ratio has to be chosen as

$$\zeta = 1 \quad (3.33)$$

so that a critical damping of the PD-controller stabilized plant (3.25) is obtained, meaning that no overshoots or oscillations while stabilizing the mover's position are expected. Accordingly, (3.32) can be rewritten as

$$G_{OL}(s) = \frac{\omega_0^2}{s(s + \omega_0)}. \quad (3.34)$$

The crossover frequency  $\omega_c$  is found at the frequency where the magnitude of (3.34) is unity substituting the complex variable  $s = j\omega_c$ , i.e., solving

$$|G_{OL}(j\omega_c)| = \left| \frac{\omega_0^2}{j\omega_c(j\omega_c + \omega_0)} \right| = 1 \quad (3.35)$$

for  $\omega_c$ , where the only positive and real solution that can be found is

$$\omega_c = \frac{\sqrt{\sqrt{5} - 1}}{\sqrt{2}} \cdot \omega_0 = k_\omega \cdot \omega_0 \approx 0.786 \cdot \omega_0, \quad (3.36)$$

which means that the crossover frequency is linearly dependent on the natural frequency that can be arbitrarily chosen. Consequently, the phase of the open-loop transfer function at the crossover frequency can be calculated as

$$\angle(G_{OL}(j\omega_c)) = -90^\circ - \tan^{-1}(k_\omega) \approx -128.2^\circ \quad (3.37)$$

and it is independent of the chosen crossover or natural frequency, meaning that the phase margin is always given as

$$\text{pm} = \angle(G_{OL}(j\omega_c)) + 180^\circ \approx 51.8^\circ. \quad (3.38)$$

Finally, the closed-loop transfer function that defines the response of the controlled system is given as

$$G_{CL}(s) = \frac{x_m(s)}{x_m^*(s)} = \frac{G_{OL}(s)}{1 + G_{OL}(s)} = \frac{\omega_0^2}{s^2 + \omega_0s + \omega_0^2} \quad (3.39)$$

and shows a typical second-order system response when comparing its denominator with (3.26), where the natural frequency (or bandwidth) is  $\omega_0$ , and the damping ratio is 0.5, meaning that an overshoot in the mover's position is expected when the controller is trying to track, e.g., a step reference signal  $x_m^*$ .

In summary, the only parameter that has to be chosen with the proposed design technique is the bandwidth of the closed-loop system  $\omega_0$ , and together with the requirement (3.33), the four controller gains (3.27), (3.28), (3.30), and (3.31) can be calculated. Note that a trade-off between fast dynamics and required control current has to be faced since choosing a large bandwidth automatically leads to an increased EM current because all controller gains are dependent on  $\omega_0$ , and they determine the required current depending on the mover's position and velocity, as can be seen in **Fig. 3.6**. Therefore, the maximum achievable bandwidth depends on the current limit, which should not be exceeded to ensure a proper controller function and is usually given by the power electronics that supplies the current to the EMs.

### 3.4.2 Dynamic Model Proof and Adaption

For the verification of the dynamic model of the system, a measurement of the transfer function in the frequency domain from the EM current to the force sensor output is performed on the  $x$  and  $y$  axis individually, where the mover is free to travel on the investigated axis while its movement is restricted on the other axis with a customized barrier that allows a sliding with little friction (see **Fig. 3.7 (a)**). For this preliminary test, the mover is actively controlled on the investigated axis in the radially centered position with an optical sensor [67] placed at the mover's level, which allows measuring the position with  $10\ \mu\text{m}$  accuracy. The controller is implemented with the structure discussed in **Subsection 3.4.1**, where the only design parameter is the closed-loop bandwidth, and it is chosen to be  $\omega_0 = 2\pi \cdot 2\ \text{Hz}$ . Higher controller bandwidths up to 5 Hz have been tested, but the system was more prone to vibratory behavior. To record desired transfer functions, sinusoidal currents  $i_{\text{exc}}$  at different frequencies are added to the control currents and injected into the EMs (see **Fig. 3.7 (b)**) to cause a displacement of the mover in a neighborhood of the levitation point of the investigated axis, and all reaction forces on the stator are measured with the force sensor. As schematically shown in **Fig. 3.7 (a)**, the electrical signals coming from the force sensor are amplified, filtered, and stored on the SoC as  $u_{\text{out},x}$  and  $u_{\text{out},y}$  (the subscript letters  $x$  and  $y$  are introduced to distinguish the quantities between the axes). Ideally, the

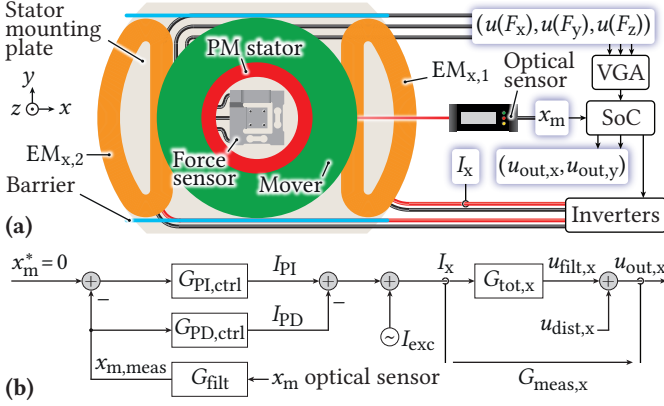


**Fig. 3.7:** (a) Top view of the measurement setup to verify the MLP’s dynamic model in  $x$  direction, where the mover’s position is controlled based on an optical position measurement and sinusoidal currents are injected into the EMs to cause a displacement of the mover and, consequently, a reaction on the stator measured with the force sensor while the  $y$  position is kept constant at  $y_m = 0$  with sliding barriers. (b) Block diagram of the control system from Fig. 3.6 that levitates the mover while currents  $I_{exc}$  are summed to the control currents to verify  $G_{tot,x}$  from Fig. 3.5 by measuring  $G_{meas,x}$ .

voltage  $u_{out,x}$  should be determined by the multiplication of the theoretical system’s transfer function with the EMs’ current (i.e., without disturbances  $u_{dist,x} = 0$  in Fig. 3.7 (b),  $U_{out,x}(s) = U_{filt,x}(s) = G_{tot,x}(s) \cdot I_x(s)$ ). The voltage  $u_{out,y}$  should ideally be zero for all frequencies with the assumption that no cross-coupling between  $I_x$  and  $u_{out,y}$  exists. Additionally, the current is considered to be the mean value between the individual EM currents, i.e.,  $I_x = (I_{x,1} - I_{x,2})/2$ , where the negative sign is due to the opposite directions of the currents in the two coils of an axis (see Fig. 3.1) to generate a force on the mover in one direction.

The resulting measured system’s transfer function of the preliminary test on the  $x$  axis is shown in Fig. 3.8 (a) as a series of cyan points in the frequency range 0.1 Hz – 200 Hz, where the gain and phase have been calculated over at least eighteen periods for the lowest frequency and up to fifty for the largest frequency. When comparing the measurement with the theoretical transfer function (solid red line) already shown in Fig. 3.5, a good agreement can be observed from the natural frequency of the mover’s rotation (tilting)  $f_{n,rot} = 2$  Hz up to the force sensor’s natural frequency  $f_{n,RFS} = 69.9$  Hz. At

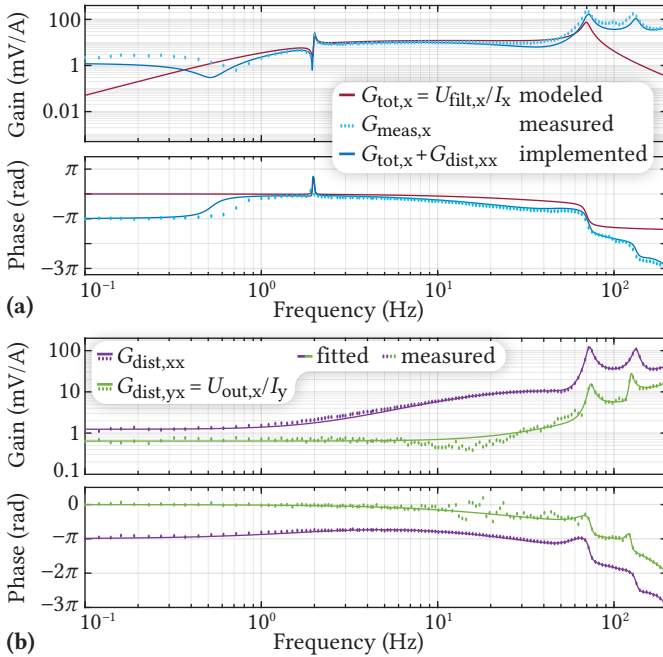


**Fig. 3.8:** (a) shows the frequency responses of the model, measurement, and disturbance corrected  $x$  axis force sensor output to an input current in  $x$  direction (with mover levitating), whereas (b) shows the model disturbance  $G_{\text{dist},xx}$  with the cross-coupling between  $y$  current and  $x$  sensor output  $G_{\text{dist},yx}$  (without mover). Please note that the measured phase lies within  $[-\pi, \pi]$  but has been unwrapped for the representation (i.e., adjusted by adding or subtracting  $2\pi$  to targeted phase values to ensure a continuous and smooth representation without discontinuities).

these resonant frequencies, the constants  $k_{d,\text{rot}}$ ,  $k_{d,\text{RFS}}$ , and  $k_{s,\text{RFS}}$  are finely tuned to match the measured peakings, resulting in the values reported in **Tab. 3.1**. While performing measurements in this frequency range, the mover has a small displacement from the radially centered position up to 1 mm for the lower frequencies, where also a rotation around the  $y$  axis can be observed, and a vibratory behavior from 6 Hz up to 10 Hz. The mover holds the centered position for larger frequencies because of its large inertia that does not allow larger movements, meaning that only the reaction forces caused by the EMs are applied to the force sensor, as PM forces would only occur for a finite displacement and/or rotation of the mover. For frequencies lower than 2 Hz,

where the mover is displaced up to 4 mm from the center, there is a mismatch between the model and the measurements. The dip in the transfer function at 1.96 Hz due to the cancellation of all reaction forces described with the help of **Fig. 3.5** is still visible, but the increasing gain connected to a phase equal to zero in the lowest frequency region could not be measured in the real system. Another discrepancy with the model is found at frequencies larger than 70 Hz due to a vibratory mode of the whole mechanical system, where a peak near 130 Hz is prominent. This behavior is commonly found in complex mechanical structures involving multiple parts [68]. In summary, the important characteristics of the theoretical model are visible in the measured transfer function. However, some deterministic behavioral differences must be addressed before the force sensor signal can be used for the feedback control of the mover.

These differences are visible when performing a second measurement, where the mover is removed from the system, and sinusoidal currents are injected into the EMs (as during the first measurement, the axes are considered individually). Following the model of **Fig. 3.4**, the force sensor should not register forces since all reaction forces from the mover ( $F_{PM}$ ,  $F_{EM}$ , and  $F_{rot}$ ) are zero. Accordingly, the electrical signal  $u_{out,x}$  should be zero regardless of the injected current. However, as shown by **Fig. 3.8 (b)**, transfer functions with a gain comparable to the modeled transfer function  $G_{tot,x}$  are measured.  $G_{dist,xx}$  represents the disturbance on the modeled function  $G_{tot,x}$  and is obtained by injecting  $I_x$  in the EMs and measuring  $u_{out,x}$  without a mover. Therefore, it differs from the measurement  $G_{meas,x}$  with the mover levitating reported in **Fig. 3.8 (a)**. Nevertheless, it can be seen that the two peaks around 70 Hz and 130 Hz are still visible, indicating that forces are acting on the force sensor, which originate from the electromagnetic forces between the EMs and the PM stator. They generate a displacement of both objects (EMs and PM stator) on the stator mounting plate due to the poor mechanical mounting, finally resulting in a movement of the force sensor's sensing side. This effect is also observed at the lowest frequencies, explaining the relatively large gain compared to the model. Furthermore, in the frequency range above 1 Hz, another effect that directly affects the strain gauges is observed, namely, induced voltages that are summed to the force-dependent voltages and are caused by the time-varying magnetic fields from the electromagnets. The origin of both disturbances can be proven by removing the PM stator from the system, where only the induced voltages can be measured with a phase of  $\pi/2$  with respect to the current in the EMs. Eventually, fitting the measurement of  $G_{dist,xx}$  with the transfer function estimation tool provided by MATLAB® and

adding the obtained frequency response to the model transfer function  $G_{\text{tot},x}$ , the measurement performed with the mover levitating can be reproduced with better accuracy (cf.  $G_{\text{meas},x}$  with  $G_{\text{tot},x} + G_{\text{dist},xx}$  in **Fig. 3.8 (a)**). The error that remains between the transfer functions can be attributed to the fact that the two measurements (with and without mover) are performed separately and that the model parameters also present an error originating from their measurement and/or simulation. Another behavior that is hard to model but is prominent in the output of the force sensor, as shown in **Fig. 3.8 (b)**, is the cross-coupling between the axes, which is indicated by the transfer function  $G_{\text{dist},yx}$ , for the force sensor output  $u_{\text{out},x}$  due to a current  $I_y$ , where the system is excited without the mover. For this measurement, the same disturbances as for  $G_{\text{dist},xx}$  are visible, where the movement of the stator and EMs in the  $y$  direction causes a false reading in the  $x$  direction and vice versa. For this measurement, the amplitude of the disturbance on the sensor output is slightly above the noise level for the lower frequency range. Between 10 Hz and 25 Hz only noise is measured, as can be seen by the distribution of the measurement points, especially in the phase plot.

The same measurement procedure is performed to characterize the  $y$  axis of the sensor where similar results are expected due to symmetry. However, a small difference is observed in the sensor's natural frequency ( $f_{n,FS,y} = 62.2$  Hz compared to  $f_{n,FS,x} = 69.9$  Hz) due to the different stiffness of the sensing elements, and a 25% higher damping coefficient is recognized. Therefore, an adaption of the theoretical model (3.15) regarding the sensor's parameters is performed, leading to an accordingly different model transfer function  $G_{\text{tot},y}$ . Furthermore, a comparable yet dissimilar disturbance profile is recognized, resulting from the above described disturbance influences. Finally, a transfer function  $G_{\text{dist},yy}$  is used to consider the model disturbance on the  $y$  axis from the  $y$  current and  $G_{\text{dist},xy}$  for the cross-coupling originating from the  $x$  current.

## 3.5 Observer and Controller Design

### 3.5.1 Observer

The proposed position sensing method uses a force sensor that detects the forces due to the mover's motion, which are then turned into the position using the model and calibrated disturbance transfer functions. These calculations are performed by an observer that estimates the states of the system depending on the input variable, i.e., measured EMs' current  $I_{\text{meas},x}$ , using (3.15). Moreover, the observed states are corrected with a state correction

architecture (which is required to deal with model mismatches and noise) by comparing the calculated output (3.16) to the measured output  $u_{\text{out},x}$ . If the observer and the real system react the same way to an input current, the error between the estimated output and measured output would be zero, meaning that the calculated mover's dynamic behavior is the same as in the real-life hardware demonstrator. However, as seen in **Fig. 3.8 (a)**, there are relatively large mismatches due to the disturbances between the theoretical model and measurements. Thus, a correction of the observed states has to be performed so that, ultimately, the output of the observer matches the measured output. Therefore, to minimize the observer's state errors, a dynamic model that matches the measured transfer function of **Fig. 3.8 (a)** has to be implemented on the SoC. As argued in **Subsection 3.4.2**, the disturbance of the model  $G_{\text{dist},xx}$  is completely decoupled from the mover's dynamics. Hence, it can be used to better estimate the real output of the force sensor by summing its response to the response of the original model  $G_{\text{tot},x}$ , as schematically shown in **Fig. 3.9**. This way, the original seven states are still corrected with the feedback architecture of a Kalman filter as described in [69], whereas the model disturbance is used as a feedforward block that directly affects the observer's output  $\tilde{u}_{\text{out},x}$ . Furthermore, the cross-coupling function is incorporated in the observer as an additional feedforward block to enhance the tracking of the states since best all non-ideal disturbances are added to calculate the estimated  $x$  axis force sensor output depending on the currents on both axes. The same observer structure is implemented for the  $y$  axis with the discussed calibration-based improvements of the model, like the measured disturbance and cross-coupling transfer functions. Accordingly, the observed outputs for both axes are written in the  $s$ -domain as

$$\begin{aligned} \tilde{U}_{\text{out},x}(s) = & (G_{\text{tot},x}(s) + G_{\text{dist},xx}(s)) \cdot I_x(s) \\ & + G_{\text{dist},yx}(s) \cdot I_y(s) \end{aligned} \quad (3.40)$$

$$\begin{aligned} \tilde{U}_{\text{out},y}(s) = & (G_{\text{tot},y}(s) + G_{\text{dist},yy}(s)) \cdot I_y(s) \\ & + G_{\text{dist},xy}(s) \cdot I_x(s). \end{aligned} \quad (3.41)$$

### 3.5.2 Mover's Position Controller and Rotation Damping

As discussed in the previous sections, the magnetic levitation platform requires at least active control of the mover's radial  $x$ ,  $y$  position since it is intrinsically unstable. However, an active contribution to damping other stable DOFs might also be required, especially when the mover oscillates due to poor passive damping. In addition to stabilizing the mover's radial



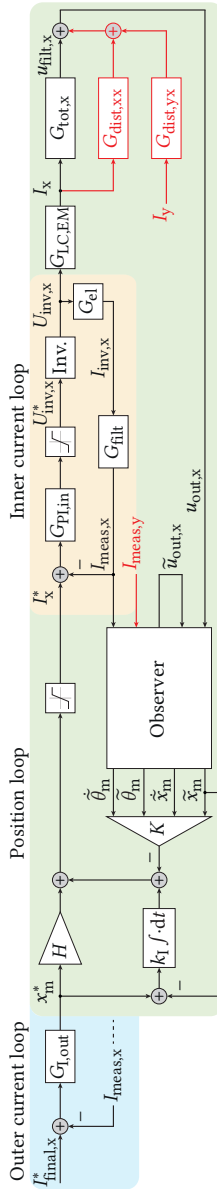


**Fig. 3-9:** Block diagram of the MLP with the mover's dynamics observer, position, and current controllers for the x axis. The black boxes represent the ideal MLP as presented up to and including **Section 3-3**, whereas the red boxes are required to extend the model for the realized prototype discussed in **Subsection 3-4.2** so that the observer delivers the states as close as possible to the reality to the position controller. For these disturbance corrections, the y axis current plays a role in the x axis model and vice versa.

position like the one described in **Subsection 3.4.1**, the proposed controller actively dampens eventual rotary oscillations. Therefore, the mover's position  $x_m$  and tilting angle  $\theta_m$  must be measured. As seen before, to stabilize the radial position, the velocity  $\dot{x}_m$  is required, whereas for the active damping of the rotation, the angular speed  $\dot{\theta}_m$  is necessary; advantageously both can be found from the derivative of the position measurements  $x_m$  and  $\theta_m$  over time. The proposed approach is a state-space (or time-domain) stabilizing controller based on a reduced state-space representation of the MLP that only considers the mover's dynamics. The force sensor's mechanical and electrical dynamics must not be controlled since the movement of the sensing side is relatively small and has practically no impact on the magnetic forces. Accordingly, the model assumes that the observed quantities ( $\tilde{x}_m, \dot{\tilde{x}}_m, \tilde{\theta}_m, \dot{\tilde{\theta}}_m$ ) are equal to the real-life quantities ( $x_m, \dot{x}_m, \theta_m, \dot{\theta}_m$ ) and it is expressed as

$$\dot{x}_{\text{ctrl}}(t) = A_{\text{ctrl}}x_{\text{ctrl}}(t) + B_{\text{ctrl}}u(t) \quad (3.42)$$

$$y_{\text{ctrl}}(t) = C_{\text{ctrl}}x_{\text{ctrl}}(t) \quad (3.43)$$

with the input, output, and state variables

$$u(t) = I(t) \quad (3.44)$$

$$y_{\text{ctrl}}(t) = x_m(t) \quad (3.45)$$

$$x_{\text{ctrl}}(t) = [\dot{\theta}_m(t) \quad \theta_m(t) \quad \dot{x}_m(t) \quad x_m(t)]^T \quad (3.46)$$

and the corresponding matrices

$$A_{\text{ctrl}} = \begin{bmatrix} -\frac{k_{d,\text{rot}}}{J_m} & -\frac{k_{\text{TPM}}}{J_m} & 0 & \frac{k_{\text{rdisp}}}{J_m} \\ 1 & 0 & 0 & 0 \\ 0 & \frac{k_{\text{Frot}}}{m_m} & 0 & \frac{k_{\text{FPM}}}{m_m} \\ 0 & 0 & 1 & 0 \end{bmatrix} \quad (3.47)$$

$$B_{\text{ctrl}} = \begin{bmatrix} -\frac{k_{\text{TEM}}}{J_m} & 0 & \frac{k_{\text{FEM}}}{m_m} & 0 \end{bmatrix}^T \quad (3.48)$$

$$C_{\text{ctrl}} = [0 \quad 0 \quad 0 \quad 1]. \quad (3.49)$$

This representation can be used independent of the position sensing method as long as the position  $x_m$  and the rotation  $\theta_m$  are obtained. As already mentioned, the mover's velocity  $\dot{x}_m$  and angular velocity  $\dot{\theta}_m$  can be calculated by deriving the position and the angle. The controller in the form of a matrix  $K$  uses all available information, in this particular case, coming from the observer (see **Fig. 3.9**) and calculates the current

$$u(t) = -Kx_{\text{ctrl}}(t) = -[k_1 \quad k_2 \quad k_3 \quad k_4]x_{\text{ctrl}}(t) \quad (3.50)$$

that stabilizes and dampens both mover's dynamics (note  $u(t) = I(t)$ , see (3.17)). The value of the controller gains can be found, for example, using the linear quadratic regulator (LQR) algorithm [70], which is widely used in the literature [71–73] and results in the optimal input  $u(t)$  following the control strategy (3.50) that minimizes the cost function

$$V = \int_0^{\infty} x_{\text{ctrl}}^{\top}(t) Q x_{\text{ctrl}}(t) + u(t) R u(t) dt, \quad (3.51)$$

where  $Q$  is a symmetric and positive definite matrix, and  $R$  is a strictly positive weighting constant. The state-space matrices  $A_{\text{ctrl}}$  and  $B_{\text{ctrl}}$ ,  $Q$  and  $R$  define the control matrix  $K$  by solving the continuous-time algebraic Riccati equation for the matrix  $P$  as

$$A_{\text{ctrl}}^{\top} P + P A_{\text{ctrl}} - \frac{1}{R} \cdot P B_{\text{ctrl}} B_{\text{ctrl}}^{\top} P + Q = 0 \quad (3.52)$$

$$K = \frac{1}{R} \cdot B_{\text{ctrl}}^{\top} P. \quad (3.53)$$

For the design of the stabilizing controller component, a choice of weights has to be performed and is shown in **Subsection 3.6.2**, where the single states and the input variable can be penalized in the cost function such that the algorithm finds a controller that ensures strong damping of the rotation while maintaining the mover stable in the radial direction. As a consequence, the unstable pole due to the radial magnetic forces is taken to the LHP, as well as decreasing the imaginary component of the rotation-related poles so that all four poles lie on the negative real axis or as close as possible to it, as shown by the violet crosses in the complex plane of **Fig. 3.5**. Furthermore, the stabilizing controller component is extended with a reference tracking system [74] consisting of a proportional and an integral part as illustrated in **Fig. 3.9** that allows following a reference radial position  $x_m^*$ , which is normally set to zero so that the mover is kept radially centered, considering that the position signal  $x_m$  has no offset. Conversely, rotation (tilting) tracking is not implemented since the reference mover's angle is zero and corresponds to the natural angle when centered. The proportional controller consists of a constant  $H$  that is chosen so that at steady-state (i.e., when  $\dot{x}_{\text{ctrl}}(t) = 0$ ), the position of the mover is equal to the reference value with the extended control strategy

$$u(t) = -K x_{\text{ctrl}}(t) + H x_m^*(t). \quad (3.54)$$

Therefore, the set of equations

$$0 = (A_{\text{ctrl}} - B_{\text{ctrl}}K)x_{\text{ctrl}}(t) + B_{\text{ctrl}}Hx_m^*(t) \quad (3.55)$$

$$y(t) = x_m^*(t) = C_{\text{ctrl}}x_{\text{ctrl}}(t) \quad (3.56)$$

has to be solved for  $H$  leading to the result

$$H = -(C_{\text{ctrl}}(A_{\text{ctrl}} - B_{\text{ctrl}}K)^{-1}B_{\text{ctrl}})^{-1}. \quad (3.57)$$

The integral controller is required to ensure that the reference signal is tracked without steady-state errors and extends the control strategy to

$$u(t) = -Kx_{\text{ctrl}}(t) + Hx_m^*(t) + k_I \int x_m^*(t) - x_m(t)dt, \quad (3.58)$$

where  $k_I$  is the integral gain, which should be chosen relatively low to not interfere with the stabilizing controller during transients that can occur due to external disturbances on the mover position. The resulting values for the control matrices and constants are listed in **Tab. 3.3**.

### 3.5.3 Inverter Stage

So far, it has been assumed that the current in the EMs is readily available and can be directly adjusted by the position controller and active tilting damper. However, in reality, a voltage  $U$  must be first applied to the EMs' terminals that together with the resistance  $R_{\text{EM}}$  and inductance  $L_{\text{EM}}$  determines the transient behavior and steady-state value  $I$  of the current. Therefore, a current controller that dynamically sets the proper voltage depending on a reference current value  $I^*(t) = u(t)$  coming from the position controller and active tilting damper has to be designed. This can be achieved with a cascaded structure as shown in **Fig. 3.9**, where it must be ensured that the bandwidth of the inner current loop is sufficiently higher (e.g., ten times larger) than the bandwidth of the position controller and active tilting damper so that the dynamics of the current control must not be considered during the design of the position controller and active tilting damper, for which we assume  $I(t) = I^*(t)$ . In the simplest case, the voltage applied to the EMs is the average value of a switched voltage generated with an inverter block (e.g., a full-bridge inverter) that allows generating positive ( $+U_{\text{DC}}$ ) and negative ( $-U_{\text{DC}}$ ) voltages out of a constant voltage source  $U_{\text{DC}}$  as indicated in **Fig. 3.1**. However, due to the large  $dv/dt$  that modern power semiconductors can generate while switching, a filter at the output of the inverter stage is required.

Without the filter, the high-frequency components of the switched voltage ( $U_{inv}$  in **Fig. 3.10**) would drive a high-frequency current  $i_{HF}$ , which finds a low impedance path through the parasitic capacitance of the EM. The return path for this current is via the EM cables, modeled by the impedance  $Z_{g,inv}$ , and via the ground connection of the position measurement circuit, modeled with the impedance  $Z_{g,meas}$ , which includes the aluminum body of the force sensor, the conductive shield of the force sensor's cables, and the reference potential for the measurements. Due to their close placement, the position measurement circuit is coupled with the parasitic capacitance  $C_c$  to the corresponding EM and is tied to the common ground on the inverter. Furthermore, the time-varying common-mode voltage  $u_{CM}(t) = (u_{DS,1}(t) + u_{DS,2}(t))/2$  induces a common-mode current  $i_{CM}$  in the cables of the EM that charges and discharges the coupling capacitance  $C_c$ , see **Fig. 3.10**. Both currents,  $i_{HF,2}$  and  $i_{CM}$ , can generate an error in the position measurement since the analog voltage, which is then sampled by an ADC, is not only determined by the amplifier circuit modeled by the gain  $k_{VGA}$ , but also by an error voltage, i.e.,  $u_{amp}(t) = k_{VGA} \cdot u_{sens}(t) + Z_{g,meas} \cdot (i_{HF,2}(t) + i_{CM}(t))$ . To minimize these noise issues, we employ a passively damped LC filter that reduces the amplitude of the high-frequency current flowing through the EMs that eventually reaches the position measurement circuit because of their close placement within the MLP by offering a low impedance return path via the filter capacitors  $C_f$  and  $C_{fd}$ . We furthermore add a common-mode choke that increases the common-mode impedance of the load at the output of the inverter to reduce

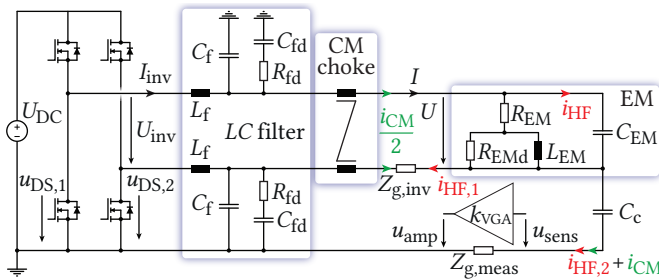


**Fig. 3.10:** Electrical system consisting of a full-bridge inverter that drives the EM of an axis. The passively damped LC filter is inserted to reduce the disturbance  $i_{HF,2}$  that can affect the position measurement circuitry due to coupling denoted by  $C_c$  with the EM, which is modeled by four lumped elements. Similarly, the common-mode choke helps reduce the amplitude of the high-frequency common-mode current  $i_{CM}$ .

the amplitude of the common-mode current. For the design of the filter, we follow the commonly used guidelines described in the literature [75] to optimally dampen the filter and avoid resonances with the driving converter. The first consideration is to get a large high-frequency attenuation ( $> 40$  dB) at the switching frequency  $f_{sw}$  reported in **Tab. 3.2**, meaning that the design frequency given as

$$f_{0,LC} = \frac{1}{2\pi \cdot \sqrt{L_f C_f}}, \quad (3.59)$$

has to be at least ten times lower than the switching frequency since the filter's roll-off is  $-40$  dB/dec. Second, for strong resonance damping, a large ratio

$$n = \frac{C_{fd}}{C_f} \quad (3.60)$$

is favorable in combination with the optimally designed damping resistor calculated from [76] as

$$R_{fd} = \sqrt{\frac{L_f}{C_f}} \cdot \frac{n+1}{n} \cdot \sqrt{\frac{2(n+1)(n+4)}{(n+2)(3n+4)}}. \quad (3.61)$$

Regarding the controller design, the proportional and integral gains of a PI-controller are calculated with the MATLAB® function “pidTuner” where

**Tab. 3.2:** Parameters of the inverter, LC filter, and EM equivalent circuit shown in **Fig. 3.10**.

Inverter			
$U_{DC}$	40 V	$f_{sw}$	100 kHz
LC filter			
$L_f$	22 $\mu$ H	$R_{fd}$	1 $\Omega$
$C_f$	22 $\mu$ F	$C_{fd}$	88 $\mu$ F
$f_{0,LC}$	7.2 kHz	$n$	4
Electromagnet			
$L_{EM}$	18.6 mH	$R_{EM}$	5.5 $\Omega$
$C_{EM}$	87 pF	$R_{EMd}$	85 k $\Omega$
Resonant freq.	125 kHz		

the closed-loop bandwidth  $\omega_{in}$  given in **Tab. 3.3** of the inner current control loop is selected according to the transfer function of the designed filter from inverter voltage to the inverter current  $G_{el}(s) = I_{inv}(s)/U_{inv}(s)$ . As indicated in **Fig. 3.9**, a filter  $G_{filt}(s)$  on the feedback path of the inner current controller is used to approximate better the current in the EM  $I(s) = G_{LC,EM}(s) \cdot U_{inv}(s)$  from the measured current  $I_{inv}(s)$ . To minimize the phase shift, its cutoff frequency should be larger than the wanted bandwidth  $\omega_{in}$ . For the controller design, the filter for the current is included in the open-loop transfer function  $G_{el}(s) \cdot G_{filt}(s)$ , and care is taken especially for achieving a sufficient phase margin that avoids overshoots in the EMs' current.

As additional notes, the minimum required DC voltage of the inverter depends on the required control bandwidth  $\omega_{in}$  and on the current amplitude  $\hat{I}$  that has to be driven to counteract displacements of the mover, where the relation  $\hat{I} = k_{FPM}/k_{FEM} \cdot x_m$  holds. For the selected  $\omega_{in} = 2\pi \cdot 20$  Hz and current amplitude  $\hat{I} = 4.5$  A corresponding to  $x_m = 10$  mm, a minimum  $dI/dt = \hat{I} \cdot \omega_{in} = 571.8$  A/s is calculated, and must be achieved to get the desired dynamics of the current. This is related to the DC voltage applied to the EM, i.e.,  $U_{DC,min1} = L_{EM} \cdot dI/dt = 10.6$  V, assuming a purely inductive EM (see **Fig. 3.10** and **Tab. 3.2**). To finally achieve the maximum value  $\hat{I}$  of the current at steady-state, a minimum DC voltage  $U_{DC,min2} = R_{EM} \cdot \hat{I} = 25$  V must be available at the EM's terminals. Further, the switching frequency should be chosen to maximize the efficiency of the inverter considering the switching and conduction losses of the power transistors during operation and has no impact on the operation of the MLP as long as it is ten times higher (as a rule of thumb) than the largest bandwidth in the system  $\omega_{in}$ , otherwise, a proper current control cannot be achieved. The selected inverter voltage and switching frequency listed in **Tab. 3.2** satisfy these requirements.

### 3.5.4 Position Sensor Offset Compensation

In cases where the measured or observed mover's position signal has a constant or slowly fluctuating offset, e.g., due to temperature dependencies, the proposed controller would position the mover with a deviation of the reference position. Therefore, an outer current control loop (see **Fig. 3.9**) is required to compensate for this offset. When the mover reference position is zero, the EM's current should also be zero since there are no radial magnetic forces that destabilize the mover. Otherwise, a control mechanism should drive the current to zero by setting a reference position for the mover that eliminates the position offset. This is done with a slow integral controller that

adjusts the mover's position reference so that the error between the reference current  $I_{\text{final}}^*$  at the desired mover's position and the measured current is zero. This works for any desired mover's position since the required current that compensates for the radial magnetic force is known (either measured or calculated with a model). In the linearized model of **Subsection 3.3.1**, for the design of the controller gains, a plant with a constant relation between the mover's reference position and the current flowing in the EMs

$$\frac{I(s)}{x_m^*(s)} = -\frac{k_{\text{FPM}}}{k_{\text{FEM}}} \quad (3.62)$$

can be considered with the requirement that the outer current controller's bandwidth is much lower than the dynamics of the position controller. Please note that the negative sign in (3.62) originates from the fact that a negative current must be generated to compensate a positive magnetic force observed for a positive radial position. To fulfill the mentioned prerequisite, the integral controller is designed such that the closed-loop bandwidth  $\omega_{\text{out}}$  results as significantly lower (e.g., ten times lower) than the lowest bandwidth in the system (see **Tab. 3.3**), i.e., the closed-loop bandwidth of the mover displacement, leading to

$$G_{\text{L,out}}(s) = -\frac{k_{\text{FEM}}}{k_{\text{FPM}}} \cdot \frac{\omega_{\text{out}}}{s}. \quad (3.63)$$

The closed-loop transfer function shows a typical first-order low-pass filter behavior with cutoff frequency (bandwidth)  $\omega_{\text{out}}$

$$G_{\text{CL,out}}(s) = \frac{I(s)}{I_{\text{final}}^*(s)} = \frac{1}{1 + s/\omega_{\text{out}}}. \quad (3.64)$$

With this design and the constraint on the bandwidth, there are no concerns about the phase margin and eventual dynamic overshoots since the assumed plant (3.62) is characterized by a constant value, and with an integral controller, the phase margin is at least  $-90^\circ$ . However, when the bandwidth of the outer loop has to be increased for a faster dynamic application, care must be taken in the model of the plant (3.62) and the corresponding controller design by considering the dynamics of the position controller and eventually the response of the inner current loop.

Furthermore, even with the proposed offset compensation for the position sensor, a positioning error that originates from an offset in the current measurement can still exist. Considering an error due to a constant offset in the position sensor  $x_{\text{err,pos}}$  and a position error due to a constant offset in the



current sensor  $x_{\text{err,curr}} = k_{\text{FEM}}/k_{\text{FPM}} \cdot I_{\text{err}}$ , the current error that leads to the same position error can be found as  $I_{\text{err}} = x_{\text{err,pos}} \cdot k_{\text{FPM}}/k_{\text{FEM}}$ . Considering the case at hand and assuming that the position error is  $x_{\text{err,pos}} = 1$  mm, the equivalent error of the current sensor would be  $I_{\text{err}} = 0.5$  A, therefore, an outer control loop is beneficial because most commercial sensors with current ratings being orders of magnitude larger than  $I_{\text{err}}$  are more accurate. The used shunt resistor-based current sensor achieves an accuracy of 60 mA with a measuring range of 10 A, i.e., 0.6 % accuracy.

## 3.6 Hardware Demonstrator Realization

This section provides a detailed practical investigation of a MLP hardware demonstrator equipped with a (reaction) force sensor for the mover's position sensing that proves the effectiveness of the previously discussed model, observer, and controller design. The properties of the passive part of the MLP, resulting from the design of the PMs according to **Chapter 2** and determining the mover's levitation height, and most importantly, the radial destabilizing force that has to be counteracted by the EMs, have been discussed in **Section 3.2**. The design and optimization of the EMs is equally important since they define the final size of the MLP and the power consumption for achieving a stable levitation, i.e., the copper loss per unit of radial displacement and unit of height. The dimensions of the EMs are chosen so that a preferably large controllable range in the radial direction of the mover is possible while trying to maintain the dimensions of the overall MLP as restricted as possible, while in addition trying to maximize the force generation with the smallest possible amount of current (i.e., power losses of the EMs). For more details, see **Appendix A**. Each of the four employed EMs (two for each radial axis) is driven with a corresponding full-bridge power electronics inverter (see **Fig. 3.10**) with  $U_{\text{DC}} = 40$  V and a maximum output current of  $I_{\text{max}} = 6$  A that provides the required voltage to the EM's terminals, which is calculated using a SoC featuring a CPU (where the observer and controller are implemented) and an FPGA that provides the gate signals to the power transistors of the inverters and records the signals from the force sensor.

### 3.6.1 Force Sensor

The device used to sense the mover position in the MLP featuring extreme levitation heights is a force sensor. It is composed of a three-axis ( $x, y, z$ ) strain gauge load cell [77] rated for a maximum force of 100 N on each axis.

Theoretically, only two axes  $x$ ,  $y$  would be necessary to regulate the mover's radial position. However, the additional sensing axis  $z$  is required for future applications, not discussed in this chapter, where the mover is loaded with a payload, and the levitation height can be determined by measuring the system's total weight. Consequently, a force sensor with a notably high maximum force rating (100 N) was selected. This sensor is perpetually subjected to a load of 35.3 N due to the mass of the stator  $m_{mlp}$  (refer to **Tab. 3.1** for numerical values). As a result, a margin of 64.7 N is available to accommodate both inertial forces and any additional payload. The force sensor provides an electrical signal of 1 mV/V at the rated force, meaning that for the chosen excitation voltage of 3 V applied to the strain gauges, a maximum signal of 3 mV can be measured at the sensing terminals. For a displacement of the mover by 1 mm from the center, the magnetic force that has to be sensed is 0.03 N, which corresponds to a voltage difference of 0.94  $\mu$ V. Accordingly, an amplifier featuring very low noise levels is required to get a signal measurable with an analog-to-digital converter (ADC). The amplifier circuit depicted in **Fig. 3.11** consists of a buffered very low noise constant voltage reference (LTC6655 [78]) used to excite the strain gauges, which are arranged as a Wheatstone bridge for each axis, and three variable gain amplifiers (VGA) [66] that amplify and filter the differential signal coming from the gauges bridges. The cutoff frequency can be set with an external capacitor

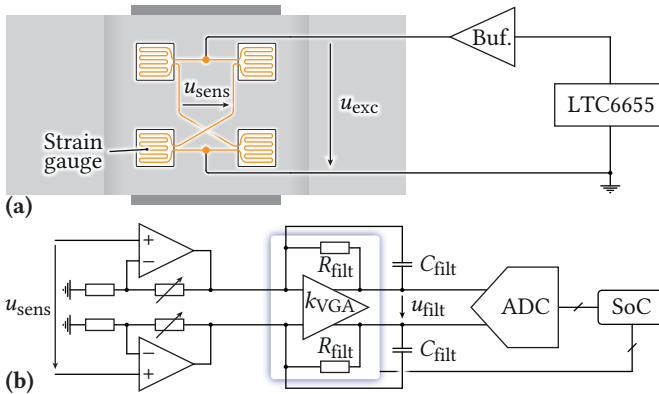


**Fig. 3.11:** (a) Excitation of the strain gauges, glued to the force sensor for a single axis, with a buffered constant voltage reference. (b) Schematic circuit diagram of the force sensor amplifier for a single axis, constituted by a manual offset correction stage, a variable gain amplification, and an analog-to-digital conversion.

$C_{\text{filt}} = 440 \text{ nF}$  that builds a first-order low pass filter with the internal feedback resistor  $R_{\text{filt}} = 9.5 \text{ k}\Omega$ . The voltage gain can be dynamically tuned from the SoC for applications where the mover changes levitation height (due to different payloads). In these cases, the amplification has to be changed to avoid saturating the VGAs' outputs since larger radial  $x, y$  forces, i.e., signals, are observed when the mover approaches the stator. Before the amplification, a manual offset compensation is implemented and is required to set the force sensor output signal to zero when the forces acting on the force sensor are zero, as the strain gauges forming a Wheatstone bridge could have slightly different resistances that would already cause a saturation of the output due to the large VGA's gain. Finally, the amplified and filtered analog signals are digitized by a multi-channel ADC [79] communicating with the SoC. It should be noted that, for static applications, the implemented amplifier enables measuring forces with a resolution of  $2.3 \text{ mN}$ , which translates to a limit of the positional accuracy of around  $74 \text{ }\mu\text{m}$  for the investigated MLP.

### 3.6.2 Controller Tuning

With the correctly estimated quantities  $(x_m, \dot{x}_m, \theta_m, \dot{\theta}_m)$  that describe the mover's motion, a state-space controller as described in **Subsection 3.5.2** is implemented for both axes  $x$  and  $y$ , in the same way, since it only depends on mover's parameters that are equal for  $x$  and  $y$  axes due to symmetry. For this purpose, the choice of the weighting matrix  $Q$  and the constant  $R$  for the LQR controller tuning has been carried out so that the mover's rotation (tilting) around the  $x$  and  $y$  axis is strongly damped choosing a relatively large  $Q_{(1,1)}$  constant, leading to a reasonable closed-loop pole's distribution. Indeed, with

$$Q = \begin{bmatrix} 0.129 & 0 & 0 & 0 \\ 0 & 0.002 & 0 & 0 \\ 0 & 0 & 0.002 & 0 \\ 0 & 0 & 0 & 0.002 \end{bmatrix} \quad (3.65)$$

$$R = 1 \quad (3.66)$$

all poles of the closed-loop transfer function (i.e., the eigenvalues of the matrix  $A_{\text{ctrl}} - B_{\text{ctrl}} \cdot K$ ) lie on the negative real axis between  $0.52 \text{ Hz}$  and  $3.29 \text{ Hz}$  as indicated in the  $s$ -plane shown in **Fig. 3.5** with violet crosses and reported in **Tab. 3.3** as  $p_1, p_2, p_3,$  and  $p_4$ . Further, the integral gain that completes the mover's position and rotation control law (3.58) is chosen to be equal to one-tenth of the smallest pole in the stabilized system (to not interfere with the stabilizing controller component), i.e.,  $k_I = 2\pi \cdot 0.15 \text{ A/ms}$ . Additionally,

**Tab. 3.3:** Parameters of the outer current controller, position and active rotation damping controller, and inner current controller.

Outer current controller $G_{I,\text{out}}$			
$\omega_{\text{out}}$		$2\pi \cdot 0.05 \text{ Hz}$	
Position controller (3.50)			
$k_1$	$-0.04 \text{ As}/^\circ$	$k_2$	$-4.3 \text{ A}/^\circ$
$k_3$	$283.5 \text{ As/m}$	$k_4$	$3.09 \text{ kA/m}$
$H$	$536.8 \text{ A/m}$	$k_1$	$2\pi \cdot 0.15 \text{ A/ms}$
$p_1$	$2\pi \cdot 0.52 \text{ Hz}$	$p_2$	$2\pi \cdot 3.29 \text{ Hz}$
$p_3$	$2\pi \cdot 3.18 \text{ Hz}$	$p_4$	$2\pi \cdot 1.74 \text{ Hz}$
Inner current controller $G_{PI,\text{in}}$			
$\omega_{\text{in}}$		$2\pi \cdot 20 \text{ Hz}$	

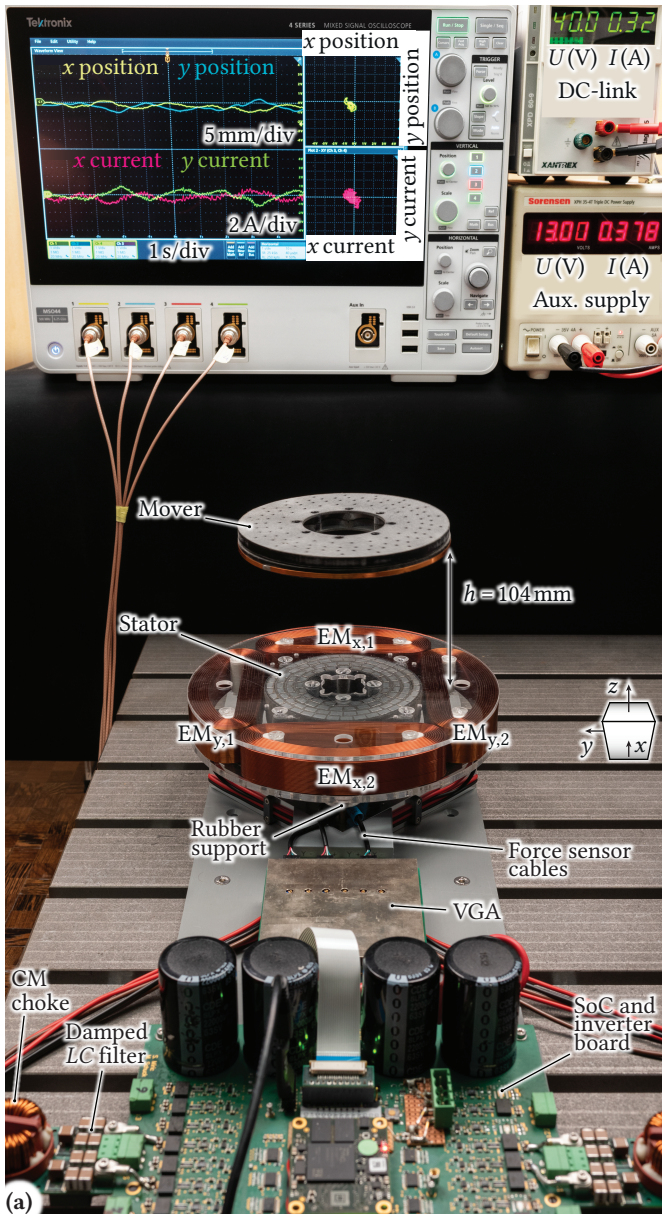
the  $LC$  filters for the inverter outputs (see **Fig. 3.10**) are designed taking into consideration the volume of the passive components and the design guidelines introduced in **Subsection 3.5.3**, leading to the values listed in **Tab. 3.2**. The design frequency is  $f_{0,\text{LC}} = 7.2 \text{ kHz}$  and leads to an attenuation of 46 dB on the EM voltage at the switching frequency (100 kHz). The impact of the output filter on the EM current dynamics is very small as the impedance of the capacitors is at least 10 times larger than the one of EM coils within the current control bandwidth of  $\omega_{\text{in}} = 2\pi \cdot 20 \text{ Hz}$ . The bandwidth  $\omega_{\text{in}}$  has been chosen to be as low as possible (i.e., about ten times higher than the highest frequency pole of the position controller) in order not to trigger vibrations of the mechanical structure since the output signal of the force sensor could be heavily disturbed with oscillations around 130 Hz (see **Subsection 3.4.2**). A measure that has been proven to work with a higher current loop bandwidth (e.g., 100 Hz) is a moving average filter on the current reference signal calculated by the position controller and active tilting damper. The number of data points considered for the average is chosen to eliminate current components that would trigger a vibration of the structure. Due to relatively large noise on the force sensor signals and their slowly fluctuating offset, an outer current controller that drives the current to zero so that the mover is centered is implemented following **Subsection 3.5.4** with a closed-loop bandwidth of  $\omega_{\text{out}} = 2\pi \cdot 0.05 \text{ Hz}$ . The reported implementation works well for both axes,

i.e., the mover never experiences rotary (tilting) oscillations, and its radial  $x, y$  position is stabilized.

### 3.6.3 Results

The demonstration of the stable levitation is depicted in **Fig. 3.12**, where the mover is levitated with an air gap of 104 mm above the stator. The calculated standard deviation of the position recorded over ten seconds during the course of levitation is 1.3 mm for the  $x$  position and 1.6 mm for the  $y$  position, indicating that the mover experiences a certain deviation from the center and that the performance on both axes is similar. Furthermore, the effect of the controller that eliminates the force sensor's offset is visible, comparing the mean values of the mover's position and EMs' currents in the  $x y$  plot in the oscilloscope and in **Fig. 3.12 (b)** and **(c)**. The first is  $(x_m, y_m) \approx (-2.2 \text{ mm}, -2.2 \text{ mm})$  also depicted in **Fig. 3.12 (b)**. The second is  $(I_x, I_y) \approx (-0.6 \text{ A}, -0.1 \text{ A})$  also depicted in **Fig. 3.12 (c)**. Therefore, even though the observer calculates a position with an offset originating from the force sensor, the mover will be controlled in the center's vicinity where the magnetic forces and, hence, the mean values of the control currents are zero.

### 3.6. Hardware Demonstrator Realization



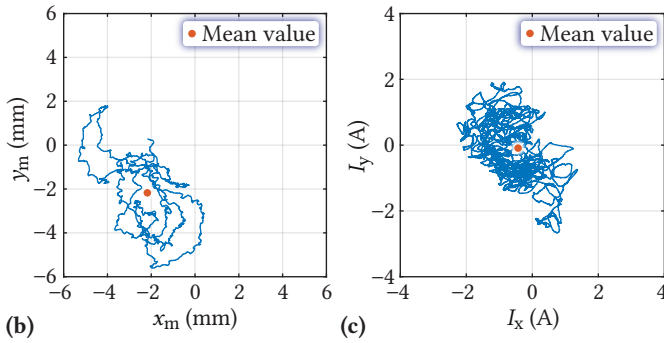


**Fig. 3.12:** (a) Picture of the complete system showing the mover's stable levitation above the stator with 104 mm air gap. The force sensor is not visible because it is placed underneath the stator and is connected to the VGA that amplifies and filters the force-dependent signals and delivers them to the observer implemented on the SoC. The DC-link supply is used for the EMs, whereas the auxiliary supply provides power to the SoC and the force sensor. (b) and (c) show the 2D plots of the observed mover's position and control current, respectively, which are also found in (a) on the oscilloscope with a different scaling factor.

### 3.7 Conclusions

This chapter presents a novel method for sensing the position of the mover in a magnetic levitation platform (MLP), where a force sensor is used to detect the reaction forces on the stator. The force sensor enables the operation of the MLP in situations where the mover is encapsulated in a hermetically sealed chamber and levitated with an extreme air gap. An observer extracts the mover's radial position and angle from the measured forces, which also depend on the control actions to achieve closed-loop position control of the mover. For this purpose, a dynamic model of the MLP, including the force sensor, is developed and accordingly augmented to compensate for unwanted disturbances with a calibration procedure. Finally, based on the developed model, a state-space controller allows controlling the mover's position and actively dampens eventual rotary (tilting) oscillations around the  $x$  or  $y$  axis.

With the proposed methods, a stable levitation of the mover is achieved, where the air gap is 104 mm, the characteristic dimension is  $CD = 207$  mm, and the passive radial stiffness of the MLP is  $32.8$  N/m. The performance is evaluated during centered ( $x_m^* = y_m^* = 0$ ) steady-state levitation by calculating the standard deviation of the mover's position, which results in

$(\sigma(x_m), \sigma(y_m)) = (1.3 \text{ mm}, 1.6 \text{ mm})$ .

In the course of further research, eddy current measurements will be used alternatively for determining the mover's position, and a comparative evaluation of the position control performance of both concepts will be provided.



# 4

## Comparative Analysis of Force and Eddy Current Position Sensing Approaches for Magnetic Levitation Platform with an Exceptional Hovering Distance

This chapter summarizes the most relevant findings of the comparison between two sensors, the reaction force sensor and the eddy current sensor, used for closed-loop control of magnetic levitation platforms that are also published in:

- ▶ R. Bonetti, S. Mirić, and J. W. Kolar, “Comparative Analysis of Force and Eddy Current Position Sensing Approaches for Magnetic Levitation Platform with an Exceptional Hovering Distance,” *Actuators*, vol. 13(4), no. 122, pp. 1-22, March 2024.

### Chapter Abstract

This chapter provides a comparative analysis between a force sensor and an eddy current sensor, focusing on their usability to determine the position of a circular levitating permanent magnet (PM) mover within an axially symmetric magnetic levitation platform (MLP) with an exceptionally large air gap. The sensors enable closed-loop control, which is essential for accurately and stably maintaining the mover's radial position. For the considered MLP, a change in radial position in principle results in a tilting of the mover, i.e., a deviation from the parallel alignment relative to the stator. As both the radial position and the tilting angle affect the sensors' (force and eddy current) output voltage, an observer must deduce the radial position from the output sensor's voltage, requiring a comprehensive MLP dynamic model and calibration of the models for both sensing approaches. The chapter discusses the advantages and weaknesses of each sensor concept, exploring operational principles and performance in levitation tests. The force sensor exhibits versatility, proving functional across various application scenarios, such as when the mover is sealed in a conductive, non-magnetic chamber. In contrast, due to its high-frequency operation, the eddy current sensor is more straightforward to characterize, simplifying its behavior relative to the mover's slower dynamics. Measurements are conducted to validate the models, showing the eddy current sensor's robustness against disturbances and imperfections in the MLPs and its immunity to cross-axis interference. Conclusively, in levitation experiments where the mover is vertically distanced at 104 mm from the stator, the eddy current sensor achieves a position tracking precision about ten times better and a ten times higher signal-to-noise ratio (SNR) compared to the off-the-shelf force sensor, confirming its better performance and reliability, but it cannot be used in applications where conductive objects are present in the air gap. Furthermore, additional experiments are conducted on the MLP using the eddy current sensor to show the controller's robustness and dynamic reference tracking capability, with and without a payload.

## 4.1 Introduction

Magnetic levitation finds applications in various fields such as transportation, aerospace, civil, biomedical, chemical, architectural, and automotive engineering, as detailed in [80]. Within this extensive range of applications, magnetic levitation platforms (MLPs), which are characterized by the absence of mechanical contact between the levitated platform (mover) and the steady base (stator), serve as vibration isolation systems for high-precision manufacturing [81, 82], dynamic supporting structures for mirrors in optical pointing and scanning applications [83], and zero-power gravity compensation systems [84], e.g., nanometer-scale positioning [85], ground-based

testing of large optical equipment for space use [86], and cleanroom conveyor systems [87].

The theoretical and practical implementation of an axially symmetric MLP potentially suitable for zero-power gravity compensation applications has been analyzed in **Chapter 2** and **Chapter 3** with the aim of extending the vertical air gap (i.e., the levitation height  $h$  in **Fig. 4.1**) between the stator and mover. Similar systems based on commercially available levitation modules have been sporadically analyzed in the literature regarding structural optimizations and closed-loop control [48, 49, 88–91].

Such MLPs are formed by a hybrid structure of permanent magnets (PMs) and electromagnets (EMs), which constitute the passive and the active part of the system, respectively. Stator and mover PMs generate the vertical force that compensates for gravity. EMs only generate the stabilizing forces that hold the mover at the zero-power point, i.e., the radially centered position  $x = y = 0$ , resulting in lower volume and losses. The PMs are designed so that the mover has three passively stable degrees of freedom (DOFs), achievable with the axially symmetric geometry presented (see **Fig. 4.1**). Specifically, the axial ( $z$  direction) displacement and the two rotations around the radial axes  $x, y$  are stable due to restoring magnetic forces and torques. The radial ( $x, y$  direction) displacement is passively unstable due to magnetic forces that pull the mover away from the center  $x = y = 0$ . Therefore, an active control of these two DOFs is strictly necessary. The axial symmetry of both PMs contributes to marginal stability in rotation around the  $z$  axis. This means there is no strict need for active control to manage this rotation; therefore, this chapter does not address it.

The adoption of closed-loop control is essential to stabilize the mover's unstable radial positions, denoted by  $x_m$  and  $y_m$ . This necessitates an effective method for obtaining the position of the MLP's mover, especially in scenarios demanding high versatility, such as, e.g., operation within stainless-steel (non-magnetic) process chambers where traditional optical position sensing is infeasible. Consequently, **Chapter 3** introduces a novel position measurement methodology that relies on observing the reaction forces exerted on the stator by the mover's movements, called *reaction-force-based* position sensor (RFS). This approach is notably beneficial for facilitating the automated manufacturing and manipulation of objects, enabling robot arms to seamlessly navigate through the air gap between the stator and the mover. However, the accurate implementation of an RFS necessitates meticulous modeling of the MLP's dynamics to convert reaction forces into position data precisely. While the complexity and noise inherent in the force sensor may impact

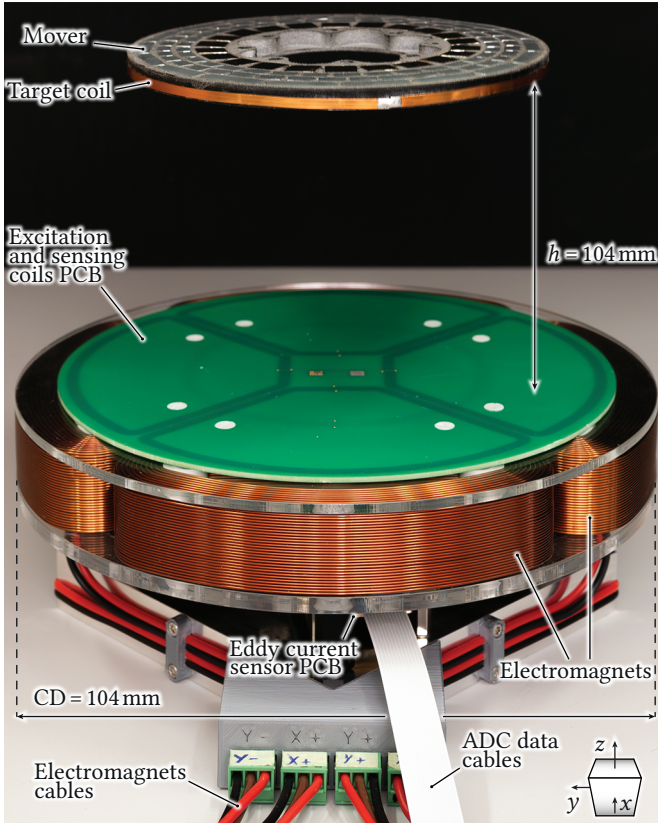


**Fig. 4.1:** Magnetic levitation platform (MLP) with the mover levitating using the eddy current position sensor (ECS) for determining the radial ( $x$ ,  $y$  axis) position. The permanent magnet (PM) stator, which is not visible as it is covered by the excitation and sensing PCB coils, generates axial, i.e.,  $z$  direction, magnetic forces that maintain the mover at the reported distance of  $h = 104$  mm. The electromagnets compensate for magnetic destabilizing forces in the radial  $x$ ,  $y$  plane and maintain the mover at the desired position based on continuous measurements captured by the position sensor.

the precision of the RFS method, the technique's universal applicability and ability to accommodate conductive objects within the air gap stand out. This is a considerable advantage over other types of position sensors, such as eddy-current-based sensors (ECSs), which require an air gap without any conductive materials. Hence, the objective of this chapter is to meticulously

evaluate the RFS and ECS technologies, focusing on their applicability, the complexity of implementation and modeling, accuracy, stability, and reference tracking capabilities. Such a detailed comparison is critical when selecting the most appropriate sensor type for specific applications, easing decision-making in the integration process of advanced mechatronics.

In **Section 4.2**, we introduce the geometry and display the operating principles of the ECS. A brief repetition of the operating principles of the RFS, which are extensively discussed in **Chapter 3**, is given in **Section 4.3**. The position sensor's dynamics modeling and verification is covered in **Section 4.4**. The comparative results of steady-state levitation experiments for both sensors are presented in **Section 4.5**, where we clarify that there are more restrictions in the design of an RFS-based position control, such as a more sophisticated dynamical model requirement and lower signal-to-noise ratio compared to the ECS. However, the ECS cannot be used in applications when the mover is enclosed in a conductive chamber due to Faraday's cage effect. Furthermore, in **Section 4.6**, additional tests on the MLP using only the ECS demonstrate that dynamical reference tracking and loading the mover with extra weight are possible. Finally, conclusions summarizing the main findings are drawn in **Section 4.7**.

## 4.2 Eddy Current Position Sensor for the MLPs

This section first introduces the ECS, tailored explicitly for the analyzed MLP. Next, the main properties of the RFS concept proposed in **Chapter 3** are summarized in **Section 4.3**, and a detailed comparison of the two position-sensing technologies is finally performed starting from **Section 4.4**.

### 4.2.1 ECS Geometry and Operating Principle

The ECS applied to the MLP employs high-frequency electromagnetic signals to determine the position of the mover in space. A set of four coils is used to sense the radial  $x, y$  position and is arranged as depicted in **Fig. 4.2 (a)** and **(b)**. The excitation coil is radially centered and located directly above the stator (see **Fig. 4.2 (a)**). A time-varying voltage  $u_{\text{exc,ECS}}$  with a high-frequency  $f_{\text{exc}}$  is applied at its terminals (see **Fig. 4.3 (a)**), whose current generates a high-frequency magnetic field that reaches and couples with the target coil on the mover.

#### 4.2. Eddy Current Position Sensor for the MLPs

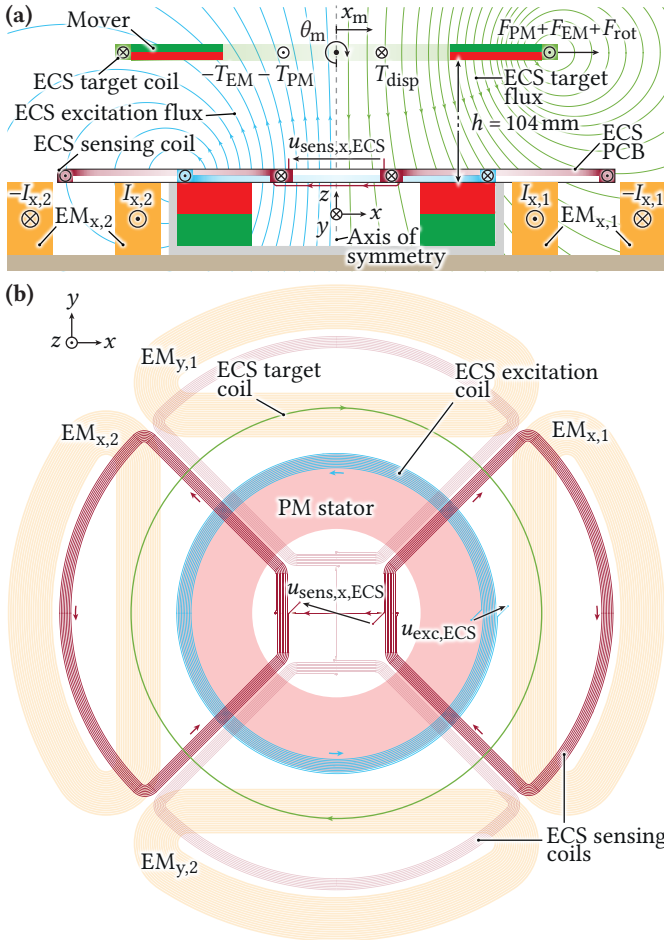


**Fig. 4.2:** (a) Section view of the MLP that uses the ECS, where the direction of the magnetic flux density, induced currents, and voltages is shown for a positive excitation current. The directions of the shown electromagnetic force  $F_{EM}$  and torque  $T_{EM}$  are given by a positive current injected in the EMs when the mover is at its natural levitation point  $x_m = 0$  and  $\theta_m = 0$ . Additionally, the effects of displacements  $x_m$  and  $\theta_m$  are shown, leading to the displacement-dependent magnetic force  $F_{PM}$  (unstable) and torque  $T_{disp}$ , and the rotation-dependent magnetic torque  $T_{PM}$  (stable) and force  $F_{rot}$ . (b) Top view of the system (excluding the radially centered mover) that shows the spatial distribution of the sensor's coils with respect to the stator and EMs.

The mover is equipped with a short-circuited target coil, where an eddy current flows to counteract the coupled excitation flux (Faraday’s law of induction), generating a magnetic field with the same frequency as the excitation frequency (denoted as “ECS target flux” in Fig. 4.2 (a)). Two sensing coils per axis are connected in anti-series to couple the flux from the excitation and target coil, generating a proportional voltage  $u_{\text{sens,ECS}}$  at their open terminals. Examining the sensing coils (e.g., the one for position measurement along the  $x$  axis) closely, the voltage generated by the excitation coil’s magnetic field is zero due to the anti-series connection of the sensing coils and the equal coupling of excitation flux (a radially symmetric magnetic field does not induce any sensing voltage). The same applies to the field from the target coil when the mover is radially centered and horizontal. As the mover displaces from the center (e.g., in positive  $x$  direction), the  $x$  axis sensing coil outputs a time-varying voltage with frequency  $f_{\text{exc}}$  as illustrated in Fig. 4.3 (b) because of an imbalance in the coupled target flux between the two sides of the coil. When the sensed signal is demodulated to obtain the amplitude  $\hat{u}_{\text{sens,ECS}}$ , a linear relation between the mover’s displacement and sensed voltage valid for small displacements is observed, i.e.,  $\hat{u}_{\text{sens,ECS}} = -k_{v,\text{disp}} \cdot x_m$ , where  $k_{v,\text{disp}}$  is the sensitivity for the radial displacement and is given in Tab. 4.1. As already observed in Section 3.3 for the reaction force sensor, the tilting of the mover

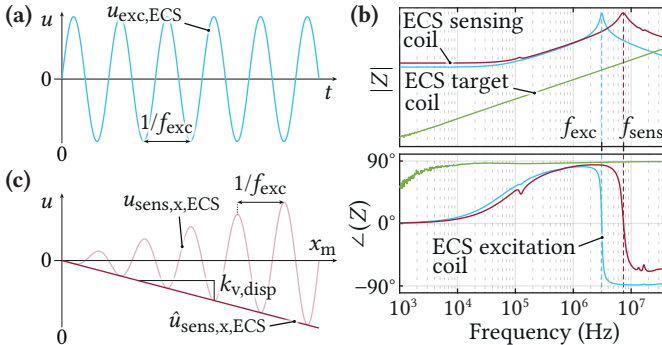


**Fig. 4.3:** (a) High-frequency excitation voltage for the excitation coil. (b) Expected voltage output from the sensing coil  $u_{\text{sens,ECS}}$  and demodulated voltage signal  $\hat{u}_{\text{sens,ECS}}$  for a positive mover’s displacement in  $x$  direction. (c) Impedance measurements of the proposed sensor’s coils, where the target and sensing coils operate in the inductive region at the excitation frequency  $f_{\text{exc}} = 3.1$  MHz, indicating that magnetic coupling exists.

around the radial  $x, y$  axes influences the sensed voltage. Tilting the mover while keeping it radially centered, a linear relation valid for small angles is observed and written as  $\hat{u}_{\text{sens,ECS}} = -k_{v,\text{rot}} \cdot \theta_m$ , where  $k_{v,\text{rot}}$  is the sensitivity for the rotation. Considering both, the displacement and the rotation, which always happen simultaneously **Section 3.3** during destabilization and control action, the superimposed equation

$$\hat{u}_{\text{sens,ECS}} = -k_{v,\text{disp}} \cdot x_m - k_{v,\text{rot}} \cdot \theta_m \quad (4.1)$$

fully describes the mover's position in space for small displacements and angles.

**Tab. 4.1:** ECS parameters, where the values of the  $RLC$  components are extracted from the impedance measurement depicted in **Fig. 4.3 (c)** performed with the coils installed on the MLP. Due to symmetry, only the  $x$  axis sensing coil parameters are shown.

$k_{v,\text{disp}}$	51.3 $\mu\text{V}/\text{mm}$	$k_{v,\text{rot}}$	5 $\mu\text{V}/^\circ$
$k_{\text{IPS}}$	240 $\text{V}/\text{V}$	$T_{f,\text{ECS}}$	4.6 ms
$f_{f,\text{ECS}}$	35 Hz	$u_{\text{exc,ECS}}$	7.4 $\text{V}_{\text{pp}}$
$f_{\text{exc}}$	3.1 MHz	$f_{\text{sens}}$	7.6 MHz
$R_{\text{exc}}$	9.5 $\Omega$	$L_{\text{exc}}$	23.9 $\mu\text{H}$
$R_{\text{sens}}$	15 $\Omega$	$L_{\text{sens}}$	27.2 $\mu\text{H}$
$R_{\text{target}}$	2 $\text{m}\Omega$	$L_{\text{target}}$	0.4 $\mu\text{H}$
$C_{\text{exc}}$	110 pF	$C_{\text{sens}}$	16 pF
$N_{\text{exc}}$	10	$N_{\text{sens}}$	16

### 4.2.2 ECS Design Considerations

For the design of the ECS coils, the spatial distribution and the number of turns are important metrics because they primarily determine the coils' inductance and parasitic capacitance, ultimately defining the resonant frequency. The goal is to maximize the sensitivity  $k_{v,\text{disp}}$  and keep the inductive behavior and the overall MLP's size the same in order to facilitate a fair comparison with the RFS. The outermost winding of the excitation coil is chosen as large as possible



to maximize coupling with the target coil on the mover. However, the size is limited by the placement of the PM stator and EMs because the excitation coil's magnetic field induces eddy currents in neighboring conductive materials, affecting the coupling with the target coil. The distribution of eddy currents in a conductive material is determined by the skin depth  $\delta = \sqrt{\rho / \pi f_{exc} \mu_0 \mu_r}$ , which depends on its electrical resistivity  $\rho$  and relative permeability  $\mu_r$  [92]. Copper EMs have a much lower resistivity than NdFeB PMs ( $\rho_{Cu} = 1.68 \times 10^{-8} \Omega m \approx 0.12 \cdot \rho_{NdFeB}$ ) and a similar relative permeability ( $\mu_{r,Cu} \approx 1 \approx 0.93 \cdot \mu_{r,NdFeB}$ ). Consequently, the skin depth in EMs is smaller than in PMs  $\delta_{Cu} \approx 37 \mu m \approx 0.36 \cdot \delta_{NdFeB}$ , indicating a higher eddy current density on the material's surface near the excitation coil. Therefore, the detrimental field caused by eddy currents in EMs in the vertical space above the excitation coil is more pronounced than the one resulting from eddy currents in the stator PMs. Consequently, limiting the excitation coil's diameter to the dimension of the stator PM, a larger coupling with the target coil is expected, even though the coil's diameter is smaller than the MLP's characteristic dimension CD. The larger coupling between the excitation and the target coil is beneficial as larger eddy currents are induced in the target coil, finally leading to larger induced voltage in sensing coils and, thus, a better sensitivity. The same principle holds for the sensing coils, where the area of the outermost winding is maximized while minimizing the overlapping region with the stator and, most importantly, with the EMs (see **Fig. 4.2 (b)**). A total diameter of the sensing coils larger than the MLP's characteristic dimension is disregarded to preserve compactness. Regarding the target coil, a single-turn coil is applied on the mover's lateral surface so that the total weight and outer diameter are only marginally increased while maximizing the coupling area for the excitation coil's magnetic field. Further, the integrated circuit (IPS2550 [93]) used to drive the excitation coil, and to amplify and demodulate the high-frequency signals from the sensing coils, poses an additional constraint on the coils' design. Specifically, the excitation coil has to exhibit a resonant frequency in the frequency range  $f_{exc} = [2 \text{ MHz}, 5.6 \text{ MHz}]$  to be appropriately excited. A high number of turns  $N$  and an operating frequency  $f_{exc}$  close to the maximum are advantageous for achieving a large sensitivity since the induced voltage in the sensing coils directly depends on both design parameters (Faraday's law of induction). However, the coils' parasitic capacitances  $C_{exc}$  and  $C_{sens}$  limit the number of turns since they increase for greater  $N_{exc}$  and  $N_{sens}$ . The proposed design features a PCB carrying the excitation coil with  $N_{exc} = 10$  turns and the sensing coils with  $N_{sens} = 16$  turns, which are arranged as depicted in **Fig. 4.2 (b)**. The measured impedance of all eddy current sensor

coils is given in **Fig. 4.3 (c)**, where the operating frequency is  $f_{\text{exc}} = 3.1$  MHz, and the sensing coils' resonant frequency is  $f_{\text{sens}} = 7.6$  MHz. The numerical values of the equivalent lumped elements are listed in **Tab. 4.1**.

The measurement bandwidth of the eddy current sensor is limited by the IPS2550's internal demodulation process, which removes the high-frequency carrier signal to obtain low-frequency demodulated signals that depend on the mover's position. This process introduces a constant time delay of  $T_d = 4 \mu\text{s}$  valid in the whole operating frequency range. In the frequency domain, the time delay is approximated by a first-order transfer function (TF)  $H_d(s) = (2 - T_d s)/(2 + T_d s)$  [94] with a zero and a pole at  $f_d = 1/(\pi \cdot T_d) = 79.6$  kHz. Accordingly, the sensor's bandwidth is defined as the  $-3$  dB frequency of a phase-equivalent TF  $\tilde{H}_d(s) = 1/(2 + T_d s)^2$  and lies at  $f_{\text{bw,ECS}} = f_d \cdot \sqrt{\sqrt{2} - 1} = 51.2$  kHz. Since the approximate bandwidth is much larger than the mover's dynamics (maximum  $f_{\text{n,rot}} = 2$  Hz for the tilting as reported in **Tab. 4.3** and **Tab. 3.1**), we neglect the dynamics of the ECS during the MLP dynamics analysis and the position controller design.

### 4.2.3 Impact of Conductive Obstacles in the Air Gap

As previously highlighted, the RFS offers a broader range of applications than ECS, particularly due to its capability to function effectively in environments with conductive materials within the air gap. In this subsection, we examine how metal objects (aluminum and copper) influence the performance of the ECS.

Considering **Fig. 4.4**, when the mover is manually displaced by 1 mm back and forth from the center without materials in the air gap, the sensed voltage of the eddy current sensor varies between zero and approximately 12.3 mV (blue curve). However, when a conductive sheet is inserted in the air gap to mimic the situation where the mover is isolated and levitated in a hermetically sealed chamber, the mover's displacement is not recognizable in the sensed voltage (see orange and yellow traces in **Fig. 4.4**). This happens because the target coil on the mover is shielded from the excitation coil's magnetic field, which means that there are no eddy currents in the target coil; accordingly, no position-dependent opposing field occurs. In contrast, the RFS can still operate since the magnetic and electromagnetic forces acting on the mover are always reflected on the stator and EMs.

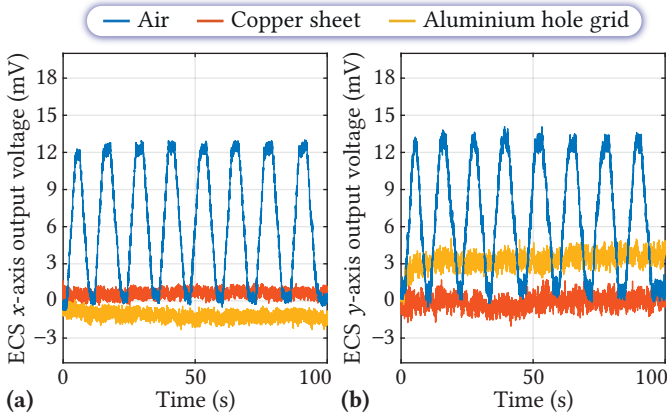


**Fig. 4.4:** ECS’s response for a manual radial displacement of the mover by 1 mm back and forth using a micropositioning stage for different mediums in the air gap. **(a)** and **(b)** show the results on the  $x$  and  $y$  axes, respectively. When a square conductive sheet (207 mm  $\times$  207 mm) that fully covers the PM stator and EMs is inserted in the middle of the air gap, i.e., at about 50 mm from the top surface of the PM stator, the magnetic coupling between the excitation, target, and sensing coils is heavily reduced due to the magnetic flux shielding, resulting in zero sensed voltage (neglecting the independent offsets, drifts, and noise). The copper sheet is 0.35 mm thick, whereas the aluminum foil is 1 mm thick and perforated, with holes having a diameter of 5 mm and a spacing of 2 mm.

### 4.3 Reaction Force-Based Position Sensor

This chapter briefly introduces the RFS, which is discussed in detail in **Chapter 3**, with the help of **Fig. 4.5**. This position sensing method consists of a force sensor capturing reaction forces on the stator caused by magnetic interactions between the PM stator and PM mover and electromagnetic interactions between the EMs mounted on the stator’s baseplate and the PM mover (see **Fig. 4.5 (a)**).

Accordingly, a three-axis ( $x, y, z$ ) strain gauge-based force sensor captures the total reaction force  $F_{\text{RFS}} = -F_{\text{PM}} - F_{\text{EM}} - F_{\text{rot}}$ . Four strain gauges arranged as a Wheatstone bridge are glued to each sensing element (one per cartesian axis  $x, y, z$ ) and are excited with a constant voltage  $u_{\text{exc,RFS}}$  (see **Fig. 4.5 (a)** and **(b)**). The total reaction force displaces the sensing side of the force sensor, resulting in the bending of the sensing element. This bending stretches the strain gauges, causing a change in their resistance, translating into a variation

of the output voltage  $u_{\text{sens,RFS}}$ . The trend of  $u_{\text{sens,RFS}}$  for a positive reaction force  $F_{\text{RFS}}$  is approximated with a linear relationship, as shown in Fig. 4.5 (c), according to the following relations.

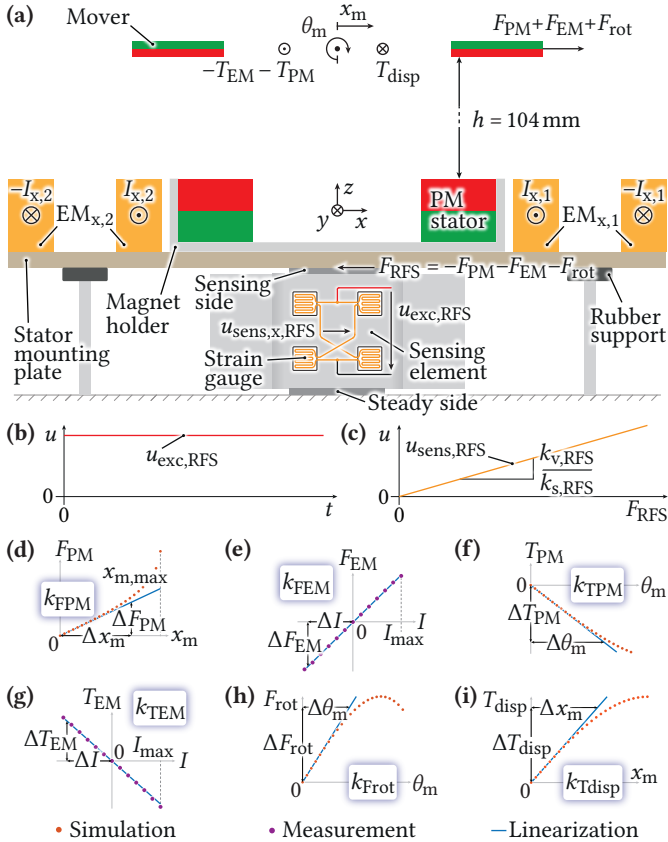


**Fig. 4.5:** (a) Section view of the MLP including the RFS with the corresponding  $x$  axis sensing element and strain gauges. The same arrangement is provided for measuring the  $y$  axis. (b) Constant voltage excitation for the strain gauges forming a Wheatstone bridge. (c) Expected RFS voltage output for a positive reaction force  $F_{\text{RFS}}$  acting on the sensing side due to the mover's motion and the electromagnetic force. (d)-(i) show the linearizations of different simulations and/or measurements performed on the MLP to build a model in the neighborhood of  $x_m = 0$ ,  $y_m = 0$ , and  $\theta_m = 0$ .

1. The movement of the force sensor's sensing side  $x_s$  and the bending of the sensing element are linearly related to the applied force, i.e.,  $x_s = F_{\text{RFS}}/k_{\text{s,RFS}}$ , where  $k_{\text{s,RFS}}$  is the stiffness of the force sensor.
2. The stretch of the strain gauges, their resistance change, and the output voltage variation are linearly dependent on the movement of the force sensor's sensing side, i.e.,  $u_{\text{sens,RFS}} = k_{\text{v,RFS}} \cdot x_s$ , where  $k_{\text{v,RFS}}$  is a constant representing the mechanical-to-electrical signal conversion.

From the sensed output voltage, information about the mover's position and tilting angle is gained since the total reaction force  $F_{\text{RFS}}$  depends on the mover's radial  $x, y$  position ( $F_{\text{PM}}$  in **Fig. 4.5 (d)**) and the mover's tilting around the  $x, y$  axes ( $F_{\text{tot}}$  in **Fig. 4.5 (h)**).

## 4.4 Dynamics Modeling and Verification

Developing a dynamic model for the MLP is a prerequisite for designing a controller capable of actively managing the mover's position. As discussed in **Section 4.2**, leveraging (4.1) reveals that the voltage signal from the ECS contains information about the mover's radial position and tilting angle. Therefore, an observer is necessary to distill at least the mover's position from the detected voltage. Subsequently, this positional information enables the controller to guide the mover by manipulating the system's sole input, namely, the EM's currents. Moreover, due to the significant levitation height, oscillations of the tilting angle are anticipated, which are not sufficiently dampened by the passive magnetic interactions. In response, the controller needs the estimated mover's angle – deduced from the sensed voltage by the observer – to actively mitigate any ensuing oscillations. To achieve this, we introduce the linearized dynamic model of the system, which is used for such observer. This model is validated by measurements and refined with calibration through Transfer Function (TF) measurements to ensure its robustness and accuracy (see **Subsection 3.4.2** for more details on disturbance TFs).

### 4.4.1 Dynamic Model

As shown in **Section 3.3** and reported here again for completeness, the mover's dynamic model is divided into two parts that describe the tilting around the radial axes  $x, y$  (**Fig. 4.6 (a)**) and the radial motion (displacement

from center) (**Fig. 4.6 (b)**). It should be noted that the tilting and displacement are coupled, which is modeled with constants  $k_{Tdisp}$  and  $k_{Frot}$ . For the direct comparison with the ECS, the third-order dynamic model of the force sensor used in **Section 3.3** is depicted in **Fig. 4.7 (a)**. This model comprises a stable mass-spring-damper system that replicates the mechanics of the sensing element (from  $F_{RFS}$  to  $x_s$ ), the mechanical-to-electrical conversion of the strain gauges glued to the sensing element ( $k_{v,RFS}$ ), the electronic amplification ( $k_{VGA}$ ), and a first-order low pass filter that attenuates noise and avoids aliasing effects in the subsequent analog-to-digital conversion (from  $u_{amp,RFS}$  to  $u_{filt,RFS}$ ).

For the ECS, the high-speed dynamics of the IPS2550 are simplified with the adjustable gain  $k_{IPS}$  (see **Fig. 4.7 (b)** and **Tab. 4.1**). To ensure a balanced comparison, the first-order analog low-pass filter is designed to mimic the phase response of the force sensor, complemented by a corresponding filter. Despite the difference in the orders of the two sensing systems, their phase responses are harmonized up to 20 Hz by calibrating the cutoff frequency of

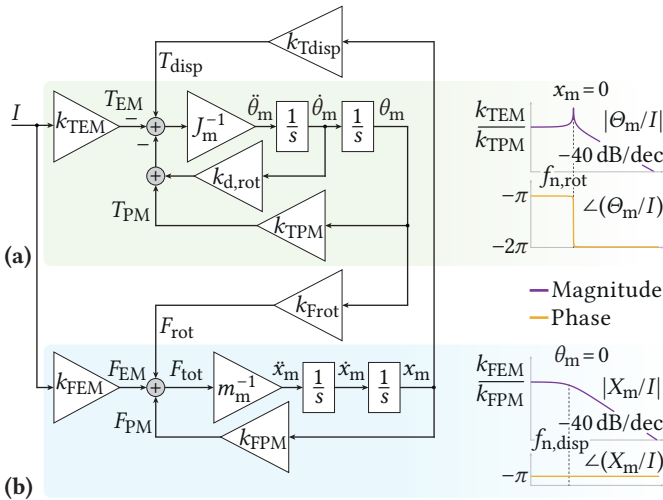


**Fig. 4.6:** Block diagram of the mover's dynamics for **(a)** tilting around the radial axes and **(b)** radial displacement, where the different dynamics are also represented as Bode diagrams. Here, only the displacement in  $x$  direction and the related tilting angle around the  $y$  axis, denoted as  $\theta_m$ , are considered. Due to symmetry, the same model holds for the  $y$  displacement and the tilting angle around  $x$  axis.

Chapter 4. Comparative Analysis of Force and Eddy Current Position Sensing Approaches for Magnetic Levitation Platform with an Exceptional Hovering Distance

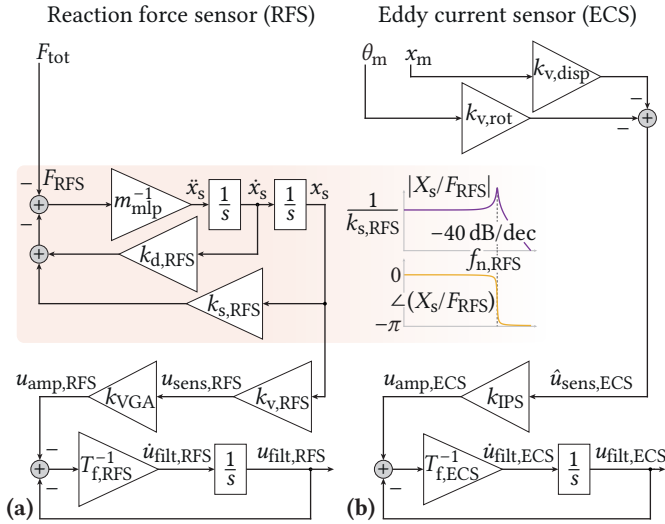


**Fig. 4.7:** (a) Block diagram of the RFS system dynamics with the second-order system modeling the movement of the force sensor’s sensing side, followed by the mechanical-to-electrical conversion of the strain gauges, amplification, and first-order active electronic filter. (b) Block diagram of the ECS with the zero-order model describing the conversion from the mover’s position to demodulated voltage, followed by the amplification and the first-order passive electronic filter.

the ECS to  $f_{f,ECS} = 1/(2\pi \cdot T_{f,ECS}) = 35$  Hz. Nonetheless, a deviation up to 1 dB at 20 Hz in the normalized magnitude responses is observed, attributable to the resonance peak in the force sensor’s TF.

In evaluating the modeling aspects of the two sensing systems, it is noted that the RFS exhibits a higher level of complexity due to its second-order TF behavior. Conversely, the ECS, characterized as a zero-order system, presents a more straightforward modeling process. However, this simplicity is accompanied by practical limitations, notably the constraint against encasing the mover in an electrically conductive capsule. Such drawback must be weighed against the ease of modeling the ECS offers, highlighting the necessity of a balanced assessment when considering integrating these sensing systems into the MLP.

#### 4.4.2 Dynamic Model Verification and Calibration

For verifying the dynamic model of the MLP using the ECS, two measurements of the TF injecting sinusoidal currents  $I$  in the EMs and observing the sensor's output  $u_{\text{out}}$  (defined as the sum of the filtered voltage  $u_{\text{filt}}$  of **Fig. 4.7** and the eventual disturbance voltage  $u_{\text{dist}}$ ) are performed, following the procedure described in **Section 3.4**. The measured system's TF  $G_{\text{meas},x} = U_{\text{out},x}/I_x$  with the mover levitating, free to move only along the  $x$  axis, and free to tilt around the  $y$  axis is shown in **Fig. 4.8 (a)** as a series of cyan points in the frequency range 0.1 Hz – 200 Hz. Compared to the theoretical TF  $G_{\text{tot},x} = U_{\text{filt},x}/I_x$  (solid red line), the same trend of the theoretical model of **Fig. 4.6** and **Fig. 4.7** is visible in the measurement, namely the static gain and the peak due to the mover's tilting around 2 Hz. However, a significant mismatch starting from 2 Hz must be corrected with a second measurement (calibration) where the mover is removed from the MLP and the TF measurement is repeated by injecting currents in the EMs, as described in **Subsection 3.4.2**. Following the model of **Fig. 4.7 (b)**, the ECS should register zero voltages  $u_{\text{filt},x}$  and  $u_{\text{filt},y}$ , as the mover's virtual position is zero. However, as shown in **Fig. 4.8 (b)**, TFs with a noticeable gain are measured, indicating parasitic couplings in the system that must be compensated.  $G_{\text{dist},xx}$  represents the disturbance for the modeled TF  $G_{\text{tot},x}$  and is obtained by injecting  $I_x$  in the EMs and measuring  $u_{\text{out},x}$  without the mover. Adding the fitted frequency response of  $G_{\text{dist},xx}$  to the modeled TF  $G_{\text{tot},x}$ , the measurement performed with the mover levitating is reproduced with better accuracy (cf.  $G_{\text{meas},x}$  with  $G_{\text{tot},x} + G_{\text{dist},xx}$  in **Fig. 4.8 (a)**). Another disturbance, which is measured by reading the sensor output  $u_{\text{out},x}$  while the system is excited with the current  $I_y$  and without the mover is the cross-coupling between the axes, indicated as  $G_{\text{dist},yx}$  in **Fig. 4.8 (b)**. This disturbance is neglected since the gain is about 160 times lower than the measured system's response  $G_{\text{meas},x}$  in the lower frequency range.

Accordingly, the observer (Kalman filter) for the ECS that extracts the mover's position  $(x_m, y_m)$  and tilting angles around  $x$  and  $y$  axes is implemented considering only the calibrated model  $G_{\text{tot},x} + G_{\text{dist},xx}$ . In contrast, the Kalman filter for the RFS contains the supplemental cross-coupling correction terms (see **Subsection 3.5.1**). In fact, the gain of  $G_{\text{dist},yx}$  in **Fig. 4.8 (b)** is not negligible compared to the calibrated model  $G_{\text{tot},x} + G_{\text{dist},xx}$  shown in **Fig. 4.8 (a)**.



## Chapter 4. Comparative Analysis of Force and Eddy Current Position Sensing Approaches for Magnetic Levitation Platform with an Exceptional Hovering Distance

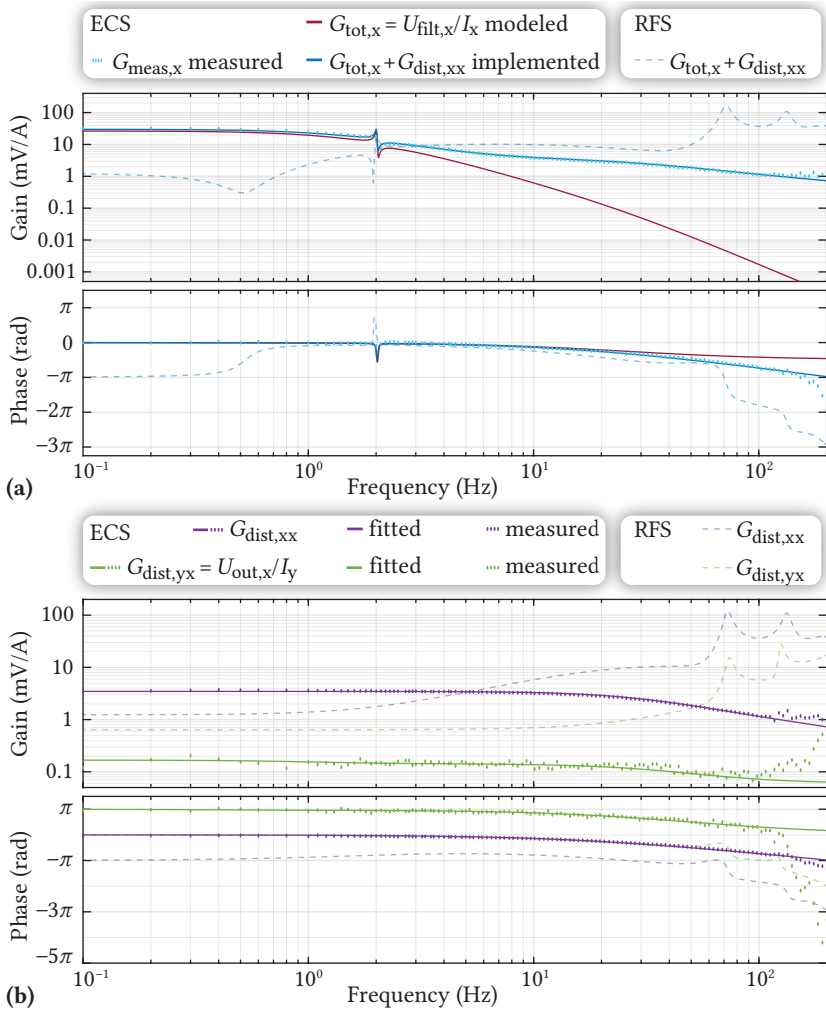


**Fig. 4.8:** TFs measurements to prove and calibrate the model presented in Fig. 4.6 and Fig. 4.7. (a) shows the frequency responses of the model, measurement, and observer implementation for the  $x$  axis while the mover levitates from an input current in  $x$  direction to the ECS's output. (b) shows the model disturbance  $G_{\text{dist},xx}$  and the cross-coupling between  $y$  current and  $x$  sensor output  $G_{\text{dist},yx}$  without mover for the ECS. The implemented TF, disturbance TF, and cross-coupling TF of the RFS seen in Fig. 3.8 are overlapped with dashed curves.

## 4.5 Comparative Results

This chapter compares the performance between the ECS and the RFS introduced in **Chapter 3** and briefly described in **Section 4.3** for steady-state levitation of the mover, which has been achieved using both sensing methods. A thorough analysis and comprehensive measurements have been conducted to understand the differences in performance and note the variations in the hardware realizations of the sensors.

### 4.5.1 Steady-State Levitation Comparison

The radial coordinates' reference is set to zero ( $x_m^* = y_m^* = 0$ ) for the steady-state levitation comparison between the ECS and RFS. The results shown in **Fig. 4.9 (a)** indicate the estimated mover's position using the ECS is close to the reference, with small fluctuations within the recorded time interval of twenty seconds. Conversely, when the RFS is used, the mover's displacements from the centered position are larger, caused by the force sensor's drift over time, which is compensated with an outer current controller loop, see **Subsection 3.5.4**. Despite all the disturbances and noise the RFS is facing in this application (see **Subsection 3.4.2**), we manage to have a stable levitation with deviations of up to 5.5 mm, which is 5.3 % of the levitation height.

The different performances resulting for the two sensors are also visible in 2D plots without direct time dependency shown in **Fig. 4.9 (b)-(e)**, where the  $x$ ,  $y$  quantities (observed mover's position, observed mover's angle, measured sensor's voltage, and measured control current) are plotted over the recorded levitating period. The standard deviation (STD), i.e., the measure of the amount of variation of the mover's radial position relative to its expected mean value, is calculated from the recorded data over the entire period as a performance metric. The STD of the mover's position for the RFS is  $(\sigma(x_m), \sigma(y_m))_{\text{RFS}} = (1.26 \text{ mm}, 1.60 \text{ mm})$ , whereas the ECS performs better with the STD of  $(\sigma(x_m), \sigma(y_m))_{\text{ECS}} = (0.05 \text{ mm}, 0.15 \text{ mm})$ . This result is confirmed considering **Fig. 4.9 (b)**, where larger mover's displacements are visible using the RFS, and relatively smaller deviations are observed when using the ECS.

Considering the plots in **Fig. 4.9 (b)-(e)** and focusing on the RFS's traces, it is visible that the control current has a similar shape as the inverse of the mover's position. In other words, a rotation by  $180^\circ$  around the center is required for the plot displaying the mover's position to see that the shape is correlated to the current.

Chapter 4. Comparative Analysis of Force and Eddy Current Position Sensing Approaches for Magnetic Levitation Platform with an Exceptional Hovering Distance

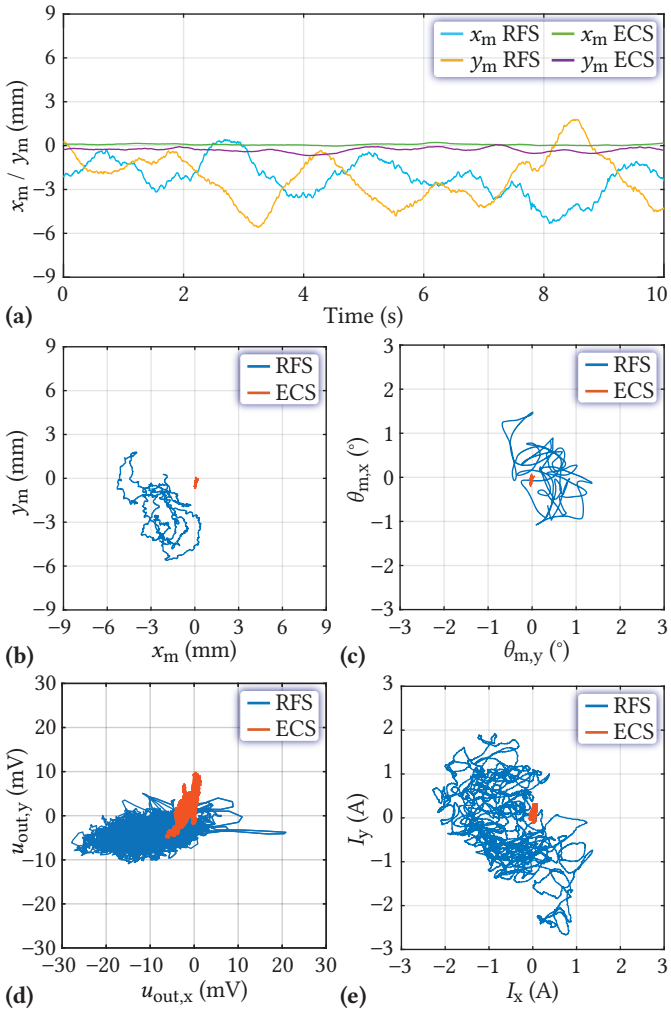


**Fig. 4.9:** Comparison between ECS and RFS during steady-state levitation of the mover with a reference position  $x_m = y_m = 0$ . (a) shows the time-domain curves of the observed mover's position, also reported as a 2D plot in (b). The recording time is 10 s, with 2.5 kHz sampling frequency resulting in a total of 25 000 data points. (c), (d), and (e) show the observed mover's tilting angle around the x, y axes, the measured position sensors' output voltage, and the measured control currents, respectively. The measurement data indicates better ECS position measurement performance.

The plot rotation corresponds to a negation of the quantities  $(x_m, y_m)$  since a positive current is required to counteract a negative mover's position, as depicted in **Fig. 4.2 (a)** and in the block diagram of the MLP in **Fig. 4.6 (b)**. The mover's angle adapts depending on the mover's position, e.g., the tilting angle around  $y$  axis,  $\theta_{m,y}$ , varies with a radial displacement along the  $x$  axis with  $y_m = 0$ , explaining the direct correlation between the two plots (cf. **Fig. 4.9 (b)** with **(c)** and note that  $\theta_{m,y}$  is shown on the horizontal axis as  $x_m$ ). Moreover, the controller cannot control the mover's angle to a reference value, but only actively dampens oscillations of the tilting angle around the  $x, y$  axes occurring at the natural frequency  $f_{n,rot} = 2$  Hz (see **Tab. 4.3** and **Subsection 3.5.2**). A similar correlation must exist between the sensed voltage and the observed mover's position and angle, as the latter quantities are extracted from the sensor's signal. However, it is difficult to identify a similar shape between the force sensor's voltage and the observed mover's position and tilting angle, indicating that disturbances and/or noise are present in the sensed signal. This statement is related to the TFs seen in **Fig. 4.8 (a)** and **(b)**, where the gain of the measured disturbance  $G_{dist,xx}$  and cross-coupling  $G_{dist,yx}$  is similar to the gain of the measured system's TF (matched by  $G_{tot,x} + G_{dist,xx}$  in **Fig. 3.8 (a)**). Due to lower SNR, the ECS trajectories presented in **Fig. 4.9** appear relatively small; a visual correlation between the measured quantities becomes evident in the presentation of results in **Section 4.6**.

## 4.5.2 Analysis of Performance Variance

This section highlights additional distinctions between the ECS and RFS-based MLP systems to explain their different performances. The first difference relates to a stronger correlation between the implemented and measured TFs observed for the ECS, as shown in **Fig. 4.8 (a)**. The observer implementation for the RFS system differs from the measurements in the lower frequency range from 0.1 Hz to 0.7 Hz (see **Fig. 3.8 (a)**). It should be noted that the presented solution performs the best among several fine-tuning attempts to improve the match in that frequency range by adjusting the constants shown in the block diagram of **Fig. 4.6** (i.e., changing the shape of the modeled TF).

The second difference relates to a comparative time-domain measurement without the mover and the results are shown in **Fig. 4.10**. Individually, both sensors are calibrated to zero at time 0 s using averaged data from past measurements while applying zero current to the EMs and continuously switching the 40 V DC-link voltage of the full-bridge two-level EMs' drive inverter. Subsequently, the position and current sensor signals are recorded for one second.

The amplitude of the noise voltage from the force sensor is larger than that from the eddy current sensor, as shown in **Fig. 4.10 (a)** as a time-domain plot and **Fig. 4.10 (c)** as a 2D plot. In quantitative terms, the RMS noise amplitude for the force sensor is  $(\hat{u}_{out,x}, \hat{u}_{out,y})_{RFS} = (1.87 \text{ mV}_{\text{rms}}, 1.70 \text{ mV}_{\text{rms}})$ , and for the eddy current sensor, it is  $(\hat{u}_{out,x}, \hat{u}_{out,y})_{ECS} = (0.22 \text{ mV}_{\text{rms}}, 0.31 \text{ mV}_{\text{rms}})$ . Furthermore, the same noise on the current signal is measured since the same inverter is used for testing both sensing systems, as illustrated in **Fig. 4.10 (b)** and **(d)**. For completeness, the corresponding RMS amplitudes are  $(\hat{I}_x, \hat{I}_y)_{RFS} = (13.5 \text{ mA}_{\text{rms}}, 8.2 \text{ mA}_{\text{rms}})$  and  $(\hat{I}_x, \hat{I}_y)_{ECS} = (13.4 \text{ mA}_{\text{rms}}, 8.1 \text{ mA}_{\text{rms}})$ . The Kalman filter includes all these measurement uncertainties by considering the voltage and current noise variance to adjust the Kalman gain when estimating the mover states. Therefore, due to the different noise levels in the

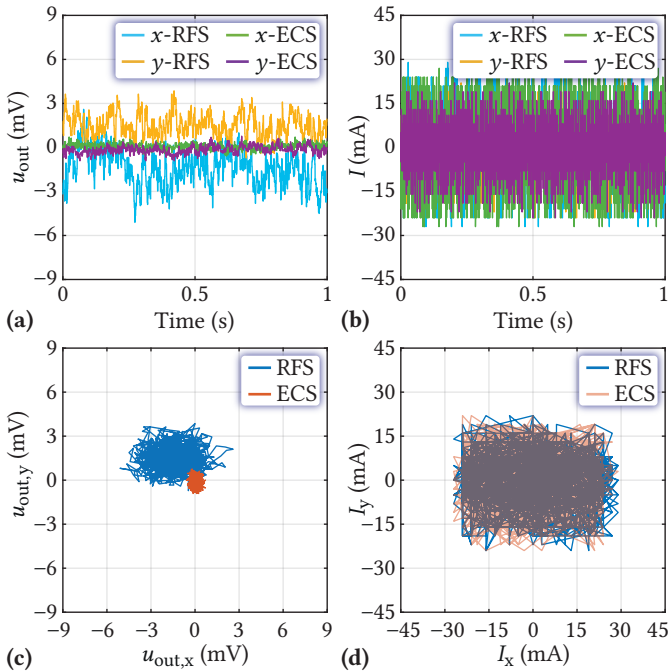


**Fig. 4.10:** Comparison of static measurements performed without mover, where the signals from the position sensors (a) and (c) and EM current sensors (b) and (d) are recorded for one second, indicating that the output of the RFS has a higher noise level than the ECS.

position sensors, the estimating performance of the Kalman filter is different.

The third difference is the signal-to-noise ratio (SNR), which is calculated to investigate both sensing systems by considering the waveforms in **Fig. 4.10 (a)**. The calculation assumes a displacement of the mover in the radial direction, neglects the tilting around the  $x, y$  axes ( $\theta_{m,y} = \theta_{m,x} = 0$ ), and takes no control action ( $I = 0$ ). According to the model presented in **Fig. 4.6** and **Fig. 4.7**, the static gain from the mover's position to the sensors' output is calculated and measured as

$$\frac{u_{\text{filt},x,\text{ECS}}}{x_m} = k_{v,\text{disp}} \cdot k_{\text{IPS}} = 12.3 \text{ mV/mm} \quad (4.2)$$

$$\frac{u_{\text{filt},y,\text{ECS}}}{y_m} = k_{v,\text{disp}} \cdot k_{\text{IPS}} = 12.3 \text{ mV/mm}. \quad (4.3)$$

$$\frac{u_{\text{filt},x,\text{RFS}}}{x_m} = \frac{k_{\text{FPM}}}{k_{s,x,\text{RFS}}} \cdot k_{v,x,\text{RFS}} \cdot k_{\text{VGA}} = 6.3 \text{ mV/mm} \quad (4.4)$$

$$\frac{u_{\text{filt},y,\text{RFS}}}{y_m} = \frac{k_{\text{FPM}}}{k_{s,y,\text{RFS}}} \cdot k_{v,y,\text{RFS}} \cdot k_{\text{VGA}} = 7.3 \text{ mV/mm} \quad (4.5)$$

The difference between the RFS's  $x, y$  quantities arises due to its asymmetrical construction (see **Chapter 3** for details on the constants). Consequently, the SNR for a displacement of the mover by  $x_m = y_m = 1 \text{ mm}_{\text{rms}}$  (RMS amplitude) around the radially centered position is given as

$$\text{SNR} = 20 \cdot \log_{10} \left( \frac{\hat{u}_{\text{filt}}}{\hat{u}_{\text{noise}}} \right), \quad (4.6)$$

where  $\hat{u}_{\text{filt}}$  is the RMS amplitude of the sensed noise voltage due to the mover's displacement calculated with (4.2), (4.3), (4.4), and (4.5).  $\hat{u}_{\text{noise}}$  is the RMS amplitude of the sensed voltage noise from **Fig. 4.10 (a)**. The resulting pairs are  $(\text{SNR}_x, \text{SNR}_y)_{\text{RFS}} = (10.5 \text{ dB}, 12.7 \text{ dB})$  and  $(\text{SNR}_x, \text{SNR}_y)_{\text{ECS}} = (35.0 \text{ dB}, 32.0 \text{ dB})$ , indicating that the mover's displacement of  $1 \text{ mm}_{\text{rms}}$  is distinguishable from noise for both sensors since positive values are obtained. However, the ECS measures a cleaner signal because its SNR is higher by about 20 dB. From another perspective, the lower detectable limits for the mover's displacement are calculated by equating  $\text{SNR} = 0$  and considering the measured noise amplitude. The results are  $(x_{m,\text{min}}, y_{m,\text{min}})_{\text{RFS}} = (0.30 \text{ mm}_{\text{rms}}, 0.23 \text{ mm}_{\text{rms}})$  and  $(x_{m,\text{min}}, y_{m,\text{min}})_{\text{ECS}} = (0.018 \text{ mm}_{\text{rms}}, 0.025 \text{ mm}_{\text{rms}})$ , indicating that the measurement with the ECS is about ten times higher in resolution. The difference is mainly due to the different noise level since the conversion from mover's position to voltage differs by about a factor of two for the ECS and the RFS (cf. (4.2) and (4.3))

with (4.4) and (4.5)).

The difference in the sensors' noise levels arises from various factors. First, the amplifier for the RFS is custom-made. It consists of a buffered ultra-low noise voltage reference [78] to excite the strain gauges, a manual offset compensation circuit for each axis, a variable gain amplifier (VGA) combined with an active  $RC$  filter for each axis, and a four-channel analog-to-digital converter (ADC) [79]. Instead, the coil excitation for the ECS and the processing of the received signal (amplification and demodulation) occur in a single integrated circuit [93]. The hardware is completed with a passive  $RC$  filter and the same ADC as the force sensor's one. Therefore, fewer components can pick up noise in the ECS's hardware. Second, the operating frequency range and the total gain for the electrical signal of the two sensors are substantially different. The amplifier for the RFS operates from zero frequency up to the bandwidth of the VGA (18 MHz) with a gain of 10 V/mV (80 dB). In contrast, the amplifier for the ECS amplifies signals by 240 V/V (47.6 dB) only at the excitation frequency of 3.1 MHz since the subsequent demodulation rejects noise at other frequencies. Hence, the RFS's amplifier enhances the probability of noise amplification. Finally, the spatial placement of the amplifier circuits within the MLP impacts the noise at their outputs. The sensing elements of both sensors (aluminum body with strain gauges and electromagnetic coils) are placed in the neighborhood of the EMs, which inevitably radiate high-frequency (HF) electromagnetic fields due to the HF current components caused by the switched power converter. The RFS's amplifier is placed on the side of the assembly formed by the PM stator and EMs. In contrast, the ECS's amplifier is placed directly under the assembly, i.e., at the same location as the RFS's aluminum body (see **Fig. 4.1** and **Fig. 4.5 (a)**). On the one hand, this arrangement can be advantageous for the RFS over the ECS because the source of electromagnetic radiation that can induce noise in the sensed signals is farther from the sensitive electronics. On the other hand, the analog signals must be routed over a longer distance for the RFS than for the ECS, rendering them more susceptible to noise. Thus, a definitive favorable placement cannot be determined in this context.

The main differences between the RFS and ECS are summarized in **Tab. 4.2**. A combination with another sensing principle could be employed for future developments on the RFS instead of using strain gauges that easily pick up noise and suffer from induced voltages. For example, precise eddy-current or optical sensors [95] could sense the displacement of the RFS's sensing side due to the reaction forces from the mover. According to **Tab. 4.2**, the ECS is more robust against noise than the RFS for using an off-the-shelf force sensor.

However, these approaches to advance the RFS increase the system's complexity and leave open challenges regarding the sensitivity and the cross-coupling between the axes, which must be solved by the mechanical design of the force sensor. When enhancing the force sensor's sensitivity through optimizing its mechanical design, reduced measurement bandwidth and lower load rating must be considered [96]. Conversely, it is observed that the sensitivity of the ECS does not negatively impact the measurement bandwidth. Enhancing the sensor's sensitivity through alternative coil designs or processing signals at higher frequencies does not necessarily result in a reduced bandwidth, as the IPS<sub>2550</sub>'s processing delay discussed in **Section 4.2.1** remains constant.

**Tab. 4.2:** Comparison of the main characteristics and performances of the RFS and the ECS. The standard deviation ( $\sigma$ ) of the mover's position from the reference position  $x_m^* = y_m^* = 0$  is calculated during steady-state levitation within a time interval of ten seconds. The RMS noise ( $\hat{u}_{out}$ ) is measured at the sensors' output voltage without the mover levitating. The SNR is calculated using the RMS noise, (4.2), (4.3), (4.4), and (4.5), derived from the MLP's models given in **Fig. 4.6** and **Fig. 4.7**.

	RFS	ECS
Mover can be encapsulated in a stainless steel chamber	Yes	No
Trade-off between sensitivity and bandwidth	Yes	No
Electromagnetic and mechanical disturbances	Large	Small
Cross-coupling	Large	Negligible
$\sigma(x_m)$	1.26 mm	0.05 mm
$\sigma(y_m)$	1.60 mm	0.15 mm
$\hat{u}_{out,x}$	1.87 mV <sub>rms</sub>	0.22 mV <sub>rms</sub>
$\hat{u}_{out,y}$	1.70 mV <sub>rms</sub>	0.31 mV <sub>rms</sub>
SNR <sub>x</sub>	10.5 dB	35.0 dB
SNR <sub>y</sub>	12.7 dB	32.0 dB



## 4.6 Additional Experimental Results for the Eddy Current Sensor

This chapter presents additional tests conducted with the ECS employed for position control to highlight features that can inspire new applications and show the MLP's servo capabilities that are not possible with the current version of the RFS.

### 4.6.1 Disturbance During Steady-State Levitation

In the first experiment, an external disturbance in the form of a hand-driven push on the mover during steady-state levitation allows for inspecting the levitation robustness of the MLP with ECS. As shown in **Fig. 4.11 (a)**, while the position and outer current controller are keeping the mover in the radially centered position, a disturbance is initiated at 5.6 s in the positive  $y$  direction. The mover displaces 4.8 mm from the origin with an angle of  $\theta_{m,x} = -1.9^\circ$  and an initial speed of  $dy_m/dt = 17.9$  mm/s. The approximate push force  $F_{\text{push}}$  is calculated from the position and current curves using the force balance equation

$$\begin{aligned} m_m \cdot \frac{d^2 y_m}{dt^2} &= F_{\text{push}} + F_{\text{PM}} + F_{\text{EM}} + F_{\text{rot}} \\ &= F_{\text{push}} + k_{\text{FPM}} \cdot y_m + k_{\text{FEM}} \cdot I + k_{\text{Frot}} \cdot \theta_{m,x}. \end{aligned} \quad (4.7)$$

The resulting impulse  $F_{\text{push}} = 0.19$  N is counteracted by the controller, which steers the mover back to the origin in 0.8 s after the disturbance initiation with a speed of 14.9 mm/s.

As a consequence of the perturbation, the mover starts spinning around the  $z$  axis. The spinning motion persists over time since this type of rotation cannot be stopped by magnetic torques or EMs. If the system is perfectly symmetric, the mover's rotation around the  $z$  axis should not be reflected on the radial quantities, such as position and tilting angle. However, the effect of the axial rotation is visible on the radial axes as a sinusoidal waveform with a period of about 80 s in the time-domain plot of **Fig. 4.11 (a)**. This observation, coupled with occasional axial rotations around the  $z$  axis during steady-state levitation, indicates that the manufactured MLP presents certain asymmetries.

Furthermore, the correlation between the current, the mover's position, and the tilting angle around the  $x$ ,  $y$  axes is visible in **Fig. 4.11 (b)-(e)**.

#### 4.6. Additional Experimental Results for the Eddy Current Sensor

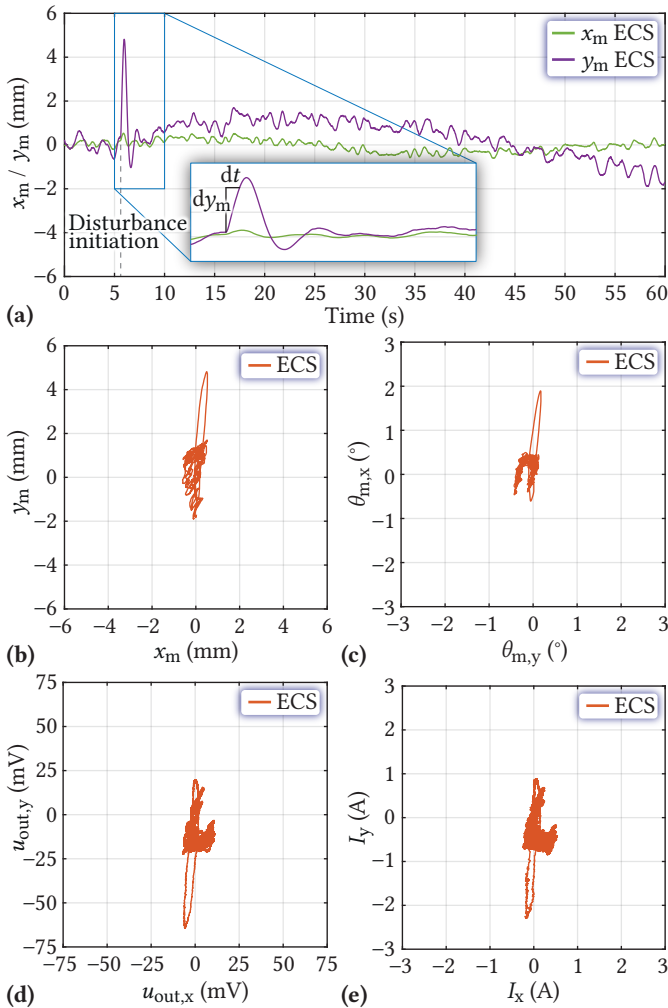


**Fig. 4.11:** Experiment performed on the MLP with ECS position sensing, where a manual push is applied to the mover. (a) and (b) show the observed mover's position. (c), (d), and (e) show the observed mover's tilting angle around the  $x$ ,  $y$  axes, the measured position sensor's output voltage, and the measured control current, respectively. The controller counteracts the disturbance; however, it could initiate a spinning motion of the mover around the  $z$  axis, worsening the levitation performance.

The similarity between the mover's position and angle and the sensed voltage follows the model shown in **Fig. 4.7 (d)**. A positive mover's radial position gives rise to a negative sensor's voltage, and a positive tilting angle around the  $x, y$  axes translates into a negative voltage.

### 4.6.2 Position Reference Tracking

In the second experiment, we fed the position controller with a time-varying position reference signal and observed the actual mover's position. The outer loop current controller (see **Fig. 3.9**) is omitted because it would inevitably interfere with the position controller. The references for the  $x$  and  $y$  axes position controllers are sinusoidal signals with an amplitude of 3 mm and a frequency of 0.1 Hz, and they are phase-shifted by  $90^\circ$  to steer the mover circularly within the  $x, y$  plane. The measurements are depicted in **Fig. 4.12**. The mover tracks the reference with an offset of  $(x, y) = (-0.98 \text{ mm}, 0.60 \text{ mm})$  about the origin and a standard deviation of  $(\sigma(x_m - x_{m,\text{ref}}), \sigma(y_m - y_{m,\text{ref}})) = (0.36 \text{ mm}, 0.24 \text{ mm})$  compared to the reference signals. The worse performance on the  $x$  axis compared to the steady-state levitation is due to the asymmetry within the MLP that generates an offset and initiates the spinning of the mover around the  $z$  axis. The spinning leads the mover toward positions that are harder to control, as shown between 90 s and 140 s in **Fig. 4.12 (a)** when  $x_m$  is at the minimum. Moreover, it results in a distorted circular trajectory in the 2D plot of **Fig. 4.12 (b)** for negative  $x_m$  and positive  $y_m$ .

Furthermore, the mover's tilting angle around the  $x, y$  axes shown in **Fig. 4.12 (c)** assumes a value depending on the radial position, and it cannot be controlled to an arbitrary reference value with the available EMs since they can only steer the radial position. However, active damping of the oscillations of the tilting angle around the  $x, y$  axes is achieved because the controller only targets the specific frequency  $f_{n,\text{rot}} = 2 \text{ Hz}$ .

#### 4.6. Additional Experimental Results for the Eddy Current Sensor

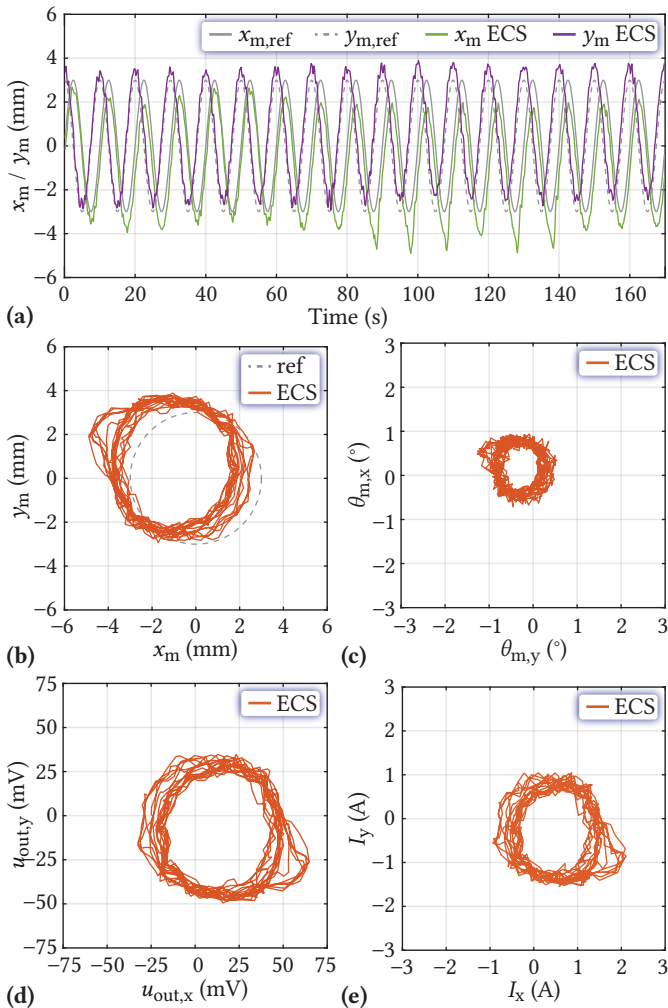


**Fig. 4.12:** Dynamic experiment performed using the ECS, where the controller has to steer the mover along a circular reference in the  $x, y$  plane. (a) and (b) show the observed mover's position. (c), (d), and (e) show the observed mover's tilting angle around the  $x, y$  axes, the measured position sensor's output voltage, and the measured control current, respectively. An asymmetry in the MLP gives rise to an offset position and a spinning of the mover around the  $z$  axis that negatively affect the tracking performance.

### 4.6.3 Position Reference Tracking with Payload

The last presented test consists of loading the mover with an additional weight and steering it in the  $x, y$  plane with a circular position reference to simulate the dynamical positioning of an actuator or a payload. The levitation height decreases to 70 mm due to the additional weight of 0.38 kg on the mover. Due to the payload, new constants in the model of **Fig. 4.6** and **Fig. 4.7 (b)** are required, leading to the values listed in **Tab. 4.3**. With this new configuration, the gain of the ECS  $k_{\text{IPS}}$  is unchanged since the voltage bounds of the ADC are not exceeded for the controllable range of the mover's positions. The natural frequencies of the mover's dynamics increase to  $f_{n,\text{disp}} = 1.74$  Hz and  $f_{n,\text{rot}} = 2.62$  Hz due to a greater increase in magnetic stiffness compared to the mass and moment of inertia. Nevertheless, the low pass filter's time constant (or cutoff frequency of 35 Hz) described by  $T_{f,\text{ECS}}$  is unchanged since it is already adequate, i.e., it is ten times larger than the mover's natural frequencies. New calibrations are not required since they are performed without the mover; thus, the same transfer functions as shown in **Fig. 4.8 (d)** are implemented in the observer.

The recorded data is displayed in **Fig. 4.13**, where the amplitude and the frequency of the position reference signals are set to 2 mm and 0.1 Hz, respectively. The tracking performance is measured with the standard deviation from the reference signals, resulting in  $(\sigma(x_m - x_{m,\text{ref}}), \sigma(y_m - y_{m,\text{ref}})) = (0.40 \text{ mm}, 0.70 \text{ mm})$ . A large part of the error is attributed to the offset from the center  $(x, y) = (-0.33 \text{ mm}, -0.27 \text{ mm})$  arising from the asymmetry in the MLP. The spinning of the mover around the  $z$  axis is inhibited by a manual (contactless) control during this measurement. Otherwise, the asymmetry combined with the spinning would destabilize the mover. For the manual control, an additional magnet is glued on the payload, and another magnet is brought into its vicinity to generate a compensating torque whenever a rotation is initiated. In a final design, this very basic technique would have to be replaced by an additional autonomous system consisting of non-axially symmetric magnets placed on the mover, a sensor, and electromagnets, which, however, increase the dimensions and complexity of the MLP.

#### 4.6. Additional Experimental Results for the Eddy Current Sensor

**Tab. 4.3:** MLP and ECS parameters with and without payload presence on the mover. The mover's mass and the payload are included in  $m_m$ . The only ECS parameters that differ from **Tab. 4.1** are  $k_{v,disp}$  and  $k_{v,rot}$ .

Magnetic levitation platform without payload			
Levitation height	$h$		104 mm
Characteristic dimension	CD		207 mm
Mover weight	$m_m$		0.36 kg
Mover moment of inertia	$J_m$		0.58 gm <sup>2</sup>
Radial stiffness	$k_{FPM}$		32.8 N/m
Displacement torque const.	$k_{Tdisp}$		0.25 Nm/m
Rotational stiffness	$k_{TPM}$		1.6 mNm/°
Rotational force const.	$k_{Frot}$		4.4 mNm/°
EMs force const.	$k_{FEM}$		65 mN/A
EMs torque const.	$k_{TEM}$		0.93 mNm/A
Rotational damping	$k_{d,rot}$		2 μNms/°
Rotation natural frequency	$f_{n,rot}$		2 Hz
Radial disp. natural frequency	$f_{n,disp}$		1.52 Hz
Magnetic levitation platform with payload of 0.38 kg			
$h$	70 mm	$m_m$	0.74 kg
$k_{FPM}$	88.1 N/m	$J_m$	1.54 gm <sup>2</sup>
$k_{TPM}$	7.3 mNm/°	$k_{FEM}$	170.4 mN/A
$k_{d,rot}$	20 μNms/°	$k_{TEM}$	1.4 mNm/A
$f_{n,rot}$	2.62 Hz	$f_{n,disp}$	1.74 Hz
Eddy current sensor			
$k_{v,disp}$	421.4 μV/mm	$k_{v,rot}$	250 μV/°

Chapter 4. Comparative Analysis of Force and Eddy Current Position Sensing Approaches for Magnetic Levitation Platform with an Exceptional Hovering Distance

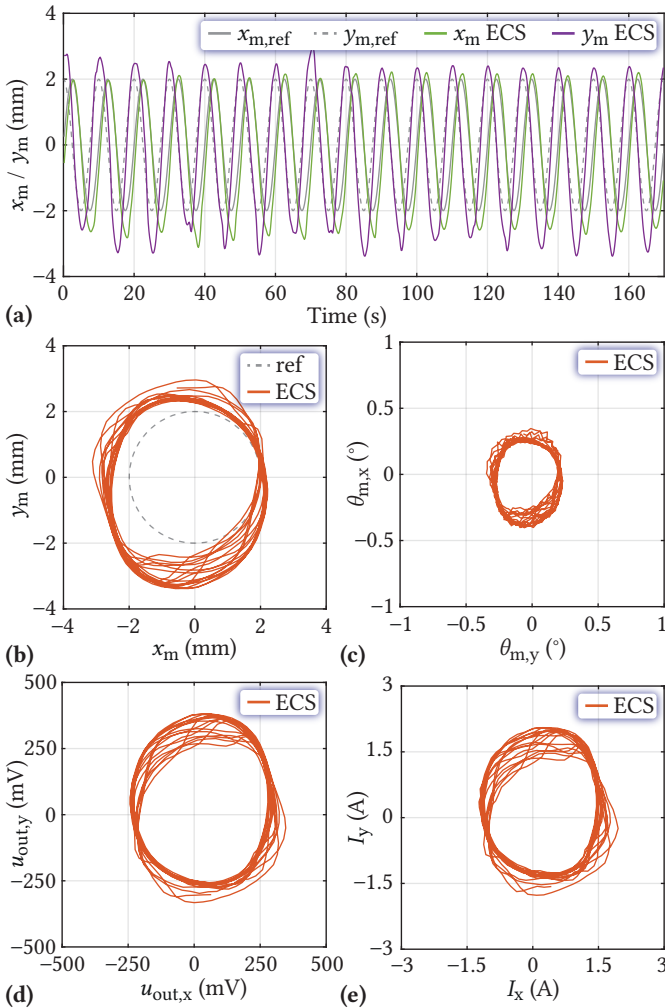


**Fig. 4.13:** Dynamic experiment with the ECS similar to that shown in Fig. 4.12, but with an additional weight of 0.38 kg placed on the mover that reduces the levitation height to 70 mm and dictates a change of the model parameters. (a) and (b) show the observed mover's position. (c), (d), and (e) show the observed mover's tilting angle around the  $x$ ,  $y$  axes, the measured position sensor's output voltage, and the measured control current, respectively. An asymmetry of the PMs in the MLP and the load causes a positional offset, impairing the tracking performance.

## 4.7 Conclusions

This chapter comparatively evaluates the performance of a reaction force-based position sensor (RFS) and an eddy current position sensor (ECS) in determining the radial position of the levitating permanent magnet (PM) mover in a magnetic levitation platform (MLP). Both sensors were integrated with an observer-based controller approach, a necessity brought by the intrinsic dynamics inherent in each sensor, and exhibited commendable qualities for different fields of application. To ensure a fair comparison in terms of cost and sensor complexity, we chose an off-the-shelf force sensor for the RFS application. In this case, the ECS stood out for its superior precision, demonstrating an approximately ten times higher accuracy than the RFS during steady-state levitation. Its performance was evaluated by calculating the standard deviation from the reference mover's position, resulting in  $(\sigma(x_m), \sigma(y_m))_{ECS} = (0.05 \text{ mm}, 0.15 \text{ mm})$  for a levitation height of  $h = 104 \text{ mm}$ . It also displayed remarkable resilience to disturbances, noise, and cross-couplings, thus offering a 20 dB higher signal-to-noise ratio  $(\text{SNR}_x, \text{SNR}_y)_{ECS} = (35.0 \text{ dB}, 32.0 \text{ dB})$  and enhanced performance reliability compared to the off-the-shelf RFS. On the other hand, the RFS demonstrates a unique advantage in scenarios where conductive materials are present in the air gap, a condition that limits the applicability of the ECS. This makes the RFS a valuable alternative for specialized applications, ensuring its relevance and utility in the diverse operational contexts of MLPs. Furthermore, the ECS showcased remarkable capabilities in handling static and dynamic tracking performances despite the challenges posed by asymmetries due to manufacturing tolerances in the MLP, highlighting its adaptability and robustness in various operational circumstances. In summary, while both sensors bring valuable qualities, the ECS distinguishes itself with higher precision and a higher SNR, making it exceptionally proficient in most MLP applications. The RFS, however, maintains its significance by offering applicability in the presence of conductive obstructions within the air gap, ensuring its indispensable role in specialized MLP scenarios.



# 5

## Conclusion and Outlook

### 5.1 Summary

Hybrid magnetic bearings are applied in electrical machines of turbocompressors, machining spindles, gas turbine generators, flywheels, and scanners, to mention a few examples. Additionally, they are employed in drives used in hermetically sealed chambers for wafer processing in the semiconductor industry and bioreactors in the pharmaceutical, chemical, and food industries. These hybrid magnetic bearings are characterized by a relatively small air gap compared to the characteristic dimension of the drive where they are employed. In contrast, this thesis explores magnetic levitation platforms (MLPs) featuring an air gap enlarged by one to two orders of magnitude, permitting an extension of current industrial applications. The presented MLP controlled using a force sensor enables the contactless support, transport, and rotation of objects within hermetically sealed process chambers having conductive walls.

Implementing such a system is possible starting with the proposed analytical method based on Lorentz's law to calculate the three-dimensional magnetic forces and torques between permanent magnets (PMs) and to determine the resulting passively stable degrees of freedom (DOFs). With the performed Pareto optimization of the PMs' dimensions, it is possible to select a suitable arrangement of PMs under constraints on the number of passively stable DOFs, the relative levitation height, the payload capability, the passive stiffnesses, and eventually, the PM dimensions. Additionally, applying the proposed scaling laws allows a fast redesign that avoids a new optimization process if the requirements regarding the constraints mentioned above would change. The remaining passively unstable DOFs are actively stabilized by a set

of electromagnets (EMs) designed to control the mover in a neighborhood of the center while minimizing the power consumption and trying to restrict the characteristic dimension of the system to preserve the large relative levitation height achieved with the optimal PM design.

The reaction force sensor used to determine the position of the mover to enable its closed-loop control opens the employment of the MLP in systems where an electrically conductive wall isolates the mover. Regarding the control algorithm, an observer first extracts the mover's radial position and angle from the measured forces considering their coupling. For this purpose, a dynamic model of the MLP, including the force sensor, is developed and accordingly augmented to compensate for unwanted disturbances. Finally, a controller based on the developed model allows controlling the mover's radial position and actively dampens its rotations around the radial axes since the rotations are poorly damped due to the relatively large air gap.

From the comparison between the force sensor and an alternative eddy current sensor for controlling the mover, it results that the force sensor poses more challenges than the eddy current sensor even though the same structure for the control algorithm is used. The force sensor offers an extended range of applications but suffers from a trade-off regarding its bandwidth and sensitivity, which are bounded by a lower and upper limit depending on the mover's dynamics. The need to decrease the bandwidth to a suitable minimum to maximize the sensitivity translates in a more complex modeling that affects the observer design. Moreover, the force sensor is prone to cross-coupling between the axes that further increases the observer's complexity. Finally, electromagnetic interference originating from the power electronics that drives the EMs constitutes a major problem for the force sensor.

In conclusion, the performance evaluation of both sensors shows that the eddy current sensor (ECS) outperforms the force sensor (FS) in the investigated MLP featuring a levitation height of 104 mm for a characteristic dimension of 207 mm. The standard deviation of the mover's radial position  $(x_m, y_m)$  from the steady-state reference  $(x_m^*, y_m^*) = (0, 0)$  is  $(\sigma(x_m), \sigma(y_m))_{\text{ECS}} = (0.15 \text{ mm}, 0.26 \text{ mm})$  for the eddy current sensor and  $(\sigma(x_m), \sigma(y_m))_{\text{FS}} = (2.00 \text{ mm}, 1.53 \text{ mm})$  for the force sensor.

## 5.2 Outlook

The following improvements could contribute to bringing the analyzed MLP closer to a possible industrial application.

- ▶ **Magnetic levitation platform:** the assembly including stator and EMs must be free of vibrations and movements caused by forces between the stator and EMs during control actions. Potting the mentioned components together would avoid their movements and reduce the vulnerability to disturbances, especially for the force sensor. The increased MLP weight due to the potting material would have to be considered since it influences the bandwidth of the force sensor.
- ▶ **Reaction force sensor:** the levitation performance could be improved by reducing the force sensor's cross-coupling between the axes with an enhanced mechanical design. Moreover, its susceptibility to disturbances in the form of induced voltages from EM currents and coupled electromagnetic interference from power electronics could be reduced with an alternative approach (optical force sensor) for measuring its bending that replaces the strain gauges. This approach would increase the levitation reliability but increase the cost of the force sensor.
- ▶ **Axial rotation control:** additional control of the mover's rotation around the vertical axis would be preferable for supporting, transporting, and rotating objects connected to the mover. The object could be directed, and its revolution enabled with such control. Within the analyzed MLP, the axial rotation is initiated by slight asymmetries in the manufactured PMs and cannot be stopped by the proposed EMs. Therefore, additional PMs must be mounted on the mover, additional EMs must be placed at the stator level, and an additional rotation sensor with a corresponding control algorithm must be implemented. This approach, however, would increase the complexity and size of the MLP.

# Appendices





# Design of the Electromagnets

This Appendix discusses the design of electromagnets (EMs) of the investigated magnetic levitation platform (MLP). A spatial arrangement analysis is conducted, equations for the multi-turn design showing dependencies on the dimensions and electrical quantities are given, and finally, the EM realization is considered.

As a starting point, a constraint on the positioning of the EMs is set to preserve the levitation height obtained by the choice of the permanent magnets (PMs) dimensions. The EMs can be placed in a region below the top face of the stator in the vertical direction, e.g., around the stator as shown in **Fig. 3.1** or between the stator and the force sensor. Regarding the number of EMs, at least three are required to control the mover on the 2D plane formed by the  $xy$  axes [97]. However, four have been chosen so that both axes can be decoupled to ease the measurement procedure using only two corresponding EMs for the dynamic model's verification. For the sake of demonstration, placement of the EMs parallel to the  $xy$  plane as shown in **Fig. A.1** is investigated.

## A.1 Positioning Analysis

To find the best position in the  $xy$  plane, a calculation based on Lenz's law is performed. The mover is displaced from the reference levitation point  $x = y = 0$  at the height  $h$  by a small step  $dx$  in  $x$  direction for simulating an unstable radial motion driven by magnetic forces. In both cases,  $x_m = 0$  and  $x_m = dx$ , the magnetic flux density in vertical direction  $B_{m,z}$  is calculated on the  $xy$  plane at the  $z$  position corresponding to the bottom face of the stator, using the model proposed in **Chapter 2**. Consequently, the difference  $dB_{m,z}$  is determined and illustrated as a contour plot in **Fig. A.1**, where it can be seen

that the regions with the largest change in magnetic flux density are located near the stator (yellow and blue zones). According to Lenz's law, a short-circuited single-turn winding that encircles a region with a time-varying magnetic flux density will experience an induced electromotive force (EMF) given by

$$\text{EMF} = -\frac{d\phi}{dt} = -\frac{\iint d\mathbf{B}_m \cdot d\mathbf{A}_w}{dt}, \quad (\text{A.1})$$

where  $\phi$  is the magnetic flux,  $d\mathbf{B}_m$  is the magnetic flux density vector passing through the area encircled by the winding, and  $d\mathbf{A}_w$  is the elemental area

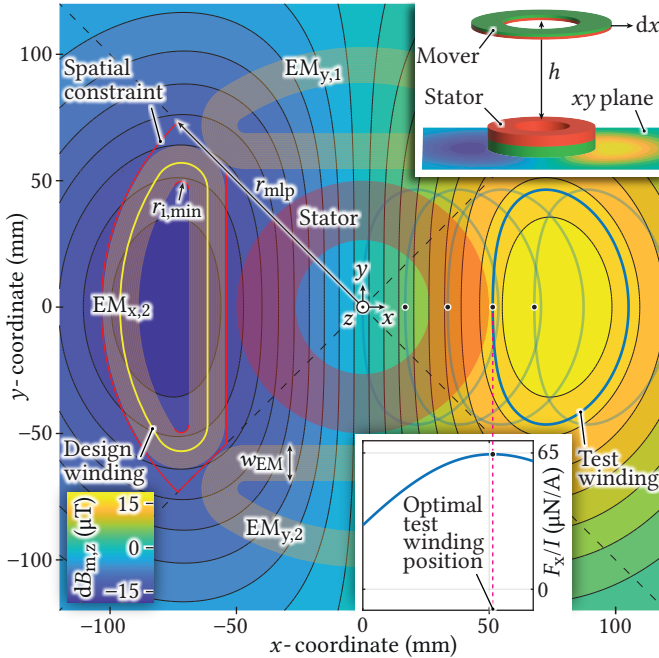


**Fig. A.1:** Contour plot of the magnetic flux change in the  $xy$  plane for a simulated movement of the mover in  $x$  direction from the radially centered position at the levitation height  $h$  by  $dx$ . With this plot, an optimal placement of the EM can be determined to obtain the largest possible force on the mover in the radial direction. For example, with the displacement in the  $x$  direction of a test winding, it is shown that its optimal location is exactly where the largest sum of  $dB_{m,z}$  in the winding's area is encircled.

vector perpendicular to the same surface. In this case,  $d\mathbf{A}_w = [0 \ 0 \ dA_{w,z}]^\top$  since the evaluation region lies in the  $xy$  plane, and therefore, only the vertical component  $dB_{m,z}$  is considered because the radial components of  $d\mathbf{B}_m$  do not contribute to the EMF generation due to the scalar product in (A.1). In addition, the time derivative is valid for the real system instead of the displacement used for the calculation since the mover travels the distance  $dx$  in the time span  $dt$ . As a consequence of (A.1), the largest force generated by the radial displacement of the mover on a short-circuited winding is found in the region that encloses the largest sum of magnetic flux density change. For example, without constraints on the winding's size, the  $xy$  plane with  $x > 0$  should be encircled by the winding since all the positive  $dB_{m,z}$  is summed with (A.1), resulting in the maximum possible force. The same holds for the  $xy$  plane with  $x < 0$ , where all the negative  $dB_{m,z}$  is enclosed. However, when a constraint on the overall size of the system exists, the optimal winding should encircle a region with the strongest  $dB_{m,z}$  so that it experiences the largest possible force, e.g., as illustrated by the test winding of **Fig. A.1**. According to Newton's third law of motion, the same force that the optimal short-circuited winding experiences due to a mover's displacement is reflected on the mover. Therefore, by opening the terminals of the optimal winding and injecting a current, the largest possible radial force on the mover is generated.

The relationship between the  $x$  position of a winding and the generated force  $F_x$  on the mover due to the current  $I$  can be seen in **Fig. A.1**. The normalized force  $F_x/I$  is calculated with the model from **Chapter 2** for different  $x$  positions of the test winding, where the maximum force is found when the largest sum of magnetic flux density change is encircled (at  $x = 51.4$  mm). Thereby, this different calculation method proves that the optimal position of a winding can be found by displacing the mover and evaluating the change of magnetic flux density over a plane.

## A.2 Multi-Turn Electromagnet

Considering the maximum achievable normalized force of the test winding  $F_x/I \approx 65 \mu\text{N}/\text{A}$ , it can be calculated how much current is needed to counteract the radial magnetic force that the mover experiences for a small displacement like  $x_m = 1$  mm: using the linearized model of the MLP, the absolute force that needs to be generated by the winding to keep the mover at the chosen location is  $F_{\text{PM}} = x_m \cdot k_{\text{FPM}} = 0.0328$  N, meaning that a current  $I = 505$  A would be required. This shows that a large amount of current is needed for compensating the destabilizing magnetic forces in a small neigh-



borhood of the natural levitation point, and even more current would be required to expand the controllable range of the mover, i.e., increase the robustness of the levitation against eventual external disturbances. Therefore, the design of a multi-turn electromagnet is discussed in the following. For this analysis, the magnetomotive force (or Ampère turns) required to compensate a given magnetic force with a normalized EM force is introduced and defined as

$$\text{MMF} = NI = \frac{F_{\text{PM}}}{F_x/I}, \quad (\text{A.2})$$

where  $N$  is the EM's number of turns. This shows that mainly two degrees of freedom are available to counteract the magnetic force, namely, the normalized force  $F_x/I$ , which depends on the winding's position and the MMF. The MMF can be split into two variables  $N$  and  $I$ , which depend on each other, meaning that the same MMF can be achieved with a large current and few turns and vice versa. However, imposing limits on, e.g., the maximum current that can be driven, a minimum number of turns can be obtained to reach a certain MMF. Thus, depending on the constraints introduced in the following, design limits for the EMs are derived.

As discussed, for  $F_x/I$ , it is advantageous to place the electromagnets around the stator as shown with the test winding at its optimal position (see **Fig. A.1**) and distribute the windings along the stator's height. In this vertical span, the picture of  $dB_{m,z}$  is very similar because the vertical range is small compared to the distance from the mover (i.e., the far field distribution is approximately the same). Moreover, the closer a winding is placed to the mover, the stronger the generated force is. Therefore, filling the vertical space with EMs from the stator's top face level down to the stator's bottom face level is convenient. When the vertical distribution of windings is not enough to generate the necessary force, a horizontal distribution becomes attractive, even though it partially worsens the optimal force generation, see **Fig. A.1**.

A choice of the vertical and horizontal span for the distribution of windings has to be made depending on the available space. Thus, with spatial constraints that define the available volume for the EM, such as the requirement of having four EMs symmetrically distributed around the stator, a maximum diameter of the overall magnetic levitation platform  $\text{CD} = 2 \cdot r_{\text{mlp}}$ , and a minimum internal radius  $r_{1,\text{min}}$  to avoid sharp edges that would complicate the manufacturing process. A winding area through which the EM's current flows having the dimensions  $w_{\text{EM}}$  and  $h_{\text{EM}}$  (width on the  $xy$  plane and height in  $z$  direction, respectively) can be defined. Accordingly, a design winding that passes through the center of the winding area (see **Fig. A.1**) is used to

approximately determine the achievable normalized force with the model proposed in **Chapter 2**, and therefore, the required magnetomotive force with (A.2) by setting a controllable range for the mover around the center position, where  $F_{PM} = k_{FPM} \cdot x_m$ . We consider a circular wire with diameter  $d_w$  (including the insulation) to wind the EMs, and employ the orthocyclic winding style for maximizing the compactness of the EM. The number of turns that can be fitted inside the defined winding area is found as depicted in **Fig. A.2**. The corresponding fill factor that defines the ratio between the

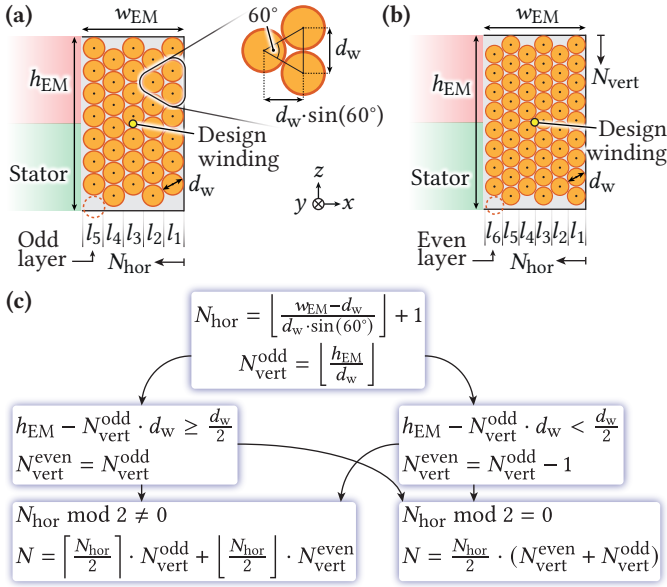


**Fig. A.2:** Cross section view of two different electromagnet realizations applying the orthocyclic winding style, depending on the used wire's diameter  $d_w$  and a defined winding area  $w_{EM} \cdot h_{EM}$ . (a) shows the case where the vertical number of turns is equal between odd and even layers, and  $N_{hor}$  is an odd number, whereas in (b), the vertical number of turns is different and  $N_{hor}$  is an even number. The number of turns can be determined using the equations in (c).

surface occupied by the windings and the whole available winding area is derived and equal to

$$k_{fill} = \frac{N \cdot \left(\frac{d_w}{2}\right)^2 \cdot \pi}{w_{EM} \cdot h_{EM}} \approx \frac{\pi}{2\sqrt{3}}, \quad (\text{A.3})$$

where the best case approximated value is found by considering three windings as shown in **Fig. A.2 (a)** [98]. Consequently, an approximated value for the number of turns can be written as

$$N \approx \frac{2}{\sqrt{3}} \cdot \frac{w_{EM} \cdot h_{EM}}{d_w^2}. \quad (\text{A.4})$$

The first limiting factor that has to be considered during the design is the current density through the EM's windings, which is calculated as

$$J = \frac{\text{MMF}}{k_{\text{fill}} \cdot w_{EM} \cdot h_{EM}} \approx \frac{2\sqrt{3}}{\pi} \cdot \frac{\text{MMF}}{w_{EM} \cdot h_{EM}}, \quad (\text{A.5})$$

and has to be limited to a maximum current density  $J_{\text{max}}$  depending on the type of cooling employed for the EMs. Therefore, for every wire diameter choice, a winding area, and a corresponding MMF, it must be ensured that  $J \leq J_{\text{max}}$  holds. Another related limiting parameter is the current flowing through the wire, which can be calculated as

$$I = \frac{\text{MMF}}{N} \approx \frac{\sqrt{3}}{2} \cdot \frac{\text{MMF}}{w_{EM} \cdot h_{EM}} \cdot d_w^2, \quad (\text{A.6})$$

and has to be limited to a maximum current  $I_{\text{max}}$  of the power electronics that supplies the EMs. It follows that there is a maximum diameter for the wire that can be used to wind the EMs depending on the required magnetomotive force and the chosen winding area, i.e.

$$d_{w,\text{max}} \approx \sqrt{I_{\text{max}} \cdot \frac{2}{\sqrt{3}} \cdot \frac{w_{EM} \cdot h_{EM}}{\text{MMF}}}. \quad (\text{A.7})$$

The analysis can be extended further to determine the approximate power required to counteract the worst-case magnetic force. For this, the approximate total length of the EM's wire  $l_{\text{tot}}$  has to be determined and can be assumed to be equal to the product between the number of turns and the length of the design winding  $l_w$ , i.e.,  $l_{\text{tot}} \approx N \cdot l_w$  since the latter is positioned in the middle of the winding area and nearly models the mean length of the horizontally distributed windings. Consequently, the resistance of the wire can be estimated as

$$R_{EM} \approx \rho \cdot \frac{N \cdot l_w}{\left(\frac{d_w}{2}\right)^2 \cdot \pi} \approx \rho \cdot \frac{8}{\pi\sqrt{3}} \cdot l_w \cdot \frac{w_{EM} \cdot h_{EM}}{d_w^4}, \quad (\text{A.8})$$

where  $\rho = 1.68 \times 10^{-8} \Omega \text{ m}$  is the electrical resistivity of copper at  $20^\circ$ . The maximum power dissipated in the EM to keep the mover at the reference radial position is obtained by squaring the DC current (A.6) and multiplying it with the electrical resistance (A.8) as

$$P_{\max} \approx \rho \cdot \frac{l_w \cdot \text{MMF}^2}{N \cdot \left(\frac{d_w}{2}\right)^2 \cdot \pi} \approx \rho \cdot \frac{6}{\pi\sqrt{3}} \cdot l_w \cdot \frac{\text{MMF}^2}{w_{\text{EM}} \cdot h_{\text{EM}}}, \quad (\text{A.9})$$

meaning that it is practically independent of the wire's diameter and only determined by the placement of the EM. With the information about the approximate resistance, the minimum voltage that has to be applied to the EM to reach the required current (i.e., for counteracting force on the mover) can be obtained by multiplying the current (A.6) and the resistance (A.8) as

$$U \approx \rho \cdot \frac{l_w \cdot \text{MMF}}{\left(\frac{d_w}{2}\right)^2 \cdot \pi} \approx \rho \cdot \frac{4}{\pi} \cdot l_w \cdot \frac{\text{MMF}}{d_w^2}. \quad (\text{A.10})$$

As for the current, the voltage has to be limited to a certain value  $U_{\max}$  that depends on the power electronics that supplies the EMs, i.e., a minimum conductor diameter has to be selected and calculated as

$$d_{w,\min} \approx \sqrt{\rho \cdot \frac{4}{\pi} \cdot l_w \cdot \frac{\text{MMF}}{U_{\max}}}. \quad (\text{A.11})$$

Finally, in this particular case where the EMs are carried on the sensing part of the force sensor and they contribute to the reduction of the sensor's resonant frequency (or bandwidth) as seen by (3.10), the EM's weight has to be considered and can be estimated to be independent of the chosen wire's diameter, i.e.

$$m_{\text{EM}} \approx \varrho \cdot k_{\text{fill}} \cdot w_{\text{EM}} \cdot h_{\text{EM}} \cdot l_w \approx \varrho \cdot \frac{\pi}{2\sqrt{3}} \cdot w_{\text{EM}} \cdot h_{\text{EM}} \cdot l_w, \quad (\text{A.12})$$

where  $\varrho = 8.96 \times 10^3 \text{ kg/m}^3$  is the density of the copper wire.

## A.3 Hardware Realization of the Electromagnets

The final realization of the EMs is constrained by the current and voltage of the power electronics inverter, the maximum RMS current density  $J_{\max}$ , and

the space around the stator that has to be minimized to get a compact MLP with respect to its large levitation height. Numerical values are summarized in **Tab. A.1**. The readily available inverter board [99] used to prove the functionality of the MLP offers enough integrated half-bridges (LMG5200) that can be combined to obtain the number of required full-bridge inverters that drive the EMs. The maximum allowed and selected voltage of the inverter board is  $U_{\max} = 40$  V and the maximum current capability for each half-bridge is 10 A. However, a maximum allowed current  $I_{\max} = 6$  A is chosen for the design of the EMs so that cooling the power semiconductors inside LMG5200 can be avoided and their reliability is increased. Similarly, a maximum RMS current density of  $J_{\max} = 10$  A/mm<sup>2</sup> is considered for the EMs so that an active cooling of the windings can be disregarded. It should be kept in mind that during nominal operation, a small current is required to keep the mover at the natural levitation point. Larger current values are required during eventual transient periods occurring due to external disturbances.

The first important requirement for the EM design is the definition of the mover's controllable range in the radial direction with respect to the center position  $x = y = 0$ , which determines the maximum magnetic force that has to be compensated by the EMs. This is chosen to be  $x_m = 10$  mm to give the sensing system enough room to be characterized and corresponds to a force  $F_{PM} = 0.328$  N. The following assumes that the EMs' force constant  $k_{FEM}$  is the same irrespective of the mover's radial position within the controllable range. This is confirmed by the approximately constant normalized force generated by the test winding in a neighborhood of its optimal position  $x = 51.4$  mm in **Fig. A.1**. With the fixed controllable range, the optimization goal is to minimize the magnetomotive force by increasing the normalized force produced by the winding (A.2) so that the current density (A.5), current (A.6), power (A.9), and voltage (A.10) are minimized since they have to be constrained to a certain finite value. For this purpose, an EM that includes as much area as possible would be required, meaning that the length  $l_w$  needs to be large. However, to minimize the power, voltage, and weight (A.12), a short total wire length is required, which partially contradicts the first optimization target since, with a decrease in length, an automatic decrease in area is obtained. To achieve the minimum required MMF for the shortest wire and knowing that the final MLP's size also has to be minimized, the radius  $r_{mlp}$  that determines the characteristic dimension of the system (see **Fig. A.1**) is iteratively increased until the required force can be reached without exceeding the voltage, current, and current density limits. During the iterative process, the spatial constraints, such as the distance toward the stator and

the adjacent EMs, are kept the same, a minimum radius  $r_{i,\min} = 3$  mm to ease the manufacturing process is defined, and  $h_{\text{EM}} = 23$  mm is chosen to be equal to the stator's height (considering additional 3 mm of plastic for the magnet holder) to get a compact design. Given these parameters, the width of the EM is automatically determined. The second design variable is the wire's diameter, which is restricted to an approximate range given by (A.7) and (A.11), and can be freely chosen once a feasible EM is found.

With all the above considerations, the EMs that have finally been manufactured originate from the shown design winding in **Fig. A.1** that alone produces a normalized force  $F_x/I = 62.9 \mu\text{N}/\text{A}$  on the mover. Its position for the force calculation using the method in **Chapter 2** is determined by the radius  $r_{\text{mlp}} = 103.5$  mm and the winding area ( $w_{\text{EM}} = 14.85$  mm,  $h_{\text{EM}} = 23$  mm). Accordingly, the required magnetomotive force is calculated considering that two EMs contribute to the radial force generation since one drags and the other pushes the mover toward the center. This leads to the normalized force being multiplied by two in (A.2); hence, resulting in  $\text{MMF} = 2.48$  kA. Knowing the magnetomotive force, the length of the

**Tab. A.1:** Parameters for the design of the EMs and their calculated characteristics. Please note that the calculated resistance  $R_{\text{EM}}$  differs from the measurement reported in **Tab. 3.2** by 1.8 %.

Design parameters			
$U_{\max}$	40 V	$I_{\max}$	6 A
$J_{\max}$	$10 \text{ A}_{\text{rms}}/\text{mm}^2$	$x_{\text{m}}$	10 mm
$r_{i,\min}$	3 mm	$h_{\text{EM}}$	23 mm
$w_{\text{EM}}$	14.85 mm	$r_{\text{mlp}}$	103.5 mm
$d_{\text{w}}$	0.82 mm	$d_{\text{w,Cu}}$	0.75 mm
Calculated characteristics			
$N$	550	$N_{\text{hor}}$	20
$N_{\text{vert}}^{\text{odd}}$	28	$N_{\text{vert}}^{\text{even}}$	27
$k_{\text{fill}}$	0.71	$J$	$10.2 \text{ A}_{\text{rms}}/\text{mm}^2$
$I$	4.5 A	$R_{\text{EM}}$	5.4 $\Omega$
$P_{\max}$	109 W	$m_{\text{EM}}$	0.56 kg

design winding  $l_w = 257.4$  mm, the inverter limits, and the material of the wire (copper), the approximate wire's diameter range can be calculated with (A.7) and (A.11) as  $0.58 \text{ mm} \leq d_w \leq 0.98 \text{ mm}$ . Consequently, with the chosen wire's diameter  $d_w = 0.82$  mm that includes the insulation, the number of turns following the calculations in **Fig. A.2 (c)** results to be  $N = 550$  with 20 horizontal layers and 27.5 vertical layers (alternating between 27 and 28 turns for the even and odd layers, respectively). For all other parameters, the more accurate copper diameter  $d_{w,Cu} = 0.75$  mm is considered leading to the following values: the fill factor is  $k_{\text{fill}} = 0.71$ , the current density results to be  $J = 10.2 \text{ A/mm}^2$ , the corresponding current is  $I = 4.5 \text{ A}$ , the approximate resistance is  $R_{EM} = 5.4 \Omega$  which defines the maximum power consumption of each EM  $P_{\text{max}} = 109 \text{ W}$  and the minimum DC-link voltage  $U = 24.3 \text{ V}$ , finally, the approximate weight per EM is  $m_{EM} = 0.56 \text{ kg}$ . In practice, it has been observed that the EMs do not run into a thermal runaway even if larger currents as  $I_{\text{max}} = 5 \text{ A}$  are used for short periods of time during transients. Therefore, the marginally excessive current density is not an issue. Comparing the force generation, the manufactured EMs have a simulated force constant  $k_{FEM} = 68.6 \text{ mN/A}$  (as reported in **Tab. 3.1**), which is calculated from the sum of forces of each winding in the EM when two EMs per axis are used for the control, whereas the designed EMs that rely on the design winding have a slightly higher force constant that can be determined as  $k_{FEM} = 2 \cdot F_x / I \cdot N = 69.2 \text{ mN/A}$ . The small error ( $< 1\%$ ) on the EMs' force constant lies in the assumption that the spatially distributed windings of the EM are approximated to a single design winding for the normalized force calculation.

# Bibliography

- [1] T. I. Baumgartner, “A Magnetically Levitated 500 000 rpm Electrical Drive System,” Ph.D. Dissertation, ETH Zurich, 2013, DOI: [10.3929/ethz-a-010117358](https://doi.org/10.3929/ethz-a-010117358).
- [2] T. C. Schneeberger, “Integriertes magnetisches Lagerungs- und Antriebs-system für Halbleiterwafer,” Ph.D. Dissertation, ETH Zurich, 2008, DOI: [10.3929/ethz-a-005877534](https://doi.org/10.3929/ethz-a-005877534).
- [3] T. Reichert, “The Bearingless Mixer in Exterior Rotor Construction,” Ph.D. Dissertation, ETH Zurich, 2012, DOI: [10.3929/ethz-a-007630320](https://doi.org/10.3929/ethz-a-007630320).
- [4] Kest Technology, “Mixers.” [Online]. Available: <https://kest.se/group/mixers/>
- [5] Stirlingkit, “800 g DIY Magnetic Levitation Module.” [Online]. Available: <https://www.stirlingkit.com/products/800g-diy-magnetic-levitation-module>
- [6] H. Davis and L. Whitehead, “Magnetic Levitation Apparatus,” Patent WO2 004 030 198A2, Apr., 2004.
- [7] G. L. M. Jansen, “Magnetic Levitation Apparatus,” Patent WO2 009 038 464A2, Mar., 2009.
- [8] R. W. Bosley, “Magnetic Levitation System,” Patent EP0 193 664A1, Sep., 1986.
- [9] A. Filatov and E. Maslen, “Passive Magnetic Bearing for Flywheel Energy Storage Systems,” *IEEE Transactions on Magnetics*, vol. 37, no. 6, pp. 3913–3924, Nov. 2001, DOI: [10.1109/20.966127](https://doi.org/10.1109/20.966127).
- [10] T. Masuzawa, S. Ezo, T. Kato, and Y. Okada, “Magnetically Suspended Centrifugal Blood Pump with an Axially Levitated Motor,” *Artificial Organs*, vol. 27, no. 7, pp. 631–638, 2003, DOI: [10.1046/j.1525-1594.2003.07111.x](https://doi.org/10.1046/j.1525-1594.2003.07111.x).
- [11] M. B. Khamesee and E. Shameli, “Regulation Technique for a Large Gap Magnetic Field for 3D Non-Contact Manipulation,” *Mechatronics*, vol. 15, no. 9, pp. 1073–1087, Nov. 2005, DOI: [10.1016/j.mechatronics.2005.06.005](https://doi.org/10.1016/j.mechatronics.2005.06.005).
- [12] X. Wang and L. Li, “Magnetic Suspension Device,” Patent US8 294 542B2, Oct., 2012.



- [13] J.-P. Yonnet, "Permanent Magnet Bearings and Couplings," *IEEE Transactions on Magnetics*, vol. 17, no. 1, pp. 1169–1173, Jan. 1981, DOI: [10.1109/TMAG.1981.1061166](https://doi.org/10.1109/TMAG.1981.1061166).
- [14] G. Akoun and J.-P. Yonnet, "3D Analytical Calculation of the Forces Exerted Between Two Cuboidal Magnets," *IEEE Transactions on Magnetics*, vol. 20, no. 5, pp. 1962–1964, Sep. 1984, DOI: [10.1109/TMAG.1984.1063554](https://doi.org/10.1109/TMAG.1984.1063554).
- [15] E. Furlani, "A Formula for the Levitation Force Between Magnetic Disks," *IEEE Transactions on Magnetics*, vol. 29, no. 6, pp. 4165–4169, Nov. 1993, DOI: [10.1109/20.280867](https://doi.org/10.1109/20.280867).
- [16] R. Ravaud, G. Lemarquand, V. Lemarquand, and C. Depollier, "Analytical Calculation of the Magnetic Field Created by Permanent-Magnet Rings," *IEEE Transactions on Magnetics*, vol. 44, no. 8, pp. 1982–1989, Aug. 2008, DOI: [10.1109/TMAG.2008.923096](https://doi.org/10.1109/TMAG.2008.923096).
- [17] S. Babic and C. Akyel, "Improvement in the Analytical Calculation of the Magnetic Field Produced by Permanent Magnet Rings," *Progress In Electromagnetics*, vol. 5, pp. 71–82, 2008.
- [18] R. Ravaud, G. Lemarquand, and V. Lemarquand, "Force and Stiffness of Passive Magnetic Bearings Using Permanent Magnets. Part 1: Axial Magnetization," *IEEE Transactions on Magnetics*, vol. 45, no. 7, pp. 2996–3002, Jul. 2009, DOI: [10.1109/TMAG.2009.2016088](https://doi.org/10.1109/TMAG.2009.2016088).
- [19] R. Ravaud, G. Lemarquand, and V. Lemarquand, "Force and Stiffness of Passive Magnetic Bearings Using Permanent Magnets. Part 2: Radial Magnetization," *IEEE Transactions on Magnetics*, vol. 45, no. 9, pp. 3334–3342, Sep. 2009, DOI: [10.1109/TMAG.2009.2025315](https://doi.org/10.1109/TMAG.2009.2025315).
- [20] W. Robertson, B. Cazzolato, and A. Zander, "A Simplified Force Equation for Coaxial Cylindrical Magnets and Thin Coils," *IEEE Transactions on Magnetics*, vol. 47, no. 8, pp. 2045–2049, Aug. 2011, DOI: [10.1109/TMAG.2011.2129524](https://doi.org/10.1109/TMAG.2011.2129524).
- [21] S. Babic, C. Akyel, J. Martinez, and B. Babic, "A New Formula for Calculating the Magnetic Force Between Two Coaxial Thick Circular Coils with Rectangular Cross-Section," *Journal of Electromagnetic Waves and Applications*, vol. 29, no. 9, pp. 1181–1193, Jun. 2015, DOI: [10.1080/09205071.2015.1035807](https://doi.org/10.1080/09205071.2015.1035807).

- 
- [22] H. Qin, Z. Ming, T. Wen, and Y. Zhao, “Force Calculation for Hybrid Magnetic Levitation System,” in *Proc. of the 14th International Conference on Computational Intelligence and Security (CIS)*, Nov. 2018, pp. 88–92, DOI: [10.1109/CIS2018.2018.00027](https://doi.org/10.1109/CIS2018.2018.00027).
- [23] M. Lahdo, T. Ströhla, and S. Kovalev, “Semi-Analytical 3D Force Calculation of an Ironless Cylindrical Permanent Magnet Actuator for Magnetic Levitation Systems,” *The Applied Computational Electromagnetics Society Journal (ACES)*, vol. 34, no. 4, pp. 520–527, Apr. 2019.
- [24] M.-S. Sim and J.-S. Ro, “Semi-Analytical Modeling and Analysis of Halbach Array,” *Energies*, vol. 13, no. 5 (1252), pp. 1–11, Jan. 2020, DOI: [10.3390/en13051252](https://doi.org/10.3390/en13051252).
- [25] Tecnotion BV, “UM Series Ironless,” Datasheet, 2021. [Online]. Available: <https://www.tecnotion.com/products/ironless-motors-um-series/>
- [26] R. Post, T. Fowler, and S. Post, “A High-Efficiency Electromechanical Battery,” *Proc. of the IEEE*, vol. 81, no. 3, pp. 462–474, Mar. 1993, DOI: [10.1109/5.241483](https://doi.org/10.1109/5.241483).
- [27] E. P. Furlani, *Permanent Magnet and Electromechanical Devices*. Academic Press, Aug. 2001, DOI: [10.1016/B978-0-12-269951-1.X5000-1](https://doi.org/10.1016/B978-0-12-269951-1.X5000-1).
- [28] G. Jungmayr, E. Marth, W. Amrhein, H.-J. Berroth, and F. Jeske, “Analytical Stiffness Calculation for Permanent Magnetic Bearings with Soft Magnetic Materials,” *IEEE Transactions on Magnetics*, vol. 50, no. 8, pp. 1–8, Aug. 2014, DOI: [10.1109/TMAG.2014.2310437](https://doi.org/10.1109/TMAG.2014.2310437).
- [29] J. Janssen, J. Paulides, L. Encica, and E. Lomonova, “Analytical Modeling of Permanent Magnets on a Soft Magnetic Support for a Suspension System,” in *Proc. of the International Conference on Electrical Machines and Systems*, Oct. 2008, pp. 3825–3830.
- [30] S. Earnshaw, “On the Nature of the Molecular Forces which Regulate the Constitution of the Luminiferous Ether,” *Transactions of the Cambridge Philosophical Society*, vol. 7, pp. 97–112, Jan. 1848.
- [31] A. Bettini, *A Course in Classical Physics 3 – Electromagnetism*, ser. Undergraduate Lecture Notes in Physics. Cham: Springer International Publishing, 2016, DOI: [10.1007/978-3-319-40871-2](https://doi.org/10.1007/978-3-319-40871-2).
- [32] A. E. Fitzgerald, C. Kingsley, and S. D. Umans, *Electric Machinery*, 6th ed. McGraw-Hill, 2003.

- [33] S. Babic and C. Akyel, "Magnetic Force Between Inclined Circular Filaments Placed in Any Desired Position," *IEEE Transactions on Magnetics*, vol. 48, no. 1, pp. 69–80, Jan. 2012, DOI: [10.1109/TMAG.2011.2165077](https://doi.org/10.1109/TMAG.2011.2165077).
- [34] K.-B. Kim, E. Levi, Z. Zabar, and L. Birenbaum, "Restoring Force Between Two Noncoaxial Circular Coils," *IEEE Transactions on Magnetics*, vol. 32, no. 2, pp. 478–484, Mar. 1996, DOI: [10.1109/20.486535](https://doi.org/10.1109/20.486535).
- [35] K.-B. Kim, E. Levi, Z. Zabar, and L. Birenbaum, "Mutual Inductance of Noncoaxial Circular Coils with Constant Current Density," *IEEE Transactions on Magnetics*, vol. 33, no. 5, pp. 4303–4309, Sep. 1997, DOI: [10.1109/20.620439](https://doi.org/10.1109/20.620439).
- [36] H. A. Haus and J. R. Melcher, *Electromagnetic Fields and Energy*. Englewood Cliffs: Prentice Hall, 1989.
- [37] Y.-C. Lai, Y.-L. Lee, and J.-Y. Yen, "Design and Servo Control of a Single-Deck Planar MAGLEV Stage," *IEEE Transactions on Magnetics*, vol. 43, no. 6, pp. 2600–2602, Jun. 2007, DOI: [10.1109/TMAG.2007.893530](https://doi.org/10.1109/TMAG.2007.893530).
- [38] H. Zhu, T. J. Teo, and C. K. Pang, "Design and Modeling of a Six-Degree-of-Freedom Magnetically Levitated Positioner Using Square Coils and 1-D Halbach Arrays," *IEEE Transactions on Industrial Electronics*, vol. 64, no. 1, pp. 440–450, Jan. 2017, DOI: [10.1109/TIE.2016.2598811](https://doi.org/10.1109/TIE.2016.2598811).
- [39] M. Lahdo, T. Ströhla, and S. Kovalev, "Design and Implementation of an New 6-DOF Magnetic Levitation Positioning System," *IEEE Transactions on Magnetics*, vol. 55, no. 12, pp. 1–7, Dec. 2019, DOI: [10.1109/TMAG.2019.2936394](https://doi.org/10.1109/TMAG.2019.2936394).
- [40] X. Zhang, C. Trakarnchaiyo, H. Zhang, and M. B. Khamesee, "MagTable: A Tabletop System for 6-DOF Large Range and Completely Contactless Operation Using Magnetic Levitation," *Mechatronics*, vol. 77, no. 102600, pp. 1–10, Aug. 2021, DOI: [10.1016/j.mechatronics.2021.102600](https://doi.org/10.1016/j.mechatronics.2021.102600).
- [41] C. Trakarnchaiyo, Y. Wang, and M. B. Khamesee, "Design of a Compact Planar Magnetic Levitation System with Wrench–Current Decoupling Enhancement," *Applied Sciences*, vol. 13, no. 4 (2370), pp. 1–22, 2023, DOI: [10.3390/app13042370](https://doi.org/10.3390/app13042370).
- [42] E. A. Lomonova, "Advanced Actuation Systems - State of the Art: Fundamental and Applied Research," in *Proc. of the IEEE International Conference on Electrical Machines and Systems*, Oct. 2010, pp. 13–24.

- [43] G. Stadler, E. Csencsics, S. Ito, and G. Schitter, “High Precision Hybrid Reluctance Actuator with Integrated Orientation Independent Zero Power Gravity Compensation,” *IEEE Transactions on Industrial Electronics*, vol. 69, no. 12, pp. 13 296–13 304, Dec. 2022, DOI: [10.1109/TIE.2021.3137444](https://doi.org/10.1109/TIE.2021.3137444).
- [44] D. Wertjanz, E. Csencsics, J. Schlarp, and G. Schitter, “Design and Control of a MAGLEV Platform for Positioning in Arbitrary Orientations,” in *Proc. of the IEEE/ASME International Conference on Advanced Intelligent Mechatronics (AIM)*, Jul. 2020, pp. 1935–1942, DOI: [10.1109/AIM43001.2020.9158898](https://doi.org/10.1109/AIM43001.2020.9158898).
- [45] K. S. Chen, D. L. Trumper, and S. T. Smith, “Design and Control for an Electromagnetically Driven  $X-Y-\theta$  Stage,” *Precision Engineering*, vol. 26, no. 4, pp. 355–369, Oct. 2002, DOI: [10.1016/S0141-6359\(02\)00147-2](https://doi.org/10.1016/S0141-6359(02)00147-2).
- [46] W.-j. Kim and D. L. Trumper, “High-Precision Magnetic Levitation Stage for Photolithography,” *Precision Engineering*, vol. 22, no. 2, pp. 66–77, Apr. 1998, DOI: [10.1016/S0141-6359\(98\)00009-9](https://doi.org/10.1016/S0141-6359(98)00009-9).
- [47] C. Schaeffel, M. Katzschmann, H.-U. Mohr, R. Gloess, C. Rudolf, C. Mock, and C. Walenda, “6D Planar Magnetic Levitation System - PIMag 6D,” *Mechanical Engineering Journal*, vol. 3, no. 1 (15-00111), pp. 1–7, 2016, DOI: [10.1299/mej.15-00111](https://doi.org/10.1299/mej.15-00111).
- [48] P. Berkelman and N. Ohashi, “Analysis and Testing of a Four Coil Magnetic Levitation Configuration,” in *Proc. of the 48th Annual Conference of the IEEE Industrial Electronics Society (IECON)*, Oct. 2022, pp. 1–5, DOI: [10.1109/IECON49645.2022.9968373](https://doi.org/10.1109/IECON49645.2022.9968373).
- [49] H. Song, W. Lin, M. Zhou, G. Liu, H. Pan, and M. Tong, “Robust  $\mathcal{H}_\infty$  Control for Disturbance Rejection in a Magnetic Levitation Device,” in *Proc. of the IEEE 28th International Symposium on Industrial Electronics (ISIE)*, Jun. 2019, pp. 2170–2174, DOI: [10.1109/ISIE.2019.8781533](https://doi.org/10.1109/ISIE.2019.8781533).
- [50] C. P. Britcher and M. Ghofrani, “A Magnetic Suspension System with a Large Angular Range,” *Review of Scientific Instruments*, vol. 64, no. 7, pp. 1910–1917, Jul. 1993, DOI: [10.1063/1.1143976](https://doi.org/10.1063/1.1143976).
- [51] P. Chong, C. Commandeur, H. Davis, and L. Whitehead, “Large-Gap Magnetic Positioning System having Advantageous Configuration,” in *Proc. of the International Symposium on Magnetic Suspension Technology, Part 2*, 1992, pp. 941–953.

- [52] H. Okuizumi, H. Sawada, H. Nagaike, Y. Konishi, and S. Obayashi, "Introduction of 1-m MSBS in Tohoku University, New Device for Aerodynamics Measurements of the Sports Equipment," in *Proc. of the 12th Conference of the International Sports Engineering Association*, vol. 2, no. 6 (273), 2018, pp. 1–7, DOI: [10.3390/proceedings2060273](https://doi.org/10.3390/proceedings2060273).
- [53] C. Inomata, M. Kuwata, S. Yokota, Y. Abe, H. Sawada, S. Obayashi, K. Asai, and T. Nonomura, "Model Position Sensing Method for Low Fineness Ratio Models in a Magnetic Suspension and Balance System," *Review of Scientific Instruments*, vol. 94, no. 2 (025102), pp. 1–13, Feb. 2023, DOI: [10.1063/5.0113806](https://doi.org/10.1063/5.0113806).
- [54] G. Pujol-Vázquez, A. N. Vargas, S. Mobayen, and L. Acho, "Semi-Active Magnetic Levitation System for Education," *Applied Sciences*, vol. 11, no. 12 (5330), pp. 1–14, 2021, DOI: [10.3390/app1125330](https://doi.org/10.3390/app1125330).
- [55] C. M. M. van Lierop, J. W. Jansen, A. A. H. Damen, E. A. Lomonova, P. P. J. van den Bosch, and A. J. A. Vandenput, "Model-Based Commutation of a Long-Stroke Magnetically Levitated Linear Actuator," *IEEE Transactions on Industry Applications*, vol. 45, no. 6, pp. 1982–1990, Nov. 2009, DOI: [10.1109/TIA.2009.2031783](https://doi.org/10.1109/TIA.2009.2031783).
- [56] P. Berkelman and M. Dzadovsky, "Magnetic Levitation over Large Translation and Rotation Ranges in All Directions," *IEEE/ASME Transactions on Mechatronics*, vol. 18, no. 1, pp. 44–52, Feb. 2013, DOI: [10.1109/TMECH.2011.2161614](https://doi.org/10.1109/TMECH.2011.2161614).
- [57] K. Kitagaki, T. Ogasawara, and T. Suehiro, "Methods to Detect Contact State by Force Sensing in an Edge Mating Task," in *Proc. of the IEEE International Conference on Robotics and Automation*, vol. 2, May 1993, pp. 701–706, DOI: [10.1109/ROBOT.1993.291877](https://doi.org/10.1109/ROBOT.1993.291877).
- [58] H. Handa, T. Nozaki, and T. Murakami, "Identification of Contact Position and Force Estimation on Manipulator Using Force Sensor Implemented on Base Frame," *IEEJ Journal of Industry Applications*, vol. 10, no. 3, pp. 324–330, 2021, DOI: [10.1541/ieejjia.20004772](https://doi.org/10.1541/ieejjia.20004772).
- [59] B. Komati, C. Clévy, and P. Lutz, "High Bandwidth Microgripper with Integrated Force Sensors and Position Estimation for the Grasp of Multistiffness Microcomponents," *IEEE/ASME Transactions on Mechatronics*, vol. 21, no. 4, pp. 2039–2049, Aug. 2016, DOI: [10.1109/TMECH.2016.2546688](https://doi.org/10.1109/TMECH.2016.2546688).

- [60] K. Nam, S. Oh, H. Fujimoto, and Y. Hori, “Estimation of Sideslip and Roll Angles of Electric Vehicles Using Lateral Tire Force Sensors Through RLS and Kalman Filter Approaches,” *IEEE Transactions on Industrial Electronics*, vol. 60, no. 3, pp. 988–1000, Mar. 2013, DOI: [10.1109/TIE.2012.2188874](https://doi.org/10.1109/TIE.2012.2188874).
- [61] A. Kanj, R. P. Thanalakshme, C. Li, J. Kulikowski, G. Bahl, and S. Tawfick, “Design, Dynamics, and Dissipation of a Torsional-Magnetic Spring Mechanism,” *Mechanical Systems and Signal Processing*, vol. 179, no. 109307, pp. 1–16, Nov. 2022, DOI: [10.1016/j.ymsp.2022.109307](https://doi.org/10.1016/j.ymsp.2022.109307).
- [62] X. Xiao, “Dynamic Tensile Testing of Plastic Materials,” *Polymer Testing*, vol. 27, no. 2, pp. 164–178, Apr. 2008, DOI: [10.1016/j.polymertesting.2007.09.010](https://doi.org/10.1016/j.polymertesting.2007.09.010).
- [63] X. Yang, L. G. Hector, and J. Wang, “A Combined Theoretical/Experimental Approach for Reducing Ringing Artifacts in Low Dynamic Testing with Servo-Hydraulic Load Frames,” *Experimental Mechanics*, vol. 54, no. 5, pp. 775–789, Jun. 2014, DOI: [10.1007/s11340-014-9850-x](https://doi.org/10.1007/s11340-014-9850-x).
- [64] Y. Xia, J. Zhu, K. Wang, and Q. Zhou, “Design and Verification of a Strain Gauge Based Load Sensor for Medium-Speed Dynamic Tests with a Hydraulic Test Machine,” *International Journal of Impact Engineering*, vol. 88, pp. 139–152, Feb. 2016, DOI: [10.1016/j.ijimpeng.2015.10.004](https://doi.org/10.1016/j.ijimpeng.2015.10.004).
- [65] R. Allemang and P. Avitabile, *Handbook of Experimental Structural Dynamics*. Springer Nature, Jun. 2022, DOI: [10.1007/978-1-4939-6503-8](https://doi.org/10.1007/978-1-4939-6503-8).
- [66] Analog Devices, “Low Power, 18 MHz Variable Gain Amplifier,” AD8338 Datasheet, Apr. 2022. [Online]. Available: <https://www.analog.com/en/products/ad8338.html>
- [67] Baumer, “Distance Sensors,” OM70-P0140.HH0130.VI Datasheet, Apr. 2021. [Online]. Available: <https://www.baumer.com/ch/en/product-overview/distance-measurement/laser-distance-sensors/high-performance/high-measuring-accuracy/om70-p0140-hh0130-vi/p/36863>
- [68] D. J. Ewins, “Mode of Vibration,” in *Encyclopedia of Vibration*, S. Braun, Ed. Oxford: Elsevier, 2001, pp. 838–844, DOI: [10.1006/rwvb.2001.0062](https://doi.org/10.1006/rwvb.2001.0062).
- [69] C. K. Chui and G. Chen, *Kalman Filtering*, 5th ed. Cham: Springer International Publishing, 2017, DOI: [10.1007/978-3-319-47612-4](https://doi.org/10.1007/978-3-319-47612-4).

## Bibliography

---

- [70] B. D. O. Anderson and J. B. Moore, *Optimal Control: Linear Quadratic Methods*, ser. Prentice-Hall Information and System Sciences Series. Englewood Cliffs, N.J.: Prentice-Hall International, 1989.
- [71] T. Abut, "Optimal LQR Controller Methods for Double Inverted Pendulum System on a Cart," *Dicle University Journal of Engineering*, vol. 14, no. 2, pp. 247–255, Jun. 2023, DOI: [10.24012/dumf.1253331](https://doi.org/10.24012/dumf.1253331).
- [72] T. Abut and E. Salkim, "Control of Quarter-Car Active Suspension System Based on Optimized Fuzzy Linear Quadratic Regulator Control Method," *Applied Sciences*, vol. 13, no. 15 (8802), pp. 1–21, Jul. 2023, DOI: [10.3390/app13158802](https://doi.org/10.3390/app13158802).
- [73] T. Zhao and W. Li, "LQR-Based Attitude Controllers Design for a 3-DOF Helicopter System with Comparative Experimental Tests," *International Journal of Dynamics and Control*, Jul. 2023, DOI: [10.1007/s40435-023-01242-1](https://doi.org/10.1007/s40435-023-01242-1).
- [74] G. F. Franklin, J. D. Powell, and A. Emami-Naeini, *Feedback Control of Dynamic Systems*, 8th ed. London: Pearson Education, May 2019, vol. 33.
- [75] R. W. Erickson and D. Maksimovic, *Fundamentals of Power Electronics*, 3rd ed. Cham: Springer Science & Business Media, May 2007, DOI: [10.1007/978-3-030-43881-4](https://doi.org/10.1007/978-3-030-43881-4).
- [76] L. Xing, F. Feng, and J. Sun, "Optimal Damping of EMI Filter Input Impedance," *IEEE Transactions on Industry Applications*, vol. 47, no. 3, pp. 1432–1440, May 2011, DOI: [10.1109/TIA.2011.2127434](https://doi.org/10.1109/TIA.2011.2127434).
- [77] Forsentek, "3 Axis Load Cell 0-100 N Multi-Axis Force Sensor," FNZ Datasheet. [Online]. Available: [http://www.forsentek.com/prodetail\\_279.html](http://www.forsentek.com/prodetail_279.html)
- [78] Analog Devices, "0.25 ppm Noise, Low Drift Precision References," LTC6655/LTC6655LN Datasheet, Apr. 2021. [Online]. Available: <https://www.analog.com/en/products/ltc6655.html>
- [79] Texas Instruments, "ADSxxx3 Dual, 1-MSPS, 16-, 14-, and 12-Bit, 4×2 or 2×2 Channel, Simultaneous Sampling Analog-to-Digital Converter," ADS8363 Datasheet, Sep. 2017. [Online]. Available: <https://www.ti.com/product/ADS8363>

- [80] H. Yaghoubi, “The Most Important MAGLEV Applications,” *Journal of Engineering*, vol. 2013, pp. 1–19, Mar. 2013, DOI: [10.1155/2013/537986](https://doi.org/10.1155/2013/537986).
- [81] E. Csencsics, M. Thier, R. Hainisch, and G. Schitter, “System and Control Design of a Voice Coil Actuated Mechanically Decoupling Two-Body Vibration Isolation System,” *IEEE/ASME Transactions on Mechatronics*, vol. 23, no. 1, pp. 321–330, Feb. 2017, DOI: [10.1109/TMECH.2017.2771440](https://doi.org/10.1109/TMECH.2017.2771440).
- [82] C. Trakarnchaiyo and M. B. Khamesee, “A Novel Wrench-Current Decoupling Strategy to Extend the Use of Small Lookup Data for a Long-Range MAGLEV Planar Motor,” *Actuators*, vol. 12, no. 9 (358), pp. 1–20, Sep. 2023, DOI: [10.3390/act12090358](https://doi.org/10.3390/act12090358).
- [83] E. Csencsics, G. Doblinger, and G. Schitter, “A Novel Magnetically Levitated Tip/Tilt Motion Platform,” *IFAC-PapersOnLine*, vol. 56, no. 2, pp. 3379–3385, Jul. 2023, DOI: [10.1016/j.ifacol.2023.10.1485](https://doi.org/10.1016/j.ifacol.2023.10.1485).
- [84] A. Pechhacker, D. Wertjanz, E. Csencsics, and G. Schitter, “Integrated Electromagnetic Actuator with Adaptable Zero Power Gravity Compensation,” *IEEE Transactions on Industrial Electronics*, vol. 71, no. 5, pp. 5055–5062, May 2024, DOI: [10.1109/TIE.2023.3288176](https://doi.org/10.1109/TIE.2023.3288176).
- [85] M. Takahashi, H. Ogawa, and T. Kato, “Compact MAGLEV Stage System for Nanometer-Scale Positioning,” *Precision Engineering*, vol. 66, pp. 519–530, Nov. 2020, DOI: [10.1016/j.precisioneng.2020.08.016](https://doi.org/10.1016/j.precisioneng.2020.08.016).
- [86] H. Zhang, Y. Lou, L. Zhou, Z. Kou, and J. Mu, “Modeling and Optimization of a Large-Load Magnetic Levitation Gravity Compensator,” *IEEE Transactions on Industrial Electronics*, vol. 70, no. 5, pp. 5055–5064, May 2023, DOI: [10.1109/TIE.2022.3183365](https://doi.org/10.1109/TIE.2022.3183365).
- [87] F. Sun, W. Pei, C. Zhao, J. Jin, F. Xu, and X. Zhang, “Permanent MAGLEV Platform Using a Variable Flux Path Mechanism: Stable Levitation and Motion Control,” *IEEE Transactions on Magnetics*, vol. 58, no. 7, pp. 1–10, Jul. 2022, DOI: [10.1109/TMAG.2022.3174452](https://doi.org/10.1109/TMAG.2022.3174452).
- [88] P. Berkelman and S. Kang, “Optimization of the Four Coil Configuration for Single Magnet Levitation from Below,” in *Proc. of the IUTAM Symposium on Optimal Guidance and Control for Autonomous Systems*, vol. 40, Jan. 2024, pp. 103–115, DOI: [10.1007/978-3-031-39303-7\\_7](https://doi.org/10.1007/978-3-031-39303-7_7).
- [89] H. A. Engmark and K. T. Hoang, “Modeling and Control of a Magnetic Levitation Platform,” *IFAC-PapersOnLine*, vol. 56, no. 2, pp. 7276–7281, Jul. 2023, DOI: [10.1016/j.ifacol.2023.10.338](https://doi.org/10.1016/j.ifacol.2023.10.338).



- [90] K. B. Kim, S. H. Im, D. Y. Um, and G. S. Park, “Comparison of Magnetic Levitation Systems Using Ring-Shaped Permanent Magnets,” *IEEE Transactions on Magnetics*, vol. 55, no. 7, pp. 1–4, Jul. 2019, DOI: [10.1109/TMAG.2019.2895063](https://doi.org/10.1109/TMAG.2019.2895063).
- [91] C. Li and L. Li, “The Stable Magnetic Levitation of a Cylindrical Ferromagnetic Object,” *Journal of Superconductivity and Novel Magnetism*, vol. 27, pp. 2773–2778, Jul. 2014, DOI: [10.1007/s10948-014-2678-x](https://doi.org/10.1007/s10948-014-2678-x).
- [92] N. Bowler, *Eddy-Current Nondestructive Evaluation*, ser. Springer Series in Measurement Science and Technology. Springer, 2019, DOI: [10.1007/978-1-4939-9629-2](https://doi.org/10.1007/978-1-4939-9629-2).
- [93] Renesas, “Inductive Position Sensor IC,” IPS2550 Datasheet, Jun. 2022. [Online]. Available: <https://www.renesas.com/us/en/products/automotive-products/automotive-sensors/automotive-position-sensors/ips2550-inductive-position-sensor-high-speed-motor-commutation-automotive>
- [94] V. Hanta and A. Procházka, “Rational Approximation of Time Delay,” *Institute of Chemical Technology in Prague. Department of Computing and Control Engineering. Technická*, vol. 5, no. 166, pp. 28–34, 2009.
- [95] P. Roriz, L. Carvalho, O. Frazão, J. L. Santos, and J. A. Simões, “From Conventional Sensors to Fibre Optic Sensors for Strain and Force Measurements in Biomechanics Applications: A Review,” *Journal of Biomechanics*, vol. 47, no. 6, pp. 1251–1261, Apr. 2014, DOI: [10.1016/j.jbiomech.2014.01.054](https://doi.org/10.1016/j.jbiomech.2014.01.054).
- [96] J. Jiang, W. Chen, J. Liu, W. Chen, and J. Zhang, “Optimum Design of a Dual-Range Force Sensor for Achieving High Sensitivity, Broad Bandwidth, and Large Measurement Range,” *IEEE Sensors Journal*, vol. 15, no. 2, pp. 1114–1123, Feb. 2015, DOI: [10.1109/JSEN.2014.2360885](https://doi.org/10.1109/JSEN.2014.2360885).
- [97] A. J. Petruska and B. J. Nelson, “Minimum Bounds on the Number of Electromagnets Required for Remote Magnetic Manipulation,” *IEEE Transactions on Robotics*, vol. 31, no. 3, pp. 714–722, Jun. 2015, DOI: [10.1109/TRO.2015.2424051](https://doi.org/10.1109/TRO.2015.2424051).
- [98] J. Hagedorn, F. S. L. Blanc, and J. Fleischer, *Handbook of Coil Winding*. Berlin: Springer-Verlag, 2018, DOI: [10.1007/978-3-662-54402-0](https://doi.org/10.1007/978-3-662-54402-0).

- [99] S. M. Mirić, R. V. Giuffrida, D. Bortis, and J. W. Kolar, “Enhanced Complex Space Vector Modeling and Control System Design of Multiphase Magnetically Levitated Rotary–Linear Machines,” *IEEE Journal of Emerging and Selected Topics in Power Electronics*, vol. 8, no. 2, pp. 1833–1849, Jun. 2020, DOI: [10.1109/JESTPE.2019.2945625](https://doi.org/10.1109/JESTPE.2019.2945625).

# Curriculum Vitae

## Personal Information

Name	Reto Bonetti
Date of birth	March 2, 1995
Nationality	Swiss
Citizen of	Gordola, Switzerland
Contact	reto.bonetti@gmail.com

## Education

2020 – 2023	Doctorate, ETH Zurich Power Electronic Systems Laboratory (PES)
2018 – 2020	MSc ETH, ETH Zurich Information Technology and Electrical Engineering
2014 – 2018	BSc ETH, ETH Zurich Information Technology and Electrical Engineering
2010 – 2014	High School, Locarno Physics and Applied Mathematics

## Work Experience

2020 – 2023	Research Assistant, ETH Zurich Power Electronic Systems Laboratory (PES)
2019 – 2019	Research Assistant, ETH Zurich Laboratory for High Power Electronic Systems (HPE)